Anisotropic colloidal assembly: kinetics, shape complementarity, and field-mediated propulsion

by

Laura D Colón-Meléndez

A dissertation submitted in partial fulfillment
of the requirements for the degree of
Doctor of Philosophy
(Physics)
in the University of Michigan
2016

Doctoral Committee:

Professor Michael J. Solomon, Chair
Professor Sharon C. Glotzer, Co-Chair
Professor Cagliyan Kurdak
Professor Ronald G. Larson
Professor Xiaoming Mao

Dedication

Para mi Mamá, mi sobrino, y mis abuelos, y para todos aquellos que luchan para hacer de Puerto Rico un país libre y soberano.

For my Mom, my nephew, and my grandparents, and for all people who fight to make Puerto Rico a free and sovereign country.

Acknowledgments

As I finish this long journey, there are many people who I feel I need to thank. Without their care and support, I would not have been able to complete my doctorate.

I am so grateful to have had an advisor as understanding, supportive, and compassionate as Mike Solomon. Mike: Science goes on because of the effort, caring and support of investigators and educators as you. I would also like to thank the rest of my committee members: Ron, it has been a pleasure to work with someone as insightful and brilliant as you. Sharon, I take huge inspiration in your masterful talks and the beautiful manuscripts you have created with your students. I think we both love the beauty of physics very much. Cagliyan, thank you for mentoring me and guiding me through troubled times. Xiaoming, although we did not work a lot together, I find your work truly fascinating. To all the members of my committee, it has been an honor to work with you.

I would not have finished this without my mother's unwavering love and support. Mami, thank you for everything. Thank you for loving me unconditionally, for visiting me, for tolerating my bad moods, for driving me to voice lessons and music classes at the Conservatorio as a child, for teaching me math and logic concepts when I was a kid, and for calling me every morning these last few weeks to

encourage me to start the day early. Your perseverance and discipline are incredible examples to follow. I have missed you a lot during my time here. I love that we are such great friends. Papi, I want to take my kids to classical music concerts on Sunday mornings too. Thank you for teaching me to love music. I think we understand each other a lot, since we are both very sensitive people who feel their emotions deeply. ¡Vayamos al Perito Moreno! ¡Qué bonita suena la palabra Ushuaia! Moncho, thank you for making me laugh and for asking me when I'm going to be done. Lissy, gracias por todo el cariño. To my nephew Noel Alejandro, this thesis is for you. You are my sun, and I adore you. Luna, my dog: you can't read, but everyone should know that having you was the best decision I made for my mental health while in Ann Arbor.

Erman, seni sevyorum! Thank you for your love and support! I cannot wait until we make our dreams together a reality. Let's see what adventures life has in place for us to figure out, survive and enjoy together. I love you. I love us. I will learn Turkish. Take me to Pamukkale during a season when the place looks white and blue. I can't wait to see Cappadocia from the sky with you! Also, we seriously need to go to Culebra. Te amo.

Abuelo Noel y Abuela Annie: Thank you for reminding me where I am from and what I stand for. Thank you for those long afternoon conversations. I have missed you dearly.

To the rest of my family: What can I say? You have been instrumental in my development as a human being. Eva: I am so happy that over the last few years we've gotten to share time together here in the states. I thank you for cheering me up when I most need it! I love you! Tití Milly, thank you for all the love and all the

photos. Tío Celes, I will always remember the conversation we had in the NYC subway when you told me that studying science was a good choice, because the world needs more humanists to be scientists, and more scientists to be humanists. Tití Eda, I am looking forward to coffee and more days spent in Old San Juan. To my godfather Javier, thank you for the moral support. To Tití Ana, thank you for that copy of "The Places You'll Go" by Dr. Seuss. It's one of my favorite books. To all my cousins: I have missed our family get-togethers!

Renée, thank you for your support and your unwavering friendship. We finished! We have grit, we have passion, and we persevere. Myriam, I've missed you so much, and I love that every time I go back home, we get to spend time together and chat about life like in old times. Shefali, I am so grateful to you for your friendship and gigantic kindness. I will visit you in Boston! Lorena, Marco, Luis, Zorimar, Mara, Sarah – thank you for your friendship. Fernando and Margarita – thank you for mentoring me thru all these years.

During my stay in Prof. Solomon's group, I had exceptional colleagues who I am happy to also call my friends: Lilian, Youngri, Liz, Leo, Aayush, Mahesh, Nina, Sepideh, Ona, Carlos, Megan, Joe, Maria – thank you for the good times. You are all amazingly smart people, and it has been a great experience to be in Mike's group with you. I would also like to thank Julie, Michelle, and Li for their friendship.

I want to thank Christina Zigulis and Susan Hamlin for treating me with such care and competence. Julie Gales, thank you. Karen Coulter, thank you. William and Gladys, I am thankful for our conversations and hugs! I am certain I am forgetting to thank a lot of people. Please accept my apologies, but know that I am deeply grateful

for your help and your care. Being nice to people matters! I'm going to pay it forward.

Table of Contents

List of Figures

Abstract

In the first part of this dissertation, we study the binding kinetics and equilibrium thermodynamics of suspensions of lock and key anisotropic colloidal particles that self-assemble in the presence of polyethylene oxide polymeric depletant. Using confocal laser scanning microscopy and particle tracking methods, we measure the kinetic pathways of interaction of lock and key particles. We find that specific lock-key bonds can be formed by the diffusion of a key into the lock dimple from bulk or by the surface diffusion of a key particle that binds to the spherical surface of the lock and diffuses on its surface until finding and binding to the lock dimple. We compare experimental results to a Smoluchowski diffusion-migration model and find quantitative agreement between both.

We then investigate the equilibrium thermodynamic behavior of lock and key colloids by varying the degree of shape complementarity between the lock dimple and the key particles. We perform binding experiments with five different key particles whose sizes are smaller or larger than the dimple cavity size, and find lower free energies of formation for key particles that are smaller than the dimple radius of curvature. Moreover, we find that binding affinity is asymmetric about this optimum: smaller keys have better overall binding affinity to the lock dimple than keys larger than the lock dimple. Our results are in agreement with previous

modeling and simulation work that predicts optimized binding and formation of specific lock-key bonds for spherical key particles smaller than the lock cavity radius.

In the second part of this dissertation, we investigate emerging propulsion of transient associations of colloidal spheres in binary suspensions subject to a low frequency oscillatory electric field that acts perpendicular to the plane of motion of the particles. Particle propulsion under perpendicular oscillatory electric fields has been observed before for rigid colloidal dimers and asymmetric dumbbells. We observe propulsion arise in a binary suspension of unequally sized unbound particles that revert back to normal diffusion upon turning off the electric field. We attribute the active motion of particles to unbalanced electrohydrodynamic flow. We characterize large particle motion using confocal microscopy and particle tracking algorithms, and find that the mean-squared displacement of the particles is well fit by single-particle active motion models of mean-squared displacement. We observe that the propulsion speed of large particles increases with increasing applied voltage and decreases with increasing frequency of oscillation. Moreover, we characterize the short-time ballistic motion of the particles and find it to depend on the number of small particle neighbors surrounding the large particle, where particles with 2 and 3 small neighbors move fastest.

Chapter 1
Introduction

The study of colloidal particles and suspensions is part of the study of soft condensed matter: matter that is easily deformed by external forces or thermal fluctuations. Colloidal particles are mesoscopic building blocks that can be used, by tuning their interactions, to produce artificial soft matter via self-assembly in equilibrium and out-of-equilibrium systems. In this dissertation we investigate the equilibrium self-assembly kinetics and thermodynamics of anisotropic colloidal particles interacting via polymer-mediated depletion. We also investigate out-of-equilibrium, emerging active motion in a suspension of binary isotropic colloids driven by an electric field.

Colloidal particles

Colloidal suspensions are made of particles suspended in a fluid, where the particles are a few nanometers to a few microns in size, and the fluid can be treated as a continuum medium.[1] When in suspension, colloidal particles diffuse by Brownian motion owing to thermal forces imparted to them by the surrounding medium. Due to their size, colloidal particles can be studied with diverse microscopy methods, from scanning and transmission electron microscopy to brightfield and confocal laser scanning microscopy[2]. Model spherical colloids have been used to

understand the liquid state[3,4], the phase behavior of hard spheres[5-7], and glassy dynamics[8]. Although much has been learned from colloidal spheres, their isotropic interactions result in the formation of structures with relatively simple symmetry and high coordination number. Nature, on the other hand, uses anisotropic interactions, that is, directed and selective interactions between atoms and molecules to form materials as complex as the double helix of DNA or protein crystals on the surface of bacteria[9]. Introducing anisotropic interactions to colloidal particles can lead to the fabrication of materials with similar complexity.

In recent years, different synthetic routes to make anisotropic colloidal particles have been developed, spurred by the abundance of different colloidal synthesis methods. Chemically patchy particles as well as shape anisotropic particles have been synthesized in the lab, enabling scientists to study the effect of anisotropy on particle self-assembly[10] and to predict what particle shapes and interactions would lead to the efficient assemblies of a given target structure[11]. Examples of patchy particles include tri-block metallodielectric Janus particles[12], particles with DNA patches on its surface[13], and ellipsoids with chemically patchy surfaces[14]. Patchy particles may also be created using methods like electrohydrodynamic co-jetting[15], placing different types of materials into a single particle, which can be very useful for applications like drug delivery and drug therapy[10]. Shape anisotropic (anisometric) particles include rough spheres[11], ellipsoidal particles[16], discoids[17], branched nanoparticles[18], colloidal molecules with controlled bond angles[19], and dimpled particles[20-22], among many others.

Lock colloids

Recently, dimpled colloids made of 3-trimethoxysilylpropyl methacrylate (TPM) have been synthesized in high yield via a two-step polymerization reaction.[23] A polycondensation step leads to the formation of TPM droplets, and a subsequent free radical polymerization step leads to the formation of a thin elastic shell on the surface of the droplets that eventually buckles to form a dimple on the particle. The dimple on the surface of these lock colloidal particles is a region of concave curvature on the surface of the otherwise spherical (convex) particle surface. The dimple radius of curvature is different than the lock particle radius. Lock and key colloids are a coarse model of Fischer's lock-and-key model for receptor-ligand binding.[20] There are other synthetic routes that can be used to make dimpled particles: seeds or templates can be used to make lock particles with perfectly shaped dimples of ellipsoidal, cubic, or spherical shape[24]. Lock particles with multiple cavities have also been experimentally realized.[25]

Interactions between colloidal particles

The properties of colloidal suspensions and the assemblies they form are dependent on the interactions between the particles. Colloidal particles suspended in a fluid interact with each other via electrostatic and van der Waals forces, as well as hard-core excluded volume repulsion, among other interactions.[26] Hard-core repulsion arises because particles occupy a finite, impenetrable volume. The screened electrostatic interaction arises due to Coulombic interaction of the

particles' diffuse double layers, which surround charged particles in suspension. It is a repulsive interaction for equally charged particles and attractive for oppositely charged ones. The electrostatic interaction potential can be tuned by tuning the electrolyte concentration of the suspension. Dispersion or van der Waals interactions between particles occur due to quantum mechanical effects regarding time-correlations in the fluctuation of particle polarizability, and can be tuned, for example, by changing the type of solvent the particles are dispersed in. The Derjaguin-Landau-Verwey-Overbeek (DLVO) theory of colloidal interactions includes the effect of electrostatic and van der Waals forces, and adequately describes the interaction of colloidal particles in suspension in electrolyte solutions[1]. In systems where DLVO forces cause aggregation of particles, suspensions can be stabilized by the use of steric agents, which preferentially deposit themselves on or are grafted onto the surface of particles creating a steric energy barrier that prevents particle aggregation. Chemical patchiness and shape anisotropy introduce orientational effects to the above mentioned pair interactions. For example, metallodielectric Janus particles have stronger van der Waals interactions when the metallic hemispheres of the particles come together than when their dielectric hemispheres are in contact.[27]

Depletion interaction

Colloidal particles may also interact with each other through the depletion interaction. The depletion interaction between particles arises whenever large

particles are in the presence of smaller particles or cosolutes. It is entropic in origin, since it results from excluded volume interactions, namely the exclusion of smaller particles from the gaps between larger particle surfaces.[28] Large particles in the presence of small depletants have a depletant exclusion zone around their surface, the thickness of which is given by the radius of the small depletants, since the centers of the depletant particles cannot get any closer to the surface of the large particles than this distance. When the surfaces of large particles are within a distance less than the size of the depleting particles, an osmotic pressure difference pushes the large particles together. This osmotic pressure difference arises due to the different concentrations of depletant particles in the gap region between the particles and elsewhere. When two large particles come together, a volume equal to the overlap of the particles' depletion zones, ΔV, is made available for the depletant particles to occupy. This increases the entropy of the system, which lowers the free energy of the overall suspension.

The depletion pair interaction potential $\Phi_{\text{depletion}}$ is described by

$$\phi_{depletion} = -\Pi_{depletion}\,\Delta V, \quad (1)$$

where $\Pi_{\text{depletant}}$ is the depletant osmotic pressure. This equation suggests ways of tuning the depletion interaction potential: the depletant's osmotic pressure or the overlap of particle depletion zones can be changed by, for example, use of thermoresponsive depleting polymer particles, such as pNIPAM (poly(N-isopropylacrylamide)), or by engineering particle shapes so as to impart directionality to the depletion interaction. Particles such as lock colloids, described

above, are good candidates to study how the depletion interaction mediates interactions between particles with anisometry.

There have been a few studies that investigate the effect of changing ΔV on the depletion interaction. Notably, Dinsmore et al.[29] studied how surface microstructure leads to the creation of "localized entropic force fields" that effect particle motion near edges when in the presence of depleting particles. Kraft et al.[30] reports that anisotropic particles with regions of differing surface roughness lead to the formation of colloidal micelles in the presence of depletants. Lock and key colloidal self-assembly, which is the focus of the first part of this disseration, has also been studied in the presence of non-adsorbing polymeric depletants.[20] We focus on studying the binding kinetics of lock-key colloids and the effect shape complementarity has on the equilibrium thermodynamic behavior of lock-key colloidal suspensions interacting via the depletion interaction. Shape complementarity between lock and key colloids has a direct effect on the size of the overlap of exclusion zones, ΔV, and therefore on the interaction between lock and key particles.

Colloidal self-assembly

Colloidal self-assembly is a spontaneous, reversible thermodynamic process dictated by the minimization of free energy of the system. In constant volume systems, the total free energy of the system -- the Helmholtz free energy , F-- is due to the internal energy U and the entropy of the system S, and is given by F = U – TS,

where T is the temperature of the system. (In isobaric systems, the Gibbs free energy is minimized.) The types of structures that building blocks can assemble into depend on the types and the strength of interactions existing between particles - the internal energy - and how many microstates the system has access to – its entropy.[A]

Spherical colloidal particles with hard-core repulsion self-assemble into symmetric structures at sufficiently high volume fraction as a consequence of the spherical symmetry of their interactions, whereas spheres with short-ranged attractive interactions may form gels[37]. Spherical particles form close packed assemblies where particles have a coordination number as high as 12. For anisotropic colloidal systems, particle location and orientation can result in the formation of materials with other symmetries[38-40] because of the directional dependence of particle interactions, which may result in the formation of structures with low coordination number.[41] Anisotropic building blocks may prefer to orient themselves in a particular way to, for example, minimize internal energy and, thus, their free energy.

In systems of particles that interact through anisotropic interaction potentials, differing energy scales at different particle relative orientations can lead

[A] Structure formation in isometric and anisometric particle systems can be realized solely by the maximization of entropy. Recent studies of "entropically patchy particles" [31-36] have shown that entropy can order particles that interact through hard-core or excluded volume interactions. Entropic patches in anisometric particles lead to the emergence of directional entropic forces[34]. Maximization of entropy does not always imply the existence of disorder in a system; if there are more ways to organize (order) a collection of particles in a system than to keep the particles in disordered configurations, minimization of free energy dictates that particles will organize.

to the frustration of structure formation due to kinetic trapping of the system as it attempts to minimize its free energy[42]. Particles may remain stuck in metastable configurations[17] and form arrested structures. In order to make ordered materials out of anisotropic colloids, we need to understand how their constituents interact, and how to tune or control anisotropic interactions for assembly purposes. This understanding could lead to the design of anisotropic particles that interact with each other in a rational, prescribed manner[43,44]. A promising way to control the self-assembly of anisotropic particles is by engineering the free energy as well as diffusivity landscapes of interacting particles[45].

Salient examples of anisotropic colloidal assemblies include the formation of an ordered cubic crystalline phase of cubic-shaped colloids interacting via the depletion interaction[38], as well as the formation of an open Kagomé lattice with patchy tri-block metallodielectic Janus particles in electrolyte solution[12]. In the latter, a Kagomé lattice is formed when each metallic patch in a particle is in contact with two other particles' metallic patches. This leads to the formation of an open, flexible lattice with different pore sizes and interesting mechanical behavior.[40,46] Patchy colloids with different types of DNA strands on its surface serve as an additional example of colloids with valence and directional interactions[41] that form colloidal molecules with suitable partners.

Simulation work regarding the self-assembly of lock-and-key colloids has shown sensitive dependence of the resulting structures on the shape of the lock dimple.[47] Other simulation work has shown that lock-key colloidal molecules –

comprised of one central key surrounded by one to four locks -- may form structures with complex symmetries, depending on bond length and relative particle size.[48] In this dissertation, we investigate how readily lock and key colloids associate to form specific lock-and-key bonds, which precludes the formation of lock-key colloidal molecules. Optimizing the assembly of lock-key colloidal molecules lays the foundation for subsequent investigation of structure formation in self-assembled lock-key systems.

Colloidal assembly can also be aided by the use of external fields such as gravitational[49], electromagnetic[50,51], and shear flow fields[52]. Externally applied forces help particles overcome kinetic and energy barriers to assembly, changing the free energy landscape of interaction between building blocks. Changes in temperature can also be strategically used to control the quenching of structures of colloidal particles, specifically those where single-stranded DNA is used to induce particle interactions[53,54], those that use polyethylene oxide as depletant[55], or that use thermoresponsive depletant polymers whose radius of gyration is temperature-dependent (and therefore result in temperature-dependent $\Delta V_{overlap}$), like pNIPAM.[56]

Application of external fields may also lead to the actuation of reversible colloidal structures, which enable switching from one configuration of particles to another. Recently, alternating current (AC) electric fields applied perpendicular to the plane of particle motion were observed to induce anisotropic interactions between spherical particles, resulting in the reversible formation of colloidal

molecules and open structures of spherical particles.[57] Recently, metallodielectric Janus ellipsoids were observed to self-assemble into chains and bundles that respond to the application of a co-planar AC electric field by stretching, increasing their length by ~36%.[58] Recently, parallel AC electric fields were also found to induce lock-key binding in the absence of depleting polymer.[59] Magnetic fields have also been used to aid particle self-assembly: magnetic fields were found to synchronize the self-assembly of metallodielectric Janus spheres into microtubes or small clusters[60], and hematite cubes embedded in a TPM polymer matrix have been used as magnetic patches that "click" together to form colloidal molecules and higher order structures in the presence of magnetic fields.[61]

Colloidal active motion and active matter

Colloidal suspensions have also been used to study active matter. Active matter is made of particles that consume energy from their environment and transform this energy into kinetic energy by undergoing directed motion. Active matter has the ability to self-organize into transient, dynamic structures. Examples of active matter include run-and-tumble bacteria like E. coli[62,63], living cells, flocks of birds, and schools of fish[64].

A few artificial colloidal active particle systems have been experimentally realized and studied. Metallodielectric platinum/polystyrene Janus particles propel due to self-diffusiophoresis when immersed in hydrogen peroxide (H_2O_2) solutions [65]. The asymmetric distribution of catalyst on the surface of the Janus particle sets a

concentration gradient of hydrogen peroxide, which drives particle propulsion in these systems. Carbon/silica Janus particles in critical water-2,6-lutidine mixtures propel upon heating by a green light laser.[66] TPM spheres with a hematite patch on their surface have also been observed to propel in H_2O_2 solutions upon illumination with ultraviolet light.[67,68]

Anisotropic dumbbell particles have been observed to individually propel and form propelling chiral clusters due to the action of low-frequency AC electric fields applied perpendicular to the particles' plane of motion.[69] Here, particle propulsion occurs due to unbalanced electrohydrodynamic (EHD) flow acting on the particle. The EHD flow acting on the particles is due to the particle's induced dipole electric field perturbing the concentration polarization layer that is set up on top of a conducting electrode upon application of an electric field.[70,71] Symmetric particles do not propel under the same conditions, but form colloidal crystalline clusters.[72] Further experimental verification of the origin of this new propulsion mechanism was obtained by performing experiments with irreversibly bound colloidal dimers with asymmetric properties.[73] Tuning the propulsion speed of these dimers is possible by choosing particles with differing size, composition, and zeta potential to form the colloidal dimers. In the second part of this thesis, we investigate emergent propulsion of particles in binary colloidal suspensions of unequally sized colloidal spheres driven by an alternating current electric field that acts perpendicular to the plane of particle motion. We observe active motion of unbound particles that couple due to the action of a low-frequency AC electric field. To the best of our knowledge,

this is the first time propulsion has been observed in a system of isotropic, unmodified colloidal particles.

The dynamic behavior of active colloidal particles is different than that of Brownian colloidal particles. Passive Brownian particles undergo translational as well as rotational diffusion[1]. The direction of motion of a passive Brownian particle is random, given the stochastic nature of the Brownian force. In N dimensions, the mean-squared displacement of a particle with translational diffusion coefficient D at lag time t is given by:

$$\langle \Delta r^2(t) \rangle = 2\, N\, D\, t\,. \qquad (2)$$

In the case of active colloidal particles propelling with velocity **v**, particle motion is due to an internal self-propelling force as well as random diffusion[74]. The mean-squared displacement of an active colloidal particle exhibits ballistic behavior at short times relative to the time it takes the particle to change its orientation; at lag times longer than this characteristic reorientation time, the mean-squared displacement of active particles is linear in time, with an enhanced effective diffusion coefficient[65,67]. The two-dimensional mean-squared displacement of an active colloidal particle with passive translational diffusion coefficient D, propulsion speed v, and reorientation time τ at lag time t is given by[75]

$$\langle \Delta r^2(t) \rangle = 4\, D\, t + {}^1\!/_2\, v^2 \tau^2 \left(\frac{2t}{\tau} + \exp\left(-\frac{2t}{\tau} \right) - 1 \right). \qquad (3)$$

Active colloidal particle suspensions have also been used to study dynamic clustering, phase separation[76] and giant number fluctuations[67,77]. Dynamic

clustering in active particle suspensions is caused by self-trapping of the self-propelled particles.[67,76] At higher particle densities, active colloidal suspensions are observed to phase separate into a dilute gas phase and a dense large clusters phase.[76] Giant number fluctuations, which are characteristic of out-of-equilibrium systems, have been observed in colonies of bacteria[78], in actively driven granular rods[79], and, recently, in light-activated active colloidal particles.[67] Systems in thermal equilibrium have number fluctuations with standard deviation ΔN that grows as $\Delta N \sim \sqrt{N}$; the relation is exact for an ideal gas. Ordered states of active, self-propelled particles exhibit giant number fluctuations with standard deviation in particle numbers that grow as $\Delta N \sim N$. The active colloidal particle system we present in this dissertation could be used to study collective active matter phenomena, since particle dynamics can be easily quantified using image processing and particle tracking methods.

Organization the dissertation

This dissertation is divided in two parts. In the first part of the dissertation, we study the binding kinetics and equilibrium thermodynamic behavior of lock-key colloidal suspensions in the presence of polyethylene oxide, a non-ionic, non-adsorbing polymer. In the second part of the dissertation, we investigate emerging particle propulsion in binary colloidal suspensions under the effect of an alternating current electric field applied perpendicular to the plane of particle motion.

In the first part of the dissertation (Chapters 2 and 3) we seek to understand how shape complementarity affects binding kinetics and the equilibrium thermodynamic behavior of lock and key colloids interacting via the depletion interaction. In Chapter 2, we use confocal laser scanning microscopy and particle tracking methods to study how lock-key pairs form specific bonds. We compare experimental measurements of rate constants and free energy to Smoluchowski diffusion-migration modeling of the system. In Chapter 3, using confocal microscopy, we measure fractional occupation and equilibrium free energies of formation of specific lock-key bonds as a function of varying key-to-dimple size ratio to understand the role of shape complementarity for lock-key binding. Understanding how and why lock and key colloids bind to form colloidal molecules will enable future researchers to assemble structures with these novel building blocks.

In Part 2 of the dissertation (Chapter 4), we use confocal laser scanning microscopy and particle tracking algorithms to characterize the dynamics of propelling particles in a binary colloidal suspension of unequally sized latex beads.. We characterize the short-time ballistic motion of large particles as a function of the number of small neighbors surrounding it.

We conclude by summarizing our results and suggesting future work that would complement the research presented in this dissertation.

References

[1] W.B. Russel, D.A. Saville, and W.R. Schowalter, *Colloidal Dispersions* (Cambridge University Press, Cambridge, 2009).

[2] V. Prasad, D. Semwogerere, and E.R. Weeks, Journal of Physics: Condensed Matter **19**, 113102 (2007).

[3] J.G. Kirkwood, The Journal of Chemical Physics **10**, 394 (1942).

[4] J.D. Weeks, The Journal of Chemical Physics **54**, 5237 (1971).

[5] P.N. Pusey and W. van Megen, Nature **320**, 340 (1986).

[6] W. Kegel and van Blaaderen A, Science **287**, 290 (2000).

[7] S. Auer, W.C.K. Poon, and D. Frenkel, Physical Review E **67**, 020401 (2003).

[8] W. van Megen, T.C. Mortensen, S.R. Williams, and J. Müller, Physical Review E **58**, 6073 (1998).

[9] R.P. Fagan and N.F. Fairweather, Nature Reviews Microbiology **12**, 211 (2014).

[10] S.C. Glotzer and M.J. Solomon, Nature Materials **6**, 557 (2007).

[11] E. Jankowski and S.C. Glotzer, Soft Matter **8**, 2852 (2012).

[12] Q. Chen, S.C. Bae, and S. Granick, Nature **469**, 381 (2011).

[13] Y. Wang, Y. Wang, D.R. Breed, V.N. Manoharan, L. Feng, A.D. Hollingsworth, M. Weck, and D.J. Pine, Nature **491**, 51 (2012).

[14] Z. Zhang, P. Pfleiderer, A.B. Schofield, C. Clasen, and J. Vermant, Journal of the American Chemical Society **133**, 392 (2011).

[15] J. Lahann, Small **7**, 1149 (2011).

[16] C.C. Ho, A. Keller, J.A. Odell, and R.H. Ottewill, Colloid & Polymer Science **271**, 469 (1993).

[17] L.C. Hsiao, B.A. Schultz, J. Glaser, M. Engel, M.E. Szakasits, S.C. Glotzer, and M.J. Solomon, Nature Communications **6**, 8507 (2015).

[18] R. He, Y.-C. Wang, X. Wang, Z. Wang, G. Liu, W. Zhou, L. Wen, Q. Li, X. Wang, X. Chen, J. Zeng, and J.G. Hou, Nature Communications **5**, (2014).

[19] D.J. Kraft, J. Groenewold, and W.K. Kegel, Soft Matter **5**, 3823 (2009).

[20] S. Sacanna, W.T.M. Irvine, P.M. Chaikin, and D.J. Pine, Nature **464**, 575 (2010).

[21] S. Sacanna, W.T.M. Irvine, L. Rossi, and D.J. Pine, Soft Matter **7**, 1631 (2011).

[22] J.J. Crassous, A.M. Mihut, L.K. Månsson, and P. Schurtenberger, Nanoscale **7**, 15971 (2015).

[23] S. Sacanna, W.T.M. Irvine, L. Rossi, and D.J. Pine, Soft Matter **7**, 1631 (2011).

[24] S. Sacanna, M. Korpics, K. Rodriguez, L. Colón-Meléndez, S.-H. Kim, D.J. Pine, and G.-R. Yi, Nature Communications **4**, 1688 (2013).

[25] Y. Wang, Y. Wang, X. Zheng, G.-R. Yi, S. Sacanna, D.J. Pine, and M. Weck, Journal of the American Chemical Society **136**, 6866 (2014).

[26] J.N. Israelachvili, *Intermolecular and Surface Forces*, 3rd ed. (Elsevier, 2011).
[27] O. Shemi and M.J. Solomon, Langmuir **30**, 15408 (2014).

[28] H.N.W. Lekkerkerker and R. Tuinier, *Colloids and the Depletion Interaction* (Springer Netherlands, Dordrecht, 2011).

[29] A.D. Dinsmore, A.G. Yodh, and D.J. Pine, Nature **383**, 239 (1996).

[30] D.J. Kraft, R. Ni, F. Smallenburg, M. Hermes, K. Yoon, D.A. Weitz, A. van Blaaderen, J. Groenewold, M. Dijkstra, and W.K. Kegel, Proceedings of the National Academy of Sciences **109**, 10787 (2012).

[31] P.F. Damasceno, M. Engel, and S.C. Glotzer, ACS Nano **6**, 609 (2011).

[32] P.F. Damasceno, M. Engel, and S.C. Glotzer, Science **337**, 453 (2012).

[33] G. van Anders, N.K. Ahmed, R. Smith, M. Engel, and S.C. Glotzer, ACS Nano **8**, 931 (2013).
[34] G. van Anders, D. Klotsa, N.K. Ahmed, M. Engel, and S.C. Glotzer, Proceedings of the National Academy of Sciences **111**, E4812 (2013).

[35] E.S. Harper, R.L. Marson, J.A. Anderson, G. van Anders, and S.C. Glotzer, Soft Matter **11**, 7250 (2015).

[36] N.K. Ahmed, G. van Anders, E.R. Chen, and S.C. Glotzer, arXiv **cond-mat.mtrl-sci**, (2015).

[37] P.J. Lu, E. Zaccarelli, F. Ciulla, A.B. Schofield, F. Sciortino, and D.A. Weitz, Nature **453**, 499 (2008).

[38] L. Rossi, S. Sacanna, W.T.M. Irvine, P.M. Chaikin, D.J. Pine, and A.P. Philipse, Soft Matter **7**, 4139 (2011).

[39] J.D. Forster, J.-G. Park, M. Mittal, H. Noh, C.F. Schreck, C.S. O'Hern, H. Cao, E.M. Furst, and E.R. Dufresne, ACS Nano **5**, 6695 (2011).

[40] D.Z. Rocklin and X. Mao, Soft Matter **10**, 7569 (2014).

[41] Y. Wang, Y. Wang, D.R. Breed, V.N. Manoharan, L. Feng, A.D. Hollingsworth, M. Weck, and D.J. Pine, Nature **491**, 51 (2012).

[42] M.F. Hagan, O.M. Elrad, and R.L. Jack, The Journal of Chemical Physics **135**, 104115 (2011).

[43] S. Sacanna, D.J. Pine, and G.-R. Yi, Soft Matter **9**, 8096 (2013).

[44] J. Zhang, E. Luijten, and S. Granick, Annual Review of Physical Chemistry **66**, 581 (2015).

[45] D.J. Beltran-Villegas and M.A. Bevan, Soft Matter **7**, 3280 (2011).

[46] X. Mao, Q. Chen, and S. Granick, Nature Materials **12**, 217 (2013).

[47] D.J. Ashton, R.L. Jack, and N.B. Wilding, Soft Matter **9**, 9661 (2013).

[48] D. Ortiz, K.L. Kohlstedt, T.D. Nguyen, and S.C. Glotzer, Soft Matter **10**, 3541 (2014).

[49] A. Mohraz and M.J. Solomon, Langmuir **21**, 5298 (2005).

[50] A.A. Shah, H. Kang, K.L. Kohlstedt, K.H. Ahn, S.C. Glotzer, C.W. Monroe, and M.J. Solomon, Small **8**, 1551 (2012).

[51] J.A. Ferrar and M.J. Solomon, Soft Matter **11**, 3599 (2015).

[52] L.T. Shereda, R.G. Larson, and M.J. Solomon, Physical Review Letters **105**, 228302 (2010).

[53] R. Dreyfus, M.E. Leunissen, R. Sha, A. Tkachenko, N.C. Seeman, D.J. Pine, and P.M. Chaikin, Physical Review E **81**, 041404 (2010).

[54] Y. Wang, Y. Wang, X. Zheng, É. Ducrot, J.S. Yodh, M. Weck, and D.J. Pine, Nature Communications **6**, 7253 (2015).

[55] L. Feng, B. Laderman, S. Sacanna, and P. Chaikin, Nature Materials **14**, 61 (2014).

[56] R.H. Pelton and P. Chibante, Colloids and Surfaces **20**, 247 (1986).

[57] F. Ma, D.T. Wu, and N. Wu, Journal of the American Chemical Society **135**, 7839 (2013).

[58] A.A. Shah, B. Schultz, W. Zhang, S.C. Glotzer, and M.J. Solomon, Nature Materials **14**, 117 (2014).

[59] M. Kamp, N.A. Elbers, T. Troppenz, A. Imhof, M. Dijkstra, R. van Roij, and A. van Blaaderen, Chemistry of Materials **28**, 1040 (2016).

[60] J. Yan, M. Bloom, S.C. Bae, E. Luijten, and S. Granick, Nature **491**, 578 (2012).

[61] S. Sacanna, L. Rossi, and D.J. Pine, Journal of the American Chemical Society **134**, 6112 (2012).

[62] H.C. Berg and D.A. Brown, Nature **239**, 500 (1972).

[63] A.E. Patteson, A. Gopinath, M. Goulian, and P.E. Arratia, Scientific Reports **5**, 15761 (2015).

[64] G. Popkin, Nature **529**, 16 (2016).

[65] J.R. Howse, R.A.L. Jones, A.J. Ryan, T. Gough, R. Vafabakhsh, and R. Golestanian, Physical Review Letters **99**, 048102 (2007).

[66] I. Buttinoni, G. Volpe, F. Kümmel, G. Volpe, and C. Bechinger, Journal of Physics: Condensed Matter **24**, 284129 (2012).

[67] J. Palacci, S. Sacanna, A.P. Steinberg, D.J. Pine, and P.M. Chaikin, Science **339**, 936 (2013).

[68] J. Palacci, S. Sacanna, S.H. Kim, G.R. Yi, D.J. Pine, and P.M. Chaikin, Philosophical Transactions of the Royal Society A **372**, 20130372 (2014).

[69] F. Ma, S. Wang, D.T. Wu, and N. Wu, Proceedings of the National Academy of Sciences **112**, 6307 (2015).

[70] W.D. Ristenpart, I.A. Aksay, and D.A. Saville, Physical Review E **69**, 021405 (2004).

[71] W.D. Ristenpart, I.A. Aksay, and D.A. Saville, Journal of Fluid Mechanics **575**, 83 (2007).

[72] M. Trau, D.A. Saville, and I.A. Aksay, Science **272**, 706 (1996).

[73] F. Ma, X. Yang, H. Zhao, and N. Wu, Physical Review Letters **115**, 208302 (2015).

[74] P. Romanczuk, M. Bär, W. Ebeling, B. Lindner, and L. Schimansky-Geier, European Physical Journal-Special Topics **202**, 1 (2012).

[75] Z. Wang, H.-Y. Chen, Y.-J. Sheng, and H.-K. Tsao, Soft Matter **10**, 3209 (2014).

[76] I. Buttinoni, J. Bialké, F. Kümmel, H. Löwen, C. Bechinger, and T. Speck, Physical Review Letters **110**, 238301 (2013).

[77] Y. Fily and M.C. Marchetti, Physical Review Letters **108**, 235702 (2012).

[78] H.P. Zhang, A. Be'er, E.L. Florin, and H.L. Swinney, Proceedings of the National Academy of Sciences **107**, 13626 (2010).

[79] V. Narayan, S. Ramaswamy, and N. Menon, Science **317**, 105 (2007).

Chapter 2
Binding kinetics of lock and key colloids

Abstract

Using confocal microscopy and first passage time analysis, we measure and predict the rates of formation and breakage of polymer-depletion-induced bonds between lock-and-key colloidal particles, and find that an indirect route to bond formation is accessed at a rate comparable to that of the direct formation of these bonds. In the indirect route, the pocket of the lock particle is accessed by nonspecific bonding of the key particle with the lock surface, followed by surface diffusion leading to specific binding in the pocket of the lock. The surprisingly high rate of indirect binding is facilitated by its high entropy relative to that of the pocket. Rate constants for forward and reverse transitions among free, nonspecific, and specific bonds are reported, compared to theoretical values, and used to determine the free energy difference between the nonspecific and specific binding state.

In this work, Daniel J. Beltran-Villegas performed modeling and simulation work, Jun Liu provided modeling work, Greg van Anders contributed to the conceptual framework, Matthew Spellings provided custom written Python code for binding kinetics analysis, and Stefano Sacanna helped with particle synthesis and dyeing. This chapter has been modified from a published paper by the author.

Introduction

Colloidal particles mimic molecular systems in that they can form ordered crystalline phases[1], disordered glasses[2], and can even bind together tightly to form colloidal "molecules" that can themselves assemble into higher-order phases.[3] Assembling colloids into higher order phases and structures frequently requires the colloids to be anisotropic or "patchy" such that specific binding between particles leads to the formation of complex structures.[4] The interaction specificity of these building blocks limits the kinetic pathways that system can take to reach their ground state.[5] The lock and key colloidal system,[6] depicted in Fig. 2.1, forms colloidal molecules through anisotropic potential interactions; its behavior mimics the binding of drug or ligand in the binding pocket of a protein. In this system, the binding force is created by the presence of a polymer depletant, which creates an osmotic pressure that drives particles to reduce free volume by binding either nonspecifically or specifically, as shown in Fig. 2.1. The synthesis and thermodynamics of specific binding of lock and key colloids was recently reported.[6-9] Here, we report on the rich kinetics of bond formation in lock and key colloids. In particular, we find that two different pathways to a specific bond proceed at comparable rates. One occurs through a direct transition from free lock and key particles. The other, indirect, pathway, transitions through an intermediate nonspecifically bound lock and key pair, in which the key binds onto the spherical surface of the lock particle, and then, through a combination of rotations of the lock

particle, and sliding and rolling motions of the key, finds the dimple of the lock and forms a specific bond. This finding is consistent with previous simulation results.[8]

The importance of the role of nonspecific binding as a transitional step to specific binding has been demonstrated earlier for biological macromolecules,[10,11] specifically for DNA interacting with proteins, as well as in models of bacteriophage tail attachment.[12] The role of the equilibrium constant of different reaction pathways in determining clustering and self-assembly in anisotropic Janus colloids has also been shown.[13] However, there is as yet no study that measures and models the kinetics of multiple reaction pathways in a colloidal system; establishing experimentally validated, first principles understanding of this complex chemical kinetics can improve the potential for self-assembly in a variety of systems, both natural and artificial.

Toward this aim, we use confocal microscopy to measure all of the transition rate constants shown in Fig. 2.1a. We compare these results to the predictions of a diffusion-migration model of transition dynamics and find quantitative agreement for the constants that determine the relative magnitudes of the direct and indirect pathways to lock and key binding. The model is parameterized by direct measurement of the transition times from nonspecific lock-and-key pairs to free locks and keys; this determination of the net strength of the interaction potential is more accurate than what is possible from a simple theory for the depletion interaction. Model predictions include the success probability of nonspecific-to-specific binding as a function of interaction strength, and the lifetimes of indirect

binding events. We also predict the rates of formation of specific lock-and-key pairs, and of the forward and reverse rates of formation of nonspecific bonds. The latter rates determine the overall rate of formation of specific lock-and-key bonds, and, in a concentrated system, merit measurement and prediction because they control the kinetics of gel formation, which might inhibit the formation of macrocrystalline phases of lock-and-key bound pairs. From the measured rate constants, we also obtain the free energy difference between the nonspecific and specific lock-key bond, which reveals interesting effects of entropy differences between the two states.

Materials and Methods

Lock and key particles were synthesized by polycondensation and free radical polymerization of 3-trimethoxysilylpropylmethacrylate (TPM, ≥ 98%, Sigma-Aldrich), with a different fluorescent dye incorporated into each so they could be distinguished by confocal microscopy.[14] The resulting lock particles had diameter d_L = 2.38 μm ± 0.02 μm and the keys had diameter d_K = 2.14 mm $\pm$ 0.01 mm as determined by analysis of N_L = 74 and N_K = 90 particles imaged by SEM (Fig. 2.2). TEM images of the lock particles (Fig. 2.2) showed their angle of aperture to be α = 0.58 ± 0.01 radians (for N = 3 measurements). The lock particles have a zeta potential of ζ_L = -77.2 mV ± 2.22 mV; the keys have a zeta potential of ζ_K = -88.0 mV ± 2.38 mV (Malvern Zetasizer). The particular dimple shape of the lock particles is such that all six reactions shown in Fig. 2.1a occur at measureable rates, a condition that facilitates understanding the interrelationship among the six rate constants of this reaction system.

Stock solutions of 2 g/L polyethylene oxide (PEO, M_v = 600,000 g/mol, Sigma-Aldrich) at 1.5 mM NaCl (κ^{-1} = 7.9 nm) were prepared as the depletant. The radius of gyration of the PEO is estimated to be R_g = 50 nm.[15] Dilute lock and key colloid suspensions of 2 mL volume were prepared by adding corresponding amounts of 1.5 mM NaCl solution, PEO solution, 25 μL of a 1% wt tetramethylammonium hydroxide solution in water (TMAH, Acros Organics) solution and 25 μL of a 5% wt Pluronic F108 aqueous solution (Pluronic F108,

Sigma-Aldrich) such that the final volume sample was 2 mL and pH = 9. PEO concentrations ranged from [PEO] = 0 g/L to 1.4 g/L (c/c^* from 0 to 0.74, where c^* is the critical overlap concentration, $c^* = 3\,M_w/4\,\pi R_g^3\,N_A$). 300 µL of the prepared samples were placed in an 8-well chamber (Lab Tek II), covered with silicone oil to prevent evaporation, and placed on the microscope.

Polymer polydispersity was estimated by DLS measurements of hydrodynamic radius, R_h, distributions, converted to molecular weight distributions following the correlation between M and R_h by Devanand and Selser[15], and fitted to a lognormal distribution yielding a polydispersity index, PDI, of M_w/M_n = 3.29. The effect of polymer polydispersity on depletant size is estimated after the method of Kleshchanok and collaborators[16] by assuming a viscosity average molecular weight, M_v = 600,000, and PDI of 3. Specifically, following Young & Lowell,[17] and by using the Mark-Houwink equation coefficient "a" for polyethylene oxide in water obtained from Ito et al,[18] we find R_g = 48.9 nm corresponding to a polydisperse depletant radius of $r_{d,polydisperse}$ = 55.1nm, comparable to r_d = 56.7nm. Thus, we estimate an uncertainty on the depletant radius to be 2.6%, on the zeta-potential to be 2.9% and 2.7% for lock and key particles, respectively, and electrolyte concentration to be 2.4%.

To measure the kinetic rate coefficients of interaction, samples were imaged with an inverted confocal microscope (Leica TCS SP8). Two fluorescence channel imaging was performed to distinguish the two different particles. After 10 minutes, during which partial sedimentation of the particles to the coverslip occurred, time

series of two dimensional images were acquired at 1.15 frames/second at a resolution of 512 x 512 pixels^2 using a 63x oil-immersion, *NA* = 1.40 Leica objective for 30 minutes, for a total capture of 2065 images. The pixel size was 117.3 X 117.3 nm^2 and the total frame size was 60 x 60 μm^2. 2D confocal microscopy images from each channel were separately analyzed by applying a Hough transform algorithm for circle detection[19] implemented in MATLAB to find the particles' centers to a resolution of ± 14 nm. Histograms of bonded particles allowed resolution of specific, nonspecific, and free particles bonds at those with separation less than 2.2 μm, between 2.2 and 2.6 μm, and greater than 2.6 μm, respectively (Fig. 2.3). This histogram shows the presence of two bond length ranges associated with the binding state between lock and key particles. The width of these peaks can be explained by building block polydispersity (the ratio of standard deviation to average particle size for locks and keys were 7.2% and 4.4%, respectively) and by out-of-plane Brownian rotation of the particle pairs. See Appendix A for a discussion of the effects of improper identification of specific and nonspecific bonds.

Representative image sequences of kinetic binding processes are shown in Figure 2.1b and 2.1c, for both the direct formation of a lock-key specific bond, and the indirect formation, through a nonspecifically bound intermediate, respectively. Figure 2.1b shows an image sequence of a direct specific binding event: a key particle binds to the dimple of a lock particle upon finding the lock. Figure 2.1c shows a nonspecifically bound key particle diffusing on the surface of the lock particle until it binds to the dimple of the lock. Although the thermodynamics of lock

and key binding dictate the degree of binding at equilibrium – i.e. large times – the kinetic pathways by which equilibrium is achieved are complex, and require that all six reactions be resolved. This kinetic complexity is a consequence of the anisotropy of the lock, and the fact that it offers two different binding states – specific and nonspecific – to the diffusing key. We find that rate constants for all six reactions shown on Fig. 2.1a are measurable.

The relative frequency of the kinetic events shown in Figures 2.1a vary with the concentration of depleting polymer, and can be quantified by analysis of the time series of confocal microscopy images. These images are analyzed to yield the rate coefficients $k_{F\text{-}S}$, $k_{F\text{-}NS}$, $k_{NS\text{-}S}$, $k_{NS\text{-}F}$, $k_{S\text{-}NS}$, and $k_{S\text{-}F}$, as defined below. Also measured were the lifetime distribution of specifically and nonspecifically bound pairs, the mean first passage time for nonspecific pairs to passage to specific pairs, and the success probability for a nonspecific pair to transition to a specific pair.

We measure the number density of locks and keys by counting the lock and key particles in each frame for the complete image time series and time-averaging their count. We then divide this number by the volume of the region, taken to be $V = 2r_L \times A$, where A is the area of the region, A = (60 μm)^2, and $2r_L$ = 2.4 μm is the diameter of the lock particles. We also track the different events as they happen, and calculate the rates at which the different events occur, normalized by volume. From these measurements, we calculate the event rate coefficients $k_{F\text{-}S}$, $k_{F\text{-}NS}$, $k_{NS\text{-}S}$, $k_{NS\text{-}F}$, $k_{S\text{-}NS}$, and $k_{S\text{-}F}$ according to first and second order reaction kinetic processes. Specifically, the following equations for kinetic rate constants were used:

$r_{F-S} = k_{F-S}\, n_L n_K$ (1),

$r_{F-NS} = k_{F-NS}\, n_L n_K$ (2),

$r_{NS-S} = k_{NS-S}\, n_{NS}$ (3),

$r_{NS-F} = k_{NS-F}\, n_{NS}$ (4),

$r_{S-NS} = k_{S-NS}\, n_S$ (5), and

$r_{S-F} = k_{S-F}\, n_S$ (6),

where n_L, n_K , n_{NS} , and n_S denote the number densities of locks, keys, nonspecifically bound and specifically bound lock-key pairs, and $r_{F\text{-}S}$, $r_{F\text{-}NS}$, $r_{NS\text{-}S}$, $r_{NS\text{-}F}$, $r_{S\text{-}NS}$, and $r_{S\text{-}F}$ denote the rate per unit volume at which free to specific, free to nonspecific, nonspecific to specific, nonspecific to free events, specific to nonspecific and specific to free events, respectively, occur. Note the units of the rate coefficients vary depending on whether or not the binding process is uni-colloidal or bi-colloidal. The kinetic rate coefficients for the six equations are obtained by measuring the concentration of lock and key particles present (n_L and n_K, respectively, with units of μm^{-3}) and the number of nonspecific and specific lock-key bonds formed and broken over the image acquisition time.

Theory

Smoluchowski diffusion-migration model

To model the kinetics of events starting from NS to other states we use a diffusion-migration description of lock and key pair particle motion in terms of relative separation, h, defined as the surface to surface distance between particles, and relative orientation, θ, defined as the angle between the lock director and center-to-center vector between particles (Fig 2.4). The governing equation for the evolution of probability density is the Smoluchowski equation,[20] given by

$$\frac{\partial \rho(h,\theta,t)}{\partial t} = \nabla \cdot \mathbf{D}(h,\theta)\exp\left[-\frac{W(h,\theta)}{k_B T}\right] \cdot \nabla \exp\left[\frac{W(h,\theta)}{k_B T}\right] \rho(h,\theta,t) \quad (7),$$

where r is the probability density that the pair is at position (h,θ), W is the potential of mean force as a function of (h,θ), given by $W(h,\theta)= \Phi(h)+W_g(h,\theta)$, where $\Phi(h)$ is the interaction potential between particles given by a sum of repulsive electrostatic and depletion attractive potentials, $W_g(h,\theta)$ is the configurational contribution to the potential of mean force associated with the choice of coordinates at a given position (h,θ), and **D** is a diffusion tensor related to hydrodynamic interactions between lock and key in both the normal and tangential directions.[21] The Smoluchowski equation is a particular case of the more general master equation for stochastic process description. The main assumptions of this model are ergodicity and that the dispersion is dilute enough to prevent three or higher-body effects. The Smoluchowski equation can be written as

$$\frac{\partial \rho(h,\theta,t)}{\partial t} = -\nabla \cdot \mathbf{S}(h,\theta,t) \quad (8),$$

where **S** is the probability current. Transition between NS to F is taken in both experiments and theory as the separation $h=h_a$, a height at which a gap between the particles can be resolved in our system. For our system h_a = 372 nm; it is equal to the difference between the largest lock-key center-to-center separation distance used to define NS events, as defined above, and the sum of the lock and key average radii. A transition from NS to S is taken to occur at an orientation $\theta=\alpha$, with α = 0.58 radians, determined from TEM images, as above. The boundary conditions required to solve equation (7) are absorbing (probability sinks) at $h=h_a$ and $\theta=\alpha$. The last absorbing boundary condition, at $\theta=\alpha$ states that we are assuming the binding is fast once a key finds its way to this position. Previous work shows the existence of a depletion energy barrier due to sharp edges.[22] This effect was found to be minor in our calculations. The solution of equation (7) gives lifetimes for different events as well as the relative occurrence of competing events, which can be estimated from lifetime distributions for events starting in NS and ending in state B (either F or S), $w_{\text{NS-B}}(t)$, as

$$w_{NS-B}(t) = \int_{\mathbb{S}_{NS-B}} \mathbf{S}(h,\theta,t) \cdot d\mathbf{n} \quad (9),$$

where the integral is over the boundary $\mathbb{S}_{NS-B}$ between states NS and B, and d**n** is a unit vector normal to the boundary. The zeroth moment of $w_{\text{NS-B}}(t)$,

$$P_{NS-B} = \int_0^\infty dt\, w_{NS-B}(t) \quad (10),$$

is the success probability, which is the probability of crossing the boundary $\mathbb{S}_{NS-B}$ before crossing any other boundary. The success probability for a transition from

NS to S is noted here as P_S. Normalization of $w_{NS\text{-}B}(t)$ by the success probability yields,

$$p_{NS-B}(t) = \frac{w_{NS-B}(t)}{P_{NS-B}} \quad (11),$$

which is the lifetime distribution conditional to events of the same type. The first moment of $p_{NS\text{-}B}(t)$ gives us the mean first passage time, $t_{MFP|NS\text{-}B}$, of events of this kind, given by

$$t_{MFP|NS-B}(t) = \int_0^\infty dt\ t\ p_{NS-B}(t) \quad (12).$$

Alternatively, the mean first passage time for all events leaving the NS state, $t_{MFP|NS}$, is given by

$$t_{MFP|NS}(t) = \int_0^\infty dt\ t\ \left(w_{NS-S}(t) + w_{NS-F}(t)\right) \quad (13).$$

The kinetic rate constant between two states is then given by

$$k_{NS-B} = \frac{P_{NS-B}}{t_{MFP|NS}} \quad (14).$$

The predictions of the analysis were confirmed to be accurate by direct Brownian dynamics simulations with full hydrodynamic interactions using established mobility tensor for pairs of spheres.[23,24] Further detail of the model can be found in recently published work.[21]

Nonspecific interaction potential determination

The nonspecific lock-and-key interaction potential is the result of the sum of electrostatic repulsive potential, $\Phi_R(h)$, and a depletion attractive potential, $\Phi_D(h)$, as

$$\Phi(h) = \Phi_R(h) + \Phi_D(h) \quad (15),$$

where the repulsive potential is described by DLVO theory[25] as

$$\Phi_R(h) = 32\pi\varepsilon\left(\frac{d_L d_K}{d_L + d_K}\right)\left(\frac{k_B T}{e}\right)^2 \tanh\left(\frac{e\zeta_L}{4k_B T}\right)\tanh\left(\frac{e\zeta_K}{4k_B T}\right)\exp(-\kappa h) \quad (16),$$

where d_L and d_K are lock and key particle diameters, respectively, e is the solvent dielectric permittivity, k_B is Boltzmann's constant, T is the absolute temperature, e is the elemental charge, κ^{-1} is the Debye screening length, and ζ_L and ζ_K are lock and key particle zeta potentials, respectively.

The depletion potential follows an Asakura-Oosawa[26] form as

$$\Phi_D(h) = -\Pi\,\Delta V(h) \quad (17),$$

where Π is the depletant osmotic pressure and ΔV is the overlap excluded volume for depletants.

To determine the depletant osmotic pressure one needs an equation of state for the polymer solution, which can be estimated by assuming the polymer solution to be ideal (i.e. $\Pi_{ideal}=n_{PEO}k_B T$, where n_{PEO} is the PEO number density). Nonetheless there is an uncertainty in parameters in equations (15)-(17) which can change the shape and well depth of the potential such as PEO molecular weight polydispersity, as explained above, and measurement uncertainty for electrolyte concentration and zeta potential, as discussed below.

Results and Discussion

Because the theoretical form of the potential energy, $\Phi(h)$ – which combines both electrostatic and depletion contributions – is uncertain[27], due to the experimental uncertainty of the parameters that it depends on, we determine it from the measurements of the lifetime distributions for NS-F events. To accomplish this we compare the lifetime distributions for NS-F events estimated from the diffusion-migration model for varying interaction strengths. In Figure 2.5a, we show the experimental data for [PEO] = 1.0 g/L, and the NS-F lifetime distribution corresponding to the interaction strength that minimizes the weighed sum of squared errors between the experimental and modeled lifetime distributions. This was repeated for all the different [PEO], giving interaction strengths shown as the minimum of the potential energy, $\Phi_{\min}$, in Figure 2.5b. Although the trend for the potential energy inferred from the lifetime of non-specific bonds on the colloid surface agrees with an *a priori* estimation from theory, there are quantitative differences. In this system, for the range of PEO concentrations studied, the minimum of the pair potential between lock and key varies from about 1 to 3 $k_B T$. Such analysis of the lifetime of non-specific bonds is a simple way to parameterize colloidal pair potential for comparison to theory and simulation.

To determine depletant osmotic pressure we fit estimates of lifetime distributions for NS-F events, using the diffusion-migration model (equation (7)), for varying values of P to lifetime distributions obtained from experiment for each depletant concentration. This fitting process is based on the minimization of a sum

of square errors, weighed by the inverse of the experimental variance, between the experimental quantity and the model-estimated quantity. We estimate P using average values of ζ, κ^{-1} and R_g to fix the shape of the potential. In Figure 2.5a we show results of lifetime distributions at [PEO] = 1.0 g/L from experiment and diffusion-migration model using the depletant osmotic pressure that minimizes the weighed sum of square errors. To compare with predictions using an ideal polymer solution we allow the PEO molecular weight (which changes R_g), zeta potential, ζ, and Debye screening length κ^{-1}, to vary by 5%. We find two extreme cases where the potential well depth is maximal and minimal. In Figure 2.5b we show the value of the minimum of the nonspecific interparticle potential, $\Phi_{\min}$, as a function of [PEO] from this fitting process alongside the values obtained from the ideal solution equation of state estimations (average, low and high estimates) for comparison. We find that the fitted potentials are within the variability of the ideal polymer theory given the uncertainty of its parameters.

The determination of the potential $\Phi(h)$ from the lifetime distribution for NS to F events fully specifies the diffusion-migration model. From it we compute the NS-S event lifetime distributions, $p_{\text{NS-S}}(t)$, shown for the particular case of 1.0 g/L depletant on Figure 2.6a, the mean first passage times for the NS to S and NS-F transitions (Figure 2.6b) and success probabilities, P_S, (Figure 2.6c) for NS to S. These quantities are of particular interest because they probe how increased attraction between lock and key affects the dynamics of nonspecifically bound dynamics, leading in some cases to a transition from this bond to a specific bond.

The lifetime distribution of the NS – S event, $p_{NS\text{-}S}(t)$, plotted in Figure 2.6a, decays non-exponentially with time. Keys that successfully transition from NS to S spend a considerable time nonspecifically bound to the lock surface. This observation is consistent with previous findings showing the potential between lock and key has a secondary minimum in NS configuration.[8] For example, 7.3% of the trajectories of keys bound nonspecifically to locks survive 6.1 s or more. By comparison, the time for a key colloid to diffuse a distance equal to its own radius is 5.7 s. These long trajectories endure because of the strength of the nonspecific depletion bond between the lock and key; unless Brownian fluctuations induce the nonspecific bond to break and for the key to become free, it continues surface diffusion on the lock until specific binding occurs.

The diffusion-migration model captures this physics with very good quantitative agreement, except at long times. The long-time disagreement between experimental and modeled lifetime distributions in Fig. 2.6a can also be seen in Figure 2.5a and is attributed to two possible factors. First, events with longer lifetimes have larger errors because they occur less frequently for an experiment of finite duration. However, this explanation is incomplete because deviation is systematically towards larger probabilities at long times for all concentrations and is outside the error bars of the experiments. Second, possible three-body and greater interactions in our system, especially at late times and high concentrations of PEO, are expected to slow down the kinetics of specific binding. These multiple-particle interactions occur, for example, when a nonspecifically bound lock-and-key

pair encounters and binds with another particles, which amounts to minor qualitative differences. These multiparticle interactions are rare at the depletant concentrations studied here, but when they occur, they should produce longer NS-S and NS-F event lifetimes. For example, a key diffusing on the surface of a lock might be approached by another particle and interact with it, delaying its motion toward the dimple, or a key might interact with an occupied lock particle. Our diffusion-migration model assumes only pair particle interactions. Apart from this long-time deviation, the experimental and theoretical binding time distributions agree with each other for the range of [PEO] considered in our experiments.

As [PEO] is increased from 0.3 g/L to 1.4 g/L, the average event lifetime of NS-F events, $t_{\mathrm{MFP|NS\text{-}F}}$, increases from 2.9 s to 6 s, and $t_{\mathrm{MFP|NS\text{-}S}}$ increases from 1.8 s to 2.9 s, as shown experimentally and confirmed by the model. From Fig 2.6b, the average transition times for NS-F events are longer than those for NS-S events. Because NS-F and NS-S processes compete, the average time for each process is dominated by the faster of the two, while the relative rates control the relative numbers of each transition type. The observed modest difference in average times between NS-F and NS-S is due to different shapes of the probability distributions for the transition times. While the NS-F process is essentially Poissonian, the NS-S process is non-Poissonian due to the finite distance to binding over which surface diffusion must occur, which creates an enhanced population of quickly-binding states, relative to a Poissonian process. This trend is not as obvious in the experimental data, which show longer NS-S times than in model predictions.

Discrepancies here are a consequence of the disagreement in the long-time tail in lifetime distributions, as explained above in the context of three-body interactions. This means there are a number of long-lasting events that shift average lifetimes, especially for NS-S events. Comparison of the lifetime distributions for NS-F (Fig 2.5a) and NS-S (Fig 2.6a) confirms that the former distribution generally falls above the latter, with this trend however becoming less clear at long times.

In Figure 2.6c, we plot the experimental and model success probability P_S, defined as the probability that a key will specifically bind to the lock dimple given that it is initially nonspecifically bound to the lock surface versus polymer concentration. Our experiments show that as [PEO] is increased from 0 g/L to 1.2 g/L, P_S increases from 7.6 % to 17.3 %. Success probabilities extracted from our diffusion model are in good agreement with our experimental success probabilities for [PEO] below 1.4 g/L. As [PEO] increases, we expect that more nonspecifically bound lock and key pairs will specifically bind to each other, because keys will have more time to perform the successful search for the lock dimple. As the time that the key remains on the surface of the lock increases, as discussed above, so does the probability of NS-S binding between the lock and key particle. For this last polymer condition, we observe a large deviation in the experimental success probability from the other experimentally determined values and from the modeled result, which can be explained by the inapplicability of our diffusion model for $N_L > 1$, $N_K > 1$ multiparticle interactions (c.f. Fig 2.7 for evidence of multiparticle interactions at [PEO] = 1.4 g/L).

We now report the kinetic rate coefficients for the NS-S reaction, as well as the five others shown in Figure 2.1a, as obtained by measuring the concentration of lock and key particles present (n_L and n_K, respectively, with units of μm^{-3}) and the number of nonspecific and specific lock-key bonds formed and broken over the image acquisition time, as described above. We predict the NS-F and NS-S rate constants using the diffusion-migration model explained previously and computed using equation (14).

We find that as [PEO] is increased from 0 g/L to 1.4 g/L, the rate coefficient for nonspecific lock-key bond formation, $k_{F\text{-}NS}$, remains roughly constant at $k_{F\text{-}NS}$ = 6.6 ± 0.5 mm^3/s (Figure 2.8a). This is expected, since this rate is diffusion controlled and a lock-key collision counts as a binding event forming a nonspecific "bond," which is ephemeral, unless depletion is present to slow breakage of this "bond." The rate coefficient for direct lock-key bond formation, $k_{F\text{-}S}$, likewise remains constant for polymer concentrations ranging from 0 g/L to 1.2 g/L at a value of 0.67 ± 0.12 mm^3/s. These rate constants do not change with polymer concentration because the rate of these events depends on the collisional dynamics of the lock and keys, which for a short range potential studied here, is independent of potential strength. Free lock and key particles may collide with each other at the spherical surface of the lock or at the dimple of the lock particle, which has an angle of aperture a, and thus occupies a fraction $f = (1 - \cos\alpha)/2$ of the lock surface area. The Smoluchowski collision rate between two spheres of unequal size r_L and r_K is given by $k = 2k_BT\{1/r_L + 1/r_K\}(r_L + r_K)/3\mu$.[25] Here, k_B is Boltzmann's

constant, T is temperature, μ is viscosity, and r_L and r_K are the lock and key radii, respectively. For our system, T = 293 K, μ = 1.002 x 10^{-3} Pa s, r_L = 1.19 μm, and r_K = 1.07 μm, yielding a collision rate of 10.8 $\mu m^3/s$. On Figure 2.8a, we compare the measured rate coefficients for F - NS and F -S lock-key binding to Smoluchowski collision rates, given by $k_{F-NS} = (1-f)\,k$ and $k_{F-S} = f\,k$. The agreement is satisfactory.

The observation of a finite rate coefficient of direct binding in the weak interaction limit is consistent with the study's definition of direct binding – the lifetimes of these weakly interacting cases are short, and the time resolution of our measurements was constrained by our frame capture rate of 1.15 fps. Some disagreement between the theoretical collision rate and experimental values might be expected due to the quasi-2D nature of our system, because the lock and key particles are close to the coverslip. This implies that at any given time, there is a fraction of the surface area of these particles that cannot interact with other particles due to their proximity to the glass surface. Another factor to be considered is the effect of recently broken NS pairs that can bind faster than remote or far-away F pairs, although this effect would increase our theory predictions making agreement worse. However, the comparison of Figure 2.8a indicates that proximity and spatial correlation effects are not great.

In Figure 2.8b we show that the rate coefficient for unbinding of nonspecifically bound locks and keys, $k_{NS\text{-}F}$, decreases from 0.42 s^{-1} to 0.14 s^{-1} as [PEO] is increased from 0.3 g/L to 1.4 g/L, showing increased difficulty for keys to

unbind from the lock at higher depletant concentration. We also observe that the rate coefficient for indirect specific binding, $k_{NS\text{-}S}$, is insensitive to changes in [PEO], as seen on Figure 2.8b, remaining constant near a value of 0.064 ± 0.006 s^{-1}. The NS-S binding rate coefficient is independent of depleting polymer concentration due to the insensitivity of the surface diffusivity of keys on locks to small changes in surface-to-surface separation.[21,28] The NS-S binding rate, on the other hand, depends on the concentration of NS-bound lock and key pairs, which is a function of polymer concentration.

In the particular lock and key system analyzed here the strength of the specific bond is not so strong as to preclude unbinding during the long durations of the experiments. In Figure 2.8c, we plot the measured S-NS and S-F event rate coefficients against polymer concentration. As depleting polymer concentration increases, the experimental rate coefficients for both specific unbinding processes decrease; the specific-to-nonspecific rate coefficients decreases from 0.4 s^{-1} to 0.07 s^{-1} for [PEO] equal to 0.3 g/L and 1.2 g/L, respectively, and specific-to-free rate coefficients decrease from 0.21 s^{-1} to 0.02 s^{-1} for [PEO] equal to 0.3 g/L and 1.2 g/L, respectively. The decrease in specific unbinding rate coefficients can be explained by an increase in the specific binding energy as [PEO] is increased. As binding energy increases, it becomes more difficult for key particles that are specifically bound to the lock dimple to unbind, and they remain in specific lock-key configuration for longer before unbinding.

While we can measure the rate constants for breaking a lock-key specific bond, shown in Figure 2.8c, either to form a free pair or a nonspecifically bound one, a theoretical estimation of these rates would require intimate knowledge of both the 3-dimensional dependence of potential energy for the key in the pocket and hydrodynamic interactions for this geometry, which is not readily available. One thing to notice at this point is the fact that details of the shape of the lock pocket are not required to explain kinetic events in the direction of NS to S. This insensitivity is due to the nature of NS-S binding which is the result of diffusion of a key on the surface of the lock until the lip of the pocket is found, after which binding occurs faster than surface diffusion and the binding rate is not sensitive to the geometric details and complex hydrodynamics as the key enters into the pocket. The reverse process of escape from the pocket (ie. from S to NS), however, involves more crucially the non-spherical shape of this pocket, the modeling of which is beyond the scope of this work.

Rate constants determined from transient experiments as explored here are related to the equilibrium behavior of the reactions involved. In particular we can relate kinetic rate constants to equilibrium constants, and obtain the equilibrium free energy difference between the nonspecific and specific lock-key bond from the kinetics. At equilibrium, association and disassociation rates between free, nonspecific and specific rates are equal. This yields the relations

$k_{F-NS}\, n_L\, n_K = k_{NS-F}\, n_{NS}$ (18),

$k_{F-S}\, n_L\, n_K = k_{S-F}\, n_S$ (19), and

$k_{NS-S}\, n_{NS} = k_{S-NS}\, n_S$ (20) ,

which imply the following relationship between kinetic rates: $k_{NS-S}/k_{S-NS} = k_{NS-F}\, k_{F-S}/k_{F-NS}\, k_{S-F}$. At equilibrium this ratio is equal to the concentration ratio of specific to nonspecific pairs, n_S/n_{NS}. Equilibrium also requires this ratio to be $n_S/n_{NS} = \exp(-\Delta F_{NS-S}/k_B T)$. Thus, we can obtain the free energy difference between the nonspecific and specific state, ΔF_{NS-S}, for all [PEO] by taking the ratio of rate constants as

$\Delta F_{NS-S} = -ln\left(\frac{k_{NS-S}}{k_{S-NS}}\right)$ (21), or

$\Delta F_{NS-S} = -ln\left(\frac{k_{NS-F}\, k_{F-S}}{k_{F-NS}\, k_{S-F}}\right)$ (22),

where the difference between equations (21) and (22) is simply the path one NS pair can take to get to S (c.f Fig 2.1a).

A similar relation can be made to obtain the free energy difference between F to NS from the equation (18) as $n_{NS}/n_L n_K = k_{F-NS}/k_{NS-F}$. Equilibrium for this reaction requires $n_{NS} n_0/n_L n_K = \exp(-\Delta F_{F-NS}/k_B T)$, where n_0 is a reference concentration. As a reference concentration we assume that one particle occupies the volume that defines the nonspecific state, $V_{NS} = 4\pi(1-f)(R'^3 - R^3)/3$, where f is defined above, $R = r_L + r_K$, and $R' = R + h_a$; that is, $n_0 = 1/V_{NS}$. The free energy difference between F and NS states is

$\Delta F_{F-NS} = -ln\left(\frac{k_{F-NS} n_0}{k_{NS-F}}\right)$ (23).

In Fig 2.9, we plot the NS-to-S free energy difference obtained from experiment. We measure the free energy difference between NS and S two different

ways: we can take the ratio of the NS-S and S-NS rate constants (direct measurement) using equation (21) or the product of the ratios of the four reactions (indirect measurement) using equation (22). The free energy difference between NS and S decreases from $\sim 2\ k_B T$ to 0 as [PEO] increases from 0 g/L to 1.4 g/L. Moreover, direct and indirect measurements of this difference are in agreement with each other, which serves as a thermodynamic consistency check for the measurements made.

Interestingly, the free energy measurements show that at depletant concentrations equal to 1 g/L or below, the nonspecific binding state is favored over the specific binding state. For [PEO] = 1.2 g/L and 1.4 g/L, the free energy difference between NS and S is close to zero, implying no preference between NS and S binding. Given the expected stronger potential of interaction for specifically bound pairs, the preference for nonspecific pairs seems counterintuitive. Nonetheless the free energy estimated above includes contributions of both the potential energy of interaction and the associated entropy of each type of bond. Because the (energetically) weaker nonspecific bond is more prevalent, the entropy of this bond (as related to the nonspecific binding volume) must be much higher than that of the specific bond, as is indeed the case. In this colloidal system, the entropic penalty associated with the smaller number of particle configurations allowed for the specific binding state is large enough to favor nonspecific binding for [PEO] below 1.0 g/L.

This discussion shows the critical role of entropy on both the equilibrium and kinetic behavior of lock and key binding specifically, and for anisotropic colloids in general. For lock and key binding the entropy is determined by the shape of the lock pocket relative to the key; the transition PEO concentration determining the point at which specific binding is favored relative to nonspecific binding would therefore certainly depend on complementarity between the key and pocket shape. We can therefore envisage that certain pocket shapes – different than the one studied here (c.f. Figure 2.2) – might lead to potential energy and entropy changes upon binding that would combine to produce a more favorable free energy change for the specific bond, relative to the non-specific bond, than reported in Figure 2.5. Future work to generate a pocket-shape dependent free energy landscape – either by simulation or experiment – would be an interesting means to evaluate the role of shape complementarity on the energetic and entropic contributions to binding in this model lock-and-key system.

Figure 2.9 also shows the free energy difference between F and NS obtained from experiment and modeling. This free energy difference is obtained from the ratio of rate constants (see Equation (23)) and the reference concentration. (Note that the reference concentration is independent of [PEO]. Therefore, relative changes along the curve are not a function of the choice of reference.) Our experiments indicate that the free energy difference between F and NS decreases with increasing [PEO], from a value of 0.7 $k_B T$ at 0.3 g/L to -0.6 $k_B T$ at 1.4 g/L. The corresponding free energy difference obtained from our modeling, using equation

(23) and rate constants using the diffusion-migration model for $k_{NS\text{-}F}$ and Smoluchowski collision rates for $k_{F\text{-}NS}$, is also shown on Figure 2.9 and is in very good agreement with our experiments. Absolute values of the NS-F free energy depend on the particular choice of reference concentration. Therefore, the preference of NS over F, as indicated by the sign of the free energy, will ultimately depend on the total particle concentration of the system.

Conclusions

We have shown that specific lock-and-key binding occurs through two different kinetic pathways: a direct pathway from free particles to specifically bound ones and an indirect pathway involving a key particle nonspecifically bound to the spherical lock surface, which transitions by surface diffusion to a specific bond. We quantified lock-and-key binding kinetics and extracted event rate coefficients for the two binding pathways, demonstrating the importance of nonspecific binding pathways for the self-assembly of anisotropic particles. From a diffusion-migration analysis we fit the lifetime event distributions from nonspecifically bound to free particles, and thereby obtained experimentally derived estimates of the attractive interaction between particles as a function of depleting polymer concentration. Predicted rates of nonspecific-to-specific (NS-S) lock-key binding, as well as distributions of transition times for nonspecific to free particles (NS-F) and nonspecific-to-specific binding were found to agree with the experimentally measured quantities. From the measured rate constants we computed free energy differences between different states of the system. We found that nonspecifically

bound pairs are preferred to specifically bound pairs for depletant concentrations below 1.0 g/L, due to the large entropy penalty for formation of the specific bond relative to that for the nonspecific bond. Similar entropy penalties are well known to limit binding affinities in highly specific protein-ligand interactions.[29] The measurements of lock-key binding kinetics is a starting point, not only for understanding more complex binding events in biology, but also for determining rates of formation of complex colloidal materials involving particles with anisotropic interactions.

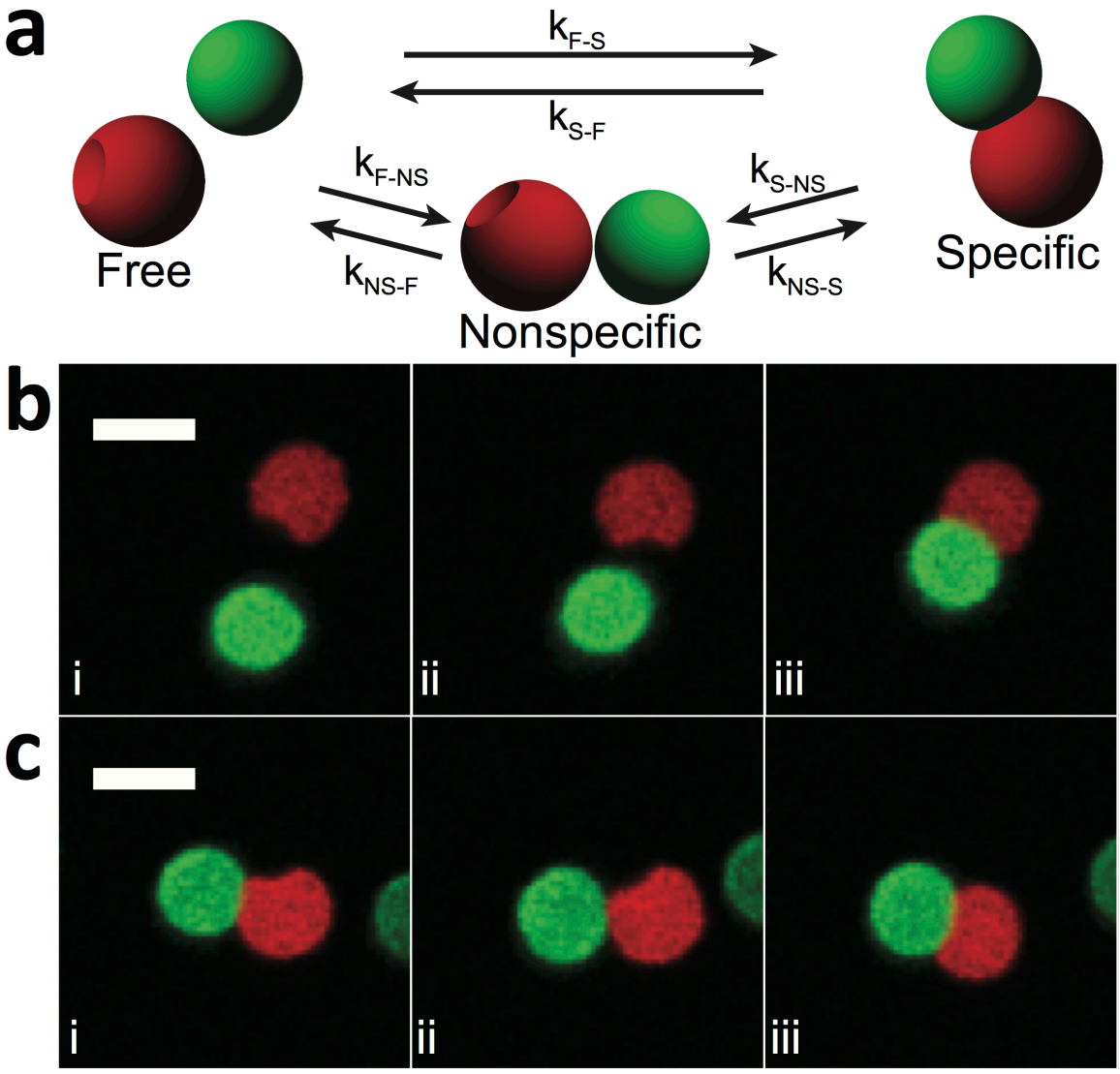

Figure 2.1 (a) Kinetic pathways of lock and key colloidal particle binding. (b) Free-to-specific, direct binding event. Scale bar 3 μm. 872 ms between frames. (c) Transition from nonspecific to specific binding. Scale bar 3 μm. 1.74 s between frames.

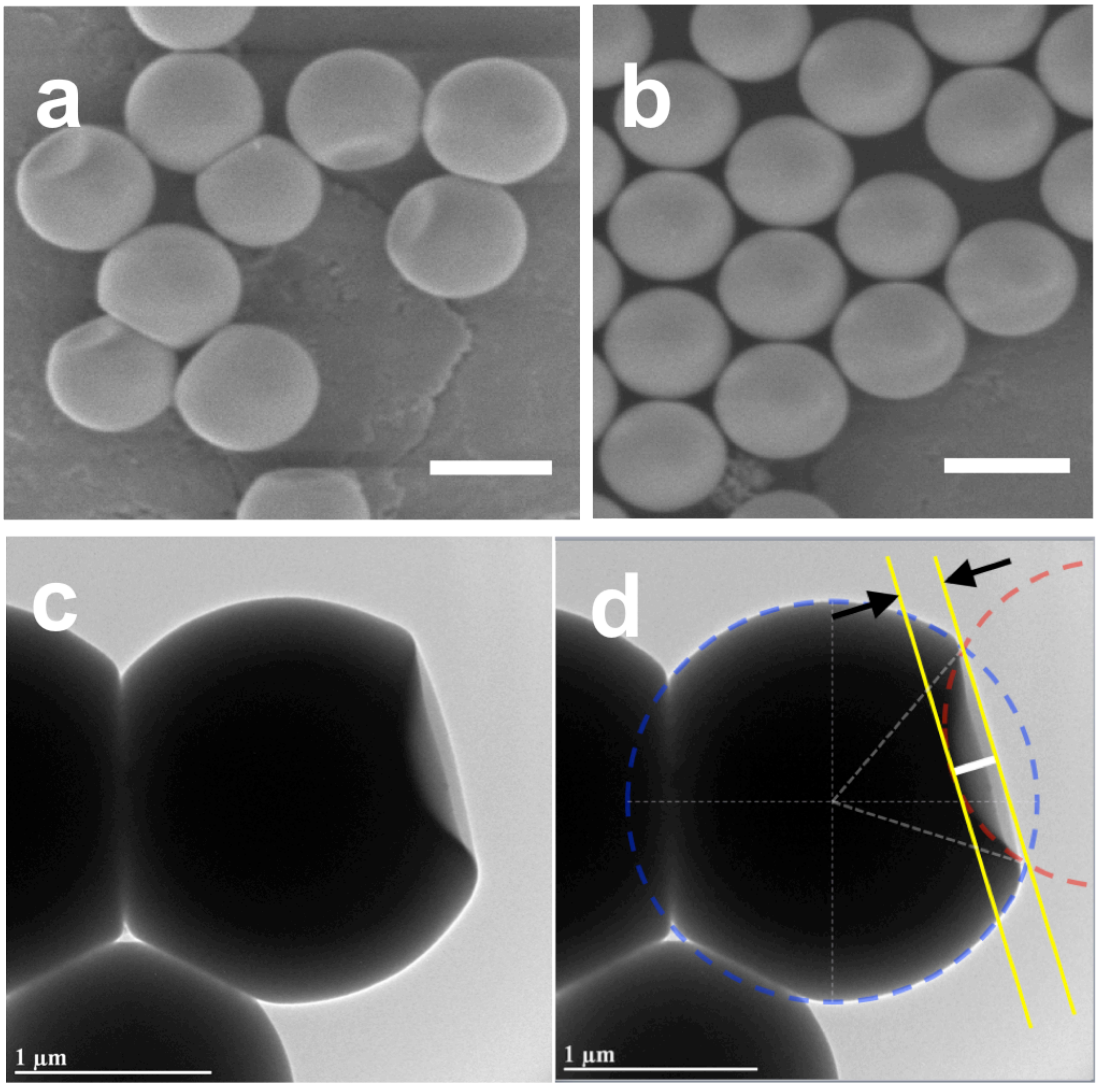

Figure 2.2 *Images of lock and key particles:* Panels (a) and (b): SEM images of the lock and key particles. The lock particles, panel (a), have diameter d_L = 2.38 µm ± 0.02 µm (N = 74) and the key particles, panel (b), have diameter d_K = 2.14 µm ± 0.01 µm (N = 90). Scale bars: 2 µm. Panel (c) shows a TEM image of a lock particle; on panel (d) the curvature of the dimple (dotted red line) and the depth of the dimple δ (solid white line) are shown. The pocket of the lock particle has angle of aperture a = 0.58 ± 0.01 radians (N = 3).

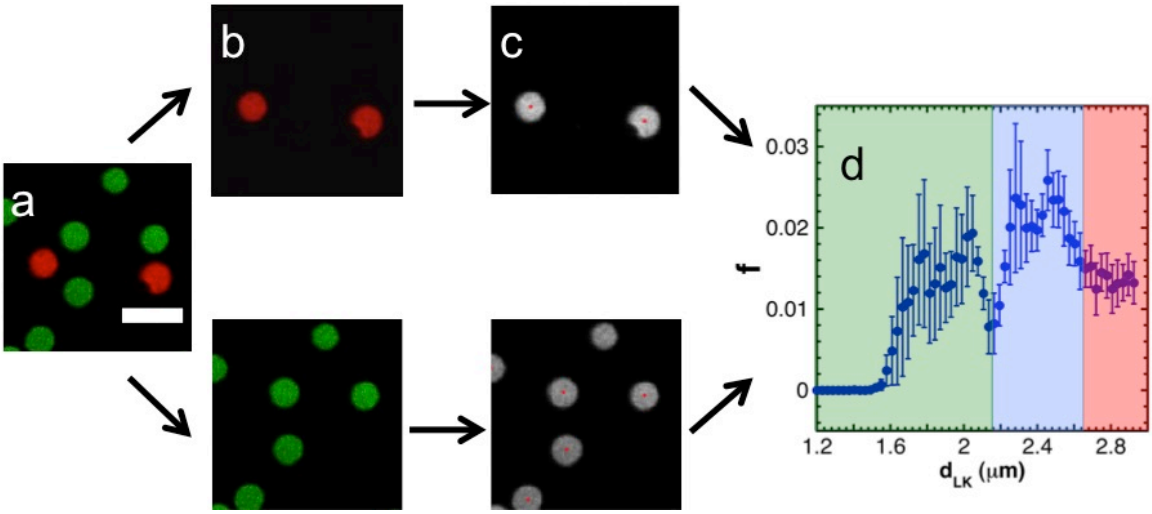

Figure 2.3 *Confocal image analysis and sample bond length distribution:* Panel (a) shows a region of a two-channel confocal microscopy image of lock and key particles. Scale bar 5 μm. We split the confocal image into its two channels, where locks are red and keys are green (panels (b)), and find the centers (red dots) of the lock and key particles independently (panels (c)) using Hough transforms. Panel (d) shows a histogram of the bond lengths between the centers of lock and key particles for N =3 samples at [PEO] = 1.4 g/L. The green region denotes specifically bound lock-key pairs, the blue region nonspecifically bound pairs, and the red region denotes free locks and keys.

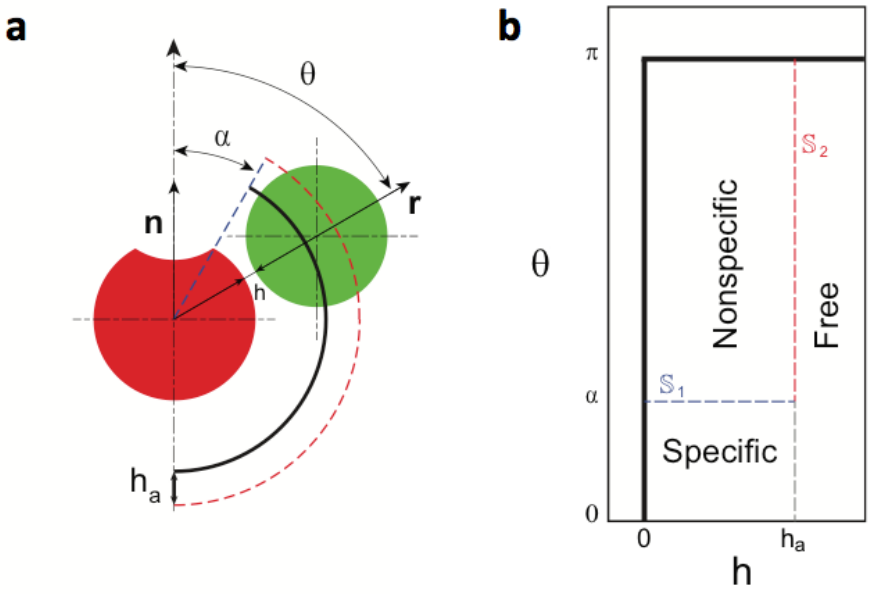

Figure 2.4 *Smoluchowski diffusion-migration modeling:* (a) Schematic of lock-key pair and relevant variables for diffusion-migration modeling. (b) Phase space in the *θ-h* plane showing the regions where specific (S), nonspecific (NS), and free (F) configurations are present.

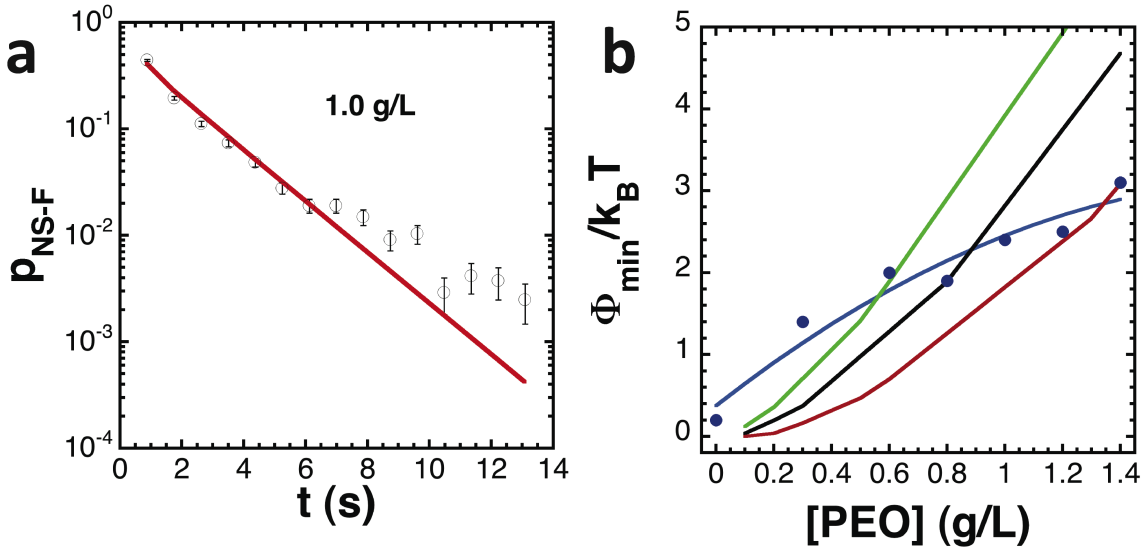

Figure 2.5 (a) NS to F event lifetime distribution for [PEO] = 1.0 g/L from experiments (symbols) and theory (line), to yield the depletant osmotic pressure that minimizes the weighed sum of squared errors. (b) Nonspecific potential energy minima obtained from this method plotted against depleting polymer concentration. The blue curve is polynomial fit to the nonspecific binding energies. The black, red, and green lines correspond to usage of ideal depletant equation of state ($\Pi_{ideal}=n_{PEO}k_BT$) allowing for variability in potential energy parameters, for average, low and high estimates, respectively.

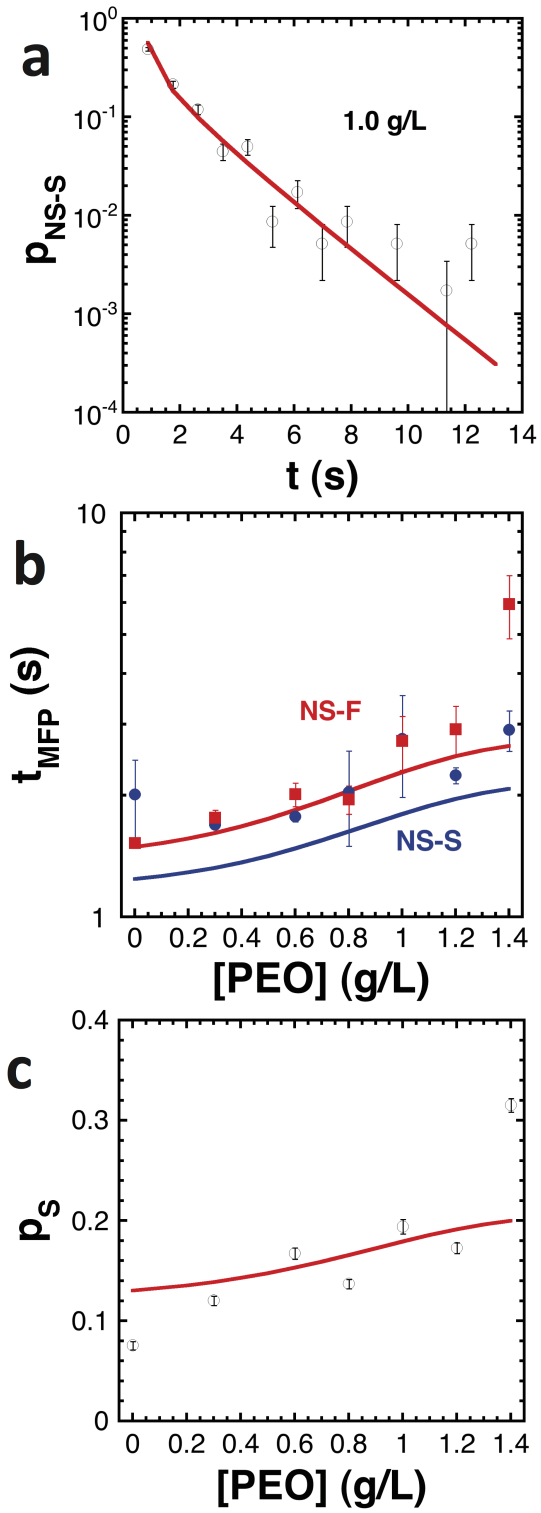

Figure 2.6 (a) NS to S event lifetime distribution for 1.0 g/L. Open symbols denote experimental results; the red line is the best-fit of theory result. (b) Mean first

passage times for NS-F (red filled squares) and NS-S (blue filled circles) events plotted against [PEO]. Model results are denoted by red (NS-F) and blue (NS-S) lines. (c) Success probability of NS-to-S binding. Experimental results are denoted by open symbols; model results are shown as a red line.

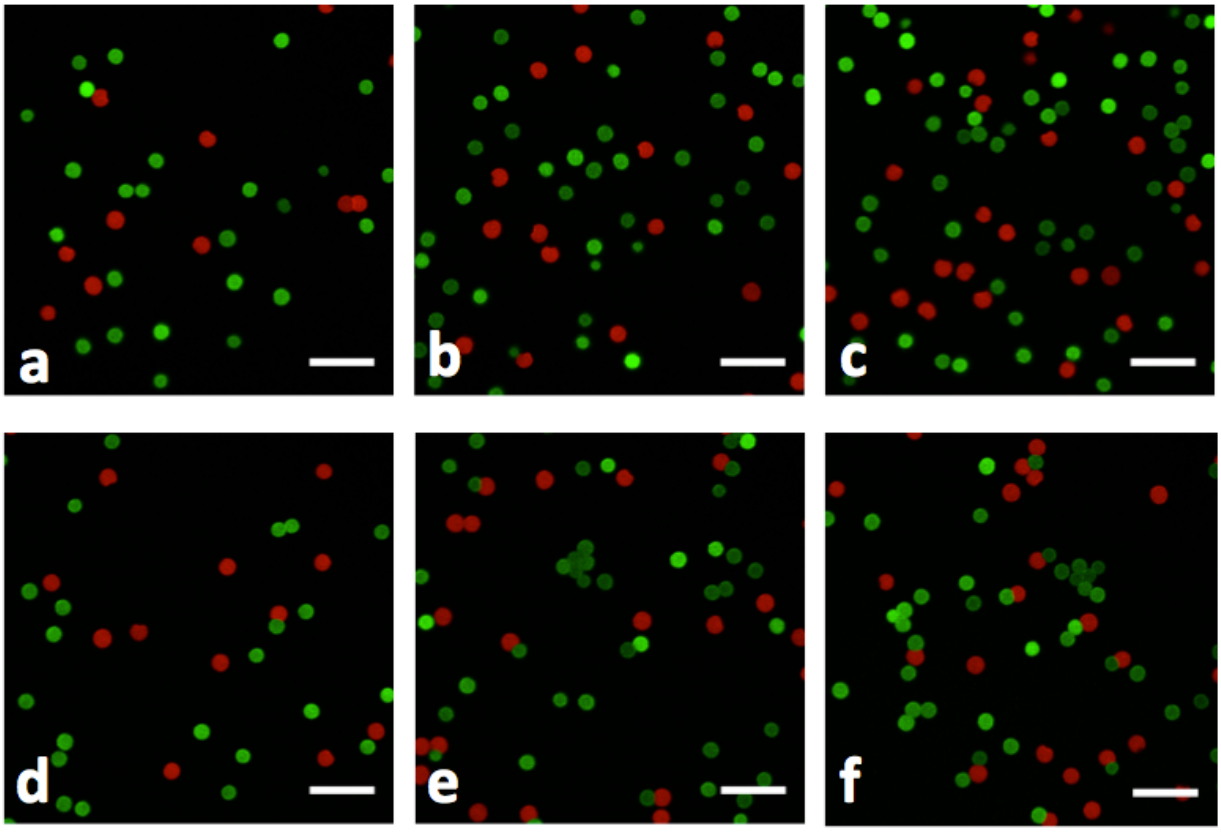

Figure 2.7 *Multiparticle interactions:* Experimental images for [PEO] = 0.6g/L (panels (a) – (c)) and [PEO] = 1.4g/L (panels (d) – (f)) for different times in the experiment where locks are shown as red particles, keys as green particles. Scale bar on all images is 10 mm. Panel (a) is taken at t=0 s, (b) at t=872 s and (c) at t=1744 s. Panel (d) is taken at t=0 s, (e) at t=872 s and (f) at t=1744 s.

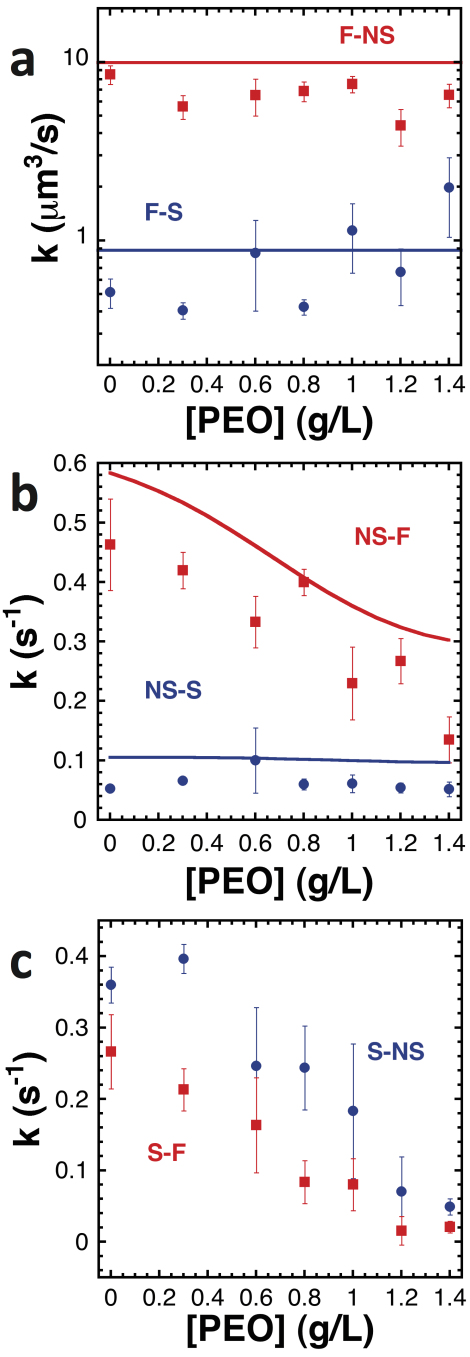

Figure 2.8 (a) Rate constants for F-NS (red filled squares) and F-S (blue filled circles) are plotted against [PEO]. Collisions rates from Smoluchowski collision theory are shown as red and blue lines, respectively. (b) Rate constants for NS-F (red filled squares) and NS-S (blue filled circles). Modeled rate constants are shown as red and blue lines, respectively. (c) Rate constants for S-NS (blue filled circles) and S-F events (red filled squares).

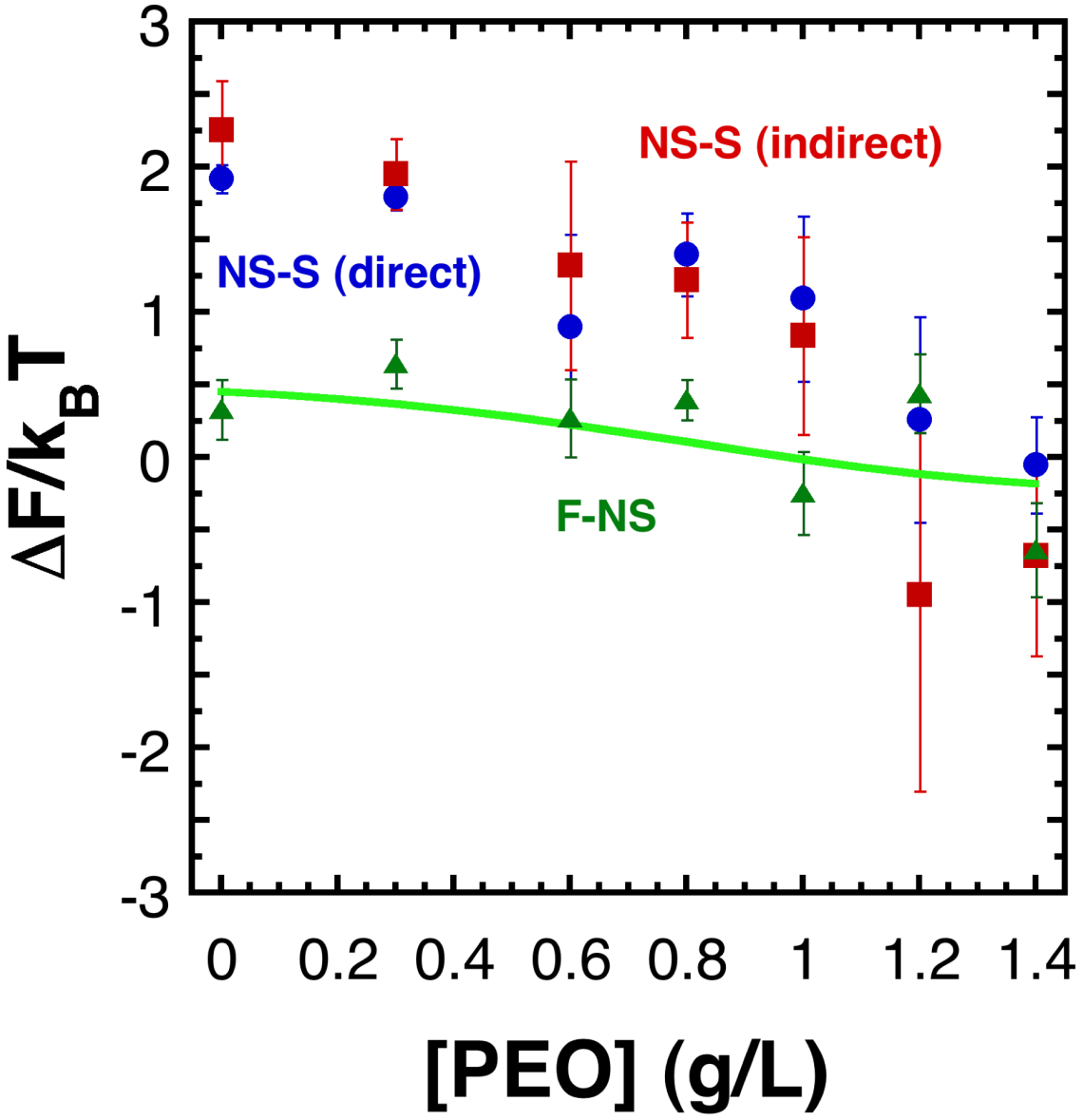

Figure 2.9 Free energy differences between nonspecific and specific lock-key binding states are shown as blue filled circles (directly measured) and filled red squares (indirect measurement). The free energy difference between free and nonspecific binding is shown as filled green triangles; the green line represents the free energy difference as obtained by our model.

References

[1] V.J. Anderson and H.N.W. Lekkerkerker, Nature **416**, 811 (2002).

[2] E.R. Weeks, Science **287**, 627 (2000).

[3] Y. Wang, Y. Wang, D.R. Breed, V.N. Manoharan, L. Feng, A.D. Hollingsworth, M. Weck, and D.J. Pine, Nature **491**, 51 (2012).

[4] S.C. Glotzer and M.J. Solomon, Nature Materials **6**, 557 (2007).

[5] E. Jankowski and S.C. Glotzer, Soft Matter **8**, 2852 (2012).

[6] S. Sacanna, W.T.M. Irvine, P.M. Chaikin, and D.J. Pine, Nature **464**, 575 (2010).

[7] S. Sacanna, W.T.M. Irvine, L. Rossi, and D.J. Pine, Soft Matter **7**, 1631 (2011).

[8] G. Odriozola, F. Jiménez-Ángeles, and M. Lozada-Cassou, The Journal of Chemical Physics **129**, 111101 (2008).

[9] G. Odriozola and M. Lozada-Cassou, Physical Review Letters **110**, 105701 (2013).

[10] O.G. Berg and P.H. von Hippel, Annual Review of Biophysics and Biophysical Chemistry **14**, 131 (1985).

[11] O.G. Berg, Biophysical Journal **47**, 1 (1985).

[12] V.A. Bloomfield and S. Prager, Biophysical Journal **27**, 447 (1979).

[13] Q. Chen, J.K. Whitmer, S. Jiang, S.C. Bae, E. Luijten, and S. Granick, Science **331**, 199 (2011).

[14] S. Sacanna, W.T.M. Irvine, L. Rossi, and D.J. Pine, Soft Matter **7**, 1631 (2011).

[15] K. Devanand and J.C. Selser, Macromolecules **24**, 5943 (1991).

[16] D. Kleshchanok, R. Tuinier, and P.R. Lang, Langmuir **22**, 9121 (2006).

[17] R.J. Young and P.A. Lovell, *Introduction to Polymers, Third Edition* (Taylor & Francis, 2011).

[18] S. Kawaguchi, G. Imai, J. Suzuki, A. Miyahara, T. Kitano, and K. Ito, Polymer **38**, 2885 (1997).

[19] P. Kierkegaard, Machine Vision and Applications **5**, 249 (1992).

[20] H. Risken and T. Frank, *The Fokker-Planck Equation: Methods of Solutions and Aplications* (Springer, 1996).

[21] D.J. Beltran-Villegas, L. Colón-Meléndez, M.J. Solomon, and R.G. Larson, Journal of Colloid and Interface Science **463**, 242 (2016).

[22] A.D. Dinsmore, A.G. Yodh, and D.J. Pine, **383**, 239 (1996).

[23] D.J. Jeffrey and Y. Onishi, Journal of Fluid Mechanics **139**, 261 (2006).

[24] S. Kim and S.J. Karrila, *Microhydrodynamics: Principles Amd Selected Applications* (Dover, 2005).

[25] W.B. Russel, D.A. SAVILLE, and W.R. Schowalter, *Colloidal Dispersions* (Cambridge University Press, Cambridge, 2009).

[26] S. Asakura and F. Oosawa, Journal of Polymer Science **33**, 183 (1958).

[27] P.J. Lu, E. Zaccarelli, F. Ciulla, A.B. Schofield, F. Sciortino, and D.A. Weitz, Nature **453**, 499 (2008).

[28] M.A. Bevan and D.C. Prieve, The Journal of Chemical Physics **113**, 1228 (2000).

[29] C.A. Chang, W. Chen, and M.K. Gilson, Proceedings of the National Academy of Sciences **104**, 1534 (2007)

Chapter 3
Effect of shape complementarity on the free energy of binding of lock and key colloids

Abstract

Using confocal microscopy, we measure the free energy of formation of specific lock-key bonds to probe the role of shape complementarity on the formation of lock-key colloidal molecules. We find that the free energy of formation of lock-key bonds is asymmetric around a perfect match between the key and lock cavity, with smaller free energies observed for key-to-lock cavity size ratios less than one relative to size ratios greater than one. The free energies of formation are derived from measurements of the equilibrium fractional occupation of locks for fixed initial concentration of lock and key particles. The lock dimple geometry of the particles was characterized using atomic force microscopy. We find that keys with key-to-lock dimple ratio equal to $\delta = 0.7$ and $\delta = 0.9$ have the most favorable specific lock-key bond free energies of formation. Our results suggest that the formation of specific lock-key bonds is promoted when the key particle is smaller than the dimple, in agreement with previous simulation and modeling work showing that lock-key specific bond formation in this region is more entropically favored than for larger keys due to better shape recognition between the particles.

In this work, Daniel J. Beltran-Villegas and Greg van Anders contributed to the conceptual framework and helped design research regarding lock and key binding and shape complementarity.

Introduction

Equilibrium colloidal self-assembly occurs as a spontaneous thermodynamic process driven by the minimization of free energy. In systems of colloidal particles with isotropic interactions, such as colloidal polymer spheres, close-packed assemblies are the free-energy minimum at high volume fraction. The formation of assemblies with complex symmetries, such as non-close packed colloidal assemblies, can be achieved by introducing anisotropic pair potential interactions into the system[1-8]. However, systems of particles with anisotropic interactions can be prone to kinetic arrest and metastability.[9-11] Kinetic trapping is observed in systems where bonds formed between particles in metastable configuration do not easily break[12]. There is interest in developing design rules for the assembly of anisotropic building blocks so as to enhance the formation of structure while avoiding kinetically arrested phases [6,13-18]. The development of such rules requires thorough understanding of the free energy landscape of interaction[19,20] in anisotropic particle systems.

In systems where self-assembly is driven by the depletion interaction, the system equilibrates into states at which depletant particles maximize their free volume[21]. The depletion interaction originates due to the exclusion of small cosolute particles from the surface of large particles or surfaces in the system. Large surfaces and particles submerged in the presence of small depletants thus have a depletion exclusion zone around them, which depletant particles cannot penetrate. When the depletion exclusion zones of two particles overlap, an osmotic pressure difference

pushes the two particle surfaces together. The osmotic pressure difference is due to a difference between the concentration of depletants in bulk and in the gap between the particles. When two particles come together, the depletant particles gain free volume equal to the overlap of the two particles' exclusion zones, $\Delta V_{overlap}$, enabling them to explore more spatial configurations and increase their entropy. Therefore, an increase in the free volume of the depletant particles leads to a decrease in the overall free energy of the system. The larger the overlap between depletion exclusion zones, the stronger the depletion interaction between the two surfaces. For spherical particles, the depletion interaction between two particles is isotropic. The interaction between two particles can be made anisotropic and selective by altering the volume of the overlap between exclusion zones[7,22-24], thereby inducing a preferred relative particle orientation.

Lock colloids as first synthesized by Sacanna et al[7,8] are anisotropic building blocks with a region of concave curvature -- a dimple -- on their surface. The shape of this dimple is akin to the shape formed when a spherical shell buckles under a point load[25]. When immersed in a solution of non-ionic depleting polymer, shape-complementary lock and key colloids assemble into dumbbells. Lock and key colloids may bind to each other in two ways: they may form a nonspecific bond, where the key particle binds to the convex (spherical) surface of the lock particle, or they may form specific bonds, where the key particle binds to the concave dimple on the lock surface[26]. Specific bond formation is promoted over nonspecific bond formation if there is a greater loss in free energy when keys bind into the lock

dimple versus onto its remaining surface. The specific bond between lock and key particles is a freely rotating bond whose free energy depends on the magnitude of the depletion overlap volume between the key and the lock dimple. The depletion overlap volume depends on the degree of shape complementarity between the key and lock dimple surfaces. The freely rotating lock-key bonds enable lock-key colloidal molecules to be mechanically reconfigurable[27,28]. Shape complementarity between the key and lock dimple surfaces refers to the degree of geometric (curvature) matching of the convex and concave particle surfaces so as to facilitate docking of one particle onto the other's surface.

Although depletant particles gain free volume when a lock and key bond is formed, the key particles that bind to the lock dimple lose configurational entropy, because the volume their centers of mass can explore is reduced to a small binding volume. Thus, for specific lock-key bonds to be stable and to increase the formation number of lock-key dumbbells, the increase in binding (internal) energy experienced by the key when it binds at the dimple has to be sufficiently large to account for the loss in the key particle's configurational entropy.

In previous work, we performed experiments and modeling to probe the kinetic pathways of lock-key colloidal assembly[26]. We found that specific lock-key bonds are formed via two binding routes: one direct route where key particles diffusing in bulk bind to the lock cavity, and another indirect route where key particles diffuse on the surface of the lock until they encounter and bind to the lock dimple. Modeling and simulation that considered the interaction between the

concave and convex surfaces of the interacting particles predicted more favorable formation of specific bonds over nonspecific bonds for key particles that are slightly smaller in size than the dimple cavity[19].

Previous experimental work on the equilibrium self-assembly of lock-key colloids suggested that more lock-key specific bonds are formed when the depletion overlap volume between key and dimple is maximized[7], which occurs when the spherical key particles matches the dimple cavity shape. In that work, because the topographical feature sizes (dimple and key radii) exceed the depletant size and Debye screening length, the electrostatic and depletion interaction between key particles and the lock dimple were modeled as occurring between flat plates with an effective area of interaction. No explicit characterization of the lock surface topography was reported, and the effective area between key and lock dimple was reported as a fitting parameter. Existing literature on the rational design of ligand-protein binding, on the other hand, suggests that tight fits between protein and ligand are unfavorable due to their high entropic cost[29,30]. Results from previous simulation work that included full determination of the depletion and electrostatic interaction potentials from considering of the dimple topography imply the same principle applies to the formation of lock and key colloidal molecules.

In this work, we perform experiments to investigate the effect of shape complementarity on the binding free energy and formation of lock-key dumbbells. We change the magnitude of the overlap volume by matching one lock particle to five different key particles of sizes smaller and larger than the lock dimple cavity

radius. We characterize the lock particles using atomic force microscopy (AFM), and, using topographic information extracted with AFM and the size of the key particles used, we characterize the ratio of the key size to lock cavity size. We perform measurements of fractional occupation for each of the different size ratios and for different depletant concentrations; these fractional occupancies are converted to free energies of formation by choice of a suitable reference state. We find that key particles smaller than the average dimple cavity size have more favorable free energies of specific lock-key bond formation than keys whose size is larger than the size of the dimple. That is, the free energy of formation is asymmetric about a condition at which the lock dimple curvature matches the key curvature, with key curvature smaller than pocket curvature being more favorable. Our results are in agreement with previous modeling and simulation work[19] that predicts optimized binding and formation of specific lock-key bonds for spherical key particles smaller than the lock cavity radius, which also exhibits a similar asymmetry about matched particle curvatures. In addition, results at high polymer concentrations suggest that the depletion attractive is moderated at these conditions, and that the free energy of formation in this case is not as favorable as would be predicted by the Asakura-Oosawa depletion interaction.

Theory

The law of mass action, and equilibrium thermodynamics

In our experiments, the colloidal suspensions reach equilibrium at constant volume and temperature conditions. Thus, the Helmholtz free energy of the system, F, where $F = U - TS$, U is the internal energy of the system, S is its entropy, and T is the absolute temperature, is minimized. From considering thermodynamic equilibrium for the reaction L + K ←→ LK, and assuming we have an ideal, dilute gas of particles, the equilibrium constant, K_{eq} , is given by

$$K_{eq} = \frac{\chi_{LK}}{\chi_L \chi_K} = \frac{n_{LK} n_{total}}{n_L n_K} = \frac{N_{LK} N_{total}}{N_L N_K}, \quad (1)$$

where n_i is the number density of species i, N_i is the number of particles of free species i, χ_i is the ratio of partial fractions of dilute gaseous species i, $\chi_i = n_i/n_{total}$, n_{total} is the sum of the number densities of all species, and the total number of particles is given by $N_{total} = N_L + N_K + N_{LK}$ [31] (Since the volume in our experiments is constant, we record particle numbers instead of number densities.) The free energy of formation of lock-key bonds, ΔF^o, is then given by

$$\beta \Delta F^o = -\ln(K_{eq}) = -\ln \frac{N_{LK} N_{total}}{N_L N_K}, \quad (2)$$

where $\beta = (k_B T)^{-1}$, k_B is Boltzmann's constant, and T is temperature.

We measure the free energy of formation of lock-key bonds, ΔF^o, by measuring the equilibrium constant, K_{eq}, which we do by counting the number of free locks, free keys, and occupied available locks in fixed volume regions identified by the field of view of a microscope, as outlined below. We do not include the

number of locks occupied by another lock, N_{LL}, in the total number of locks counted, to yield the count of free, unbound locks that are available to bind to keys, N_L; the number of locks occupied by other locks is small relative to the total number of other particle species (see below). Errors in the number measurements are calculated by propagating errors in counting of particle species. To compare experimental results to previously published simulation results, we plot ΔF^o against nonspecific binding energy.

In previous work, we measured the free energy of formation of nonspecific bonds (free to nonspecific binding), as well as the free energy difference between nonspecific and specific binding. In that work, we measured the equilibrium constant for free to nonspecific binding by applying detailed balance[26]. In this case, the equilibrium constant was a ratio of rate constants and the reference concentration (standard state) was taken as the reciprocal of the volume of the nonspecific state. In this work, we calculate equilibrium constants using particle numbers, based on treating the particles like dilute particle species. Thus, the reference concentration is given by the total particle concentration, as outlined above. The use of different reference concentrations has the effect of shifting the free energy curves by a factor equal to the natural logarithm of the ratio of the reference concentrations.

Specifically, the reference concentration used in our previous work[26] was the reciprocal of the volume of the nonspecific binding state, $n_o = 0.039\ \mu m^{-3}$. In our current experiments, since we treat the species as dilute gases, the reference

concentration is given by the total number density of particles. This concentration is made by a direct count the number of particles; for the experiments reported here, the total number density of particles in an experiment varies in the range 10^{-3} – 10^{-4} μm^{-3}. This implies that, had we chosen the same reference concentration as in our previous work, the free energies in this work would be shifted up by 3.6 k_BT – 6 k_BT, given by the ratio of reference concentrations. We compare the free energy of specific bond formation at 1.5 mM NaCl and 0.8 g/L extracted in past work[26] to the free energy of specific bond formation at those conditions from the experiments presented in this paper (1.5 mM, 0.8 g/L, δ = 1.1). From Figure 2.9 in Chapter 2 and, using $\Delta F^0 = \Delta F_{F-NS} + \Delta F_{NS-S}$, we find $\Delta F^0 = 1.7\ k_BT$ in our previous work for a shift up of ~1.5 k_BT for values reported here at the same condition. Experimental errors discussed in the previous chapter could potentially explain this deviation.

Nonspecific pair potential energy calculation

We plot the fractional occupation of locks θ_{LK} and the free energy of lock-key bond formation ΔF^o versus the non-specific binding energy E_b. The nonspecific binding energy E_b is defined as the absolute value of the minimum of the total nonspecific interaction potential, which is given by the sum of the contributions by the depletion interaction and the electrostatic interaction between two spheres. We do not include van der Waals interactions because we use Pluronic F108 in our system as a steric stabilizer, which keeps the particles separated by distances at which attractive van der Waals forces are small. We use the Asakura-Oosawa

model[32] for the depletion interaction, and the Yukawa screened electrostatic interaction potential for the electrostatic interaction, namely, $\Phi = \Phi^{AO}_{depletion} + \Phi_{electrostatics}$. The depletion interaction potential, $\Phi^{AO}_{depletion}$, is given by $\Phi^{AO}_{depletion} = -\Pi_{polymer}\,\Delta V_{overlap}$, where $\Pi_{polymer}$ is the osmotic pressure of the depletant polymer particles, and $\Delta V_{overlap}$ is the volume of the overlap of the exclusion zones of two spherical surfaces. For our simple estimate, we assume that polymers are ideal, such that $\Pi_{polymer} = \beta^{-1} n_{polymer}$, where $\beta^{-1} = k_B T$, $n_{polymer}$ is the number density of polymer molecules, k_B is Boltzmann's constant, and T is absolute temperature. Thus, the strength of the depletion interaction increases with increasing polymer concentration. The electrostatic interaction potential, $\Phi_{electrostatics}$ is given by the screened electrostatic repulsion potential between two unequally sized charged spheres[33].

Our estimate of nonspecific binding energy assumes that the depleting polymer molecules do not interact with each other, resulting in a depletion-induced attraction that is purely entropic in origin. Experiments and theories describing the depletion interaction suggest that a complete description of the depletion interaction mediated by non-ionic macromolecules like polyethylene oxide must consider the effects of polymer polydispersity[34], non-ideal solution osmotic pressure[35], as well as effects arising from structure formation of the small depletant chains[36,37] that result in the presence of oscillatory depletion interaction potentials. These structure effects might have a stabilizing effect on particle suspensions,

especially at high polymer concentrations[38].

Materials and Methods

Lock and key particle characterization

In this study we used one size lock particle and five different sized key particles (see Table 3.1). Lock particles were made with 3-trimethoxysilylpropyl methacrylate (TPM) and synthesized following Sacanna et al[7,26]. A key particle made of TPM was synthesized as described elsewhere[26]. Polystyrene beads used as keys were obtained from Polysciences (1.75 μm) and Life Technologies (1.0 μm, 1.4 μm, 1.9 μm). Average values of the particle zeta potentials, measured using a Malvern ZetaSizer, are reported on Table 1 (N = 5 measurements). For more details on key particle characteristics, see Table 3.1.

We used an atomic force microscope (Veeco Dimension Icon, equipped with a Bruker SCANASYST-AIR probe tip) to image the lock particles and obtain information about surface concavity of the lock particles (see Fig 3.1a – 3.1c). We obtain line height profile information from the AFM images with Gwyddion open-source software. As can be seen on Figures 3.1a and 3.1b, three regions of different curvatures characterize the lock particle surface: the lock dimple, the lock lip, and the rest of the lock's spherical surface. Using Matlab, we perform a fit to each height profile data and average the different fit results to obtain the mean radius of curvature of the dimple, R_{dimple} = 0.965 ± 0.167 μm (N = 15 different measurements; standard error of the mean $\sigma/\sqrt{N}$ = 0.043 μm) (Fig. 3.1c). Note that the lock

particles have a polydisperse dimple; the radius of curvature of the dimple has a coefficient of variation (CV) equal to 17.3%. We calculate δ, the key-to-dimple size ratio, $\delta = R_{key}/R_{dimple}$, for all key particles used (see Table 3.1 and Fig. 3.1d), using average values and error propagation.

Sample preparation

Stock solutions of 1.0 mM, 1.5 mM, and 2.0 mM NaCl were prepared, as well as stock solutions of 2 g/L polyethylene oxide (PEO, viscosity average molecular weight M_v = 600,000 g/mol, R_g = 50.2 nm [39], critical overlap concentration c* = 1.88 g/L; Sigma-Aldrich) at 1.0 mM, 1.5 mM and 2.0 mM NaCl. Dilute lock and key colloid suspensions of 2 mL volume (lock volume fraction $\phi = 9.5 \times 10^{-5}$; key volume fractions $\phi = 1.6 \times 10^{-4} - 2.7 \times 10^{-4}$; see table 3.1) were prepared by adding corresponding amounts of 1.0 mM, 1.5 mM, or 2.0 mM NaCl solution, PEO solution, 25 µL of a 1 wt% tetramethylammonium hydroxide (TMAH, Sigma Aldrich) solution in water, and 25 µL of a 5 wt% Pluronic F108 (Sigma Aldrich) aqueous solution. For each different salt condition, we varied [PEO] from 0.4 g/L to 1.2 g/L in 0.2 g/L increments. This range corresponds to c/c* varying from c/c* = 0.21 to 0.64.

After we prepared the samples, we dipped a rectangular capillary tube (Vitrocom, #5012-050; inner capillary height h =100 µm) into the suspension until it was completely filled and devoid of air bubbles. After the capillaries were filled with the prepared suspensions, they were glued to a glass slide using UV light-curable glue (Dymax® GR217-A). The slides were then taped onto the inner surface

of a 10 cm inner diameter PVC tube. The tube was placed on a mechanical roller (rotation rate = 9 rpm) for three days[40].

Confocal imaging and particle counting

After a given sample rotated for 3 days, it was removed and its assemblies and particles allowed to sediment for at least 10 minutes before imaging at the bottom surface of the capillary. Lock particles (density $\rho = 1.24$ g/cm^3), have a sedimentation velocity of 0.75 μm/s. Therefore, by 10 minutes, we expect that lock particles and lock-key colloidal molecules will have sedimented to the bottom of the capillary. Key particles may only have partially sedimented, and this point is addressed below. Samples were imaged using a Nikon A1.R confocal microscope equipped with a 100x oil-immersion, NA = 1.45 oil immersion objective, and imaged at 10 different regions for a total of 6.67 seconds (fifty frames at 7.5 fps per region, or one hundred frames at 15 fps, depending on the number of fluorescent channels) to ensure proper identification of lock-key dumbbells. (The potential effect of possible misidentification of specifically bound lock-key complexes is discussed below.) When possible, fluorescence imaging was performed to distinguish between particle species ($\lambda_{ex} = 488$ nm, $\lambda_{ex} = 561$ nm; see Table 3.1 and Fig. 3.2). Differential interference contrast (DIC) transmission images were acquired to identify the lock particle dimple and count potential false positives. The image acquisition size was $A = (512 \text{ pixels})^2 = (127.45 \text{ μm})^2$, where 1 pixel = 0.249 μm. Representative images

of a lock-and-key suspension used for particle identification are shown in Figures 3.2 and 3.3.

To measure the number of different free particle species i, N_i, we manually count the number of free keys N_K, all free available locks N_L, and the number of locks occupied by key particles N_{LK} within the image area. Since the abundance of trimer and tetramer colloidal molecules was low relative to the formation of dumbbell colloidal molecules (one lock bound specifically bound to one key), we include these locks and keys in the count of N_{LK} and N_K, respectively. To count the number of free available (unbound) locks N_L, we discount the number of locks occupied by other locks, N_{LL}. The percentage of locks occupied by other locks increases with depletant concentration and does not exceed 10% even at the largest polymer concentrations.

We used three different methods to count key particles. To measure the number of polystyrene key particles, we calculated the number of particles present in the image area by multiplying the particle volume fraction (see table 3.1) by the volume of the column of liquid above the image acquisition area, equal to V = A h, where h is the capillary height (h = 100 μm) and A is the image acquisition area (A = (127.45 μm)^2). Measurements of particle numbers using a hemocytomer (INCYTO™ C-Chip™) were in agreement with these calculations. Finally, we counted TPM keys with the same method as the TPM locks, since both particles fully sediment to the substrate by the 10 minute observation time.

Fractional occupation

We measure the fractional occupation of locks by key particles, as well as the free energy of formation of lock-key bonds for all five different lock-key particle concentrations at different [PEO] and NaCl concentrations, after the system has reached equilibrium. To measure the fractional occupation of locks by key particles for a given experimental condition, θ_{LK}, we divide the number of locks occupied by keys N_{LK} by the total number of locks that were available to bind with keys, $N_L + N_{LK}$, $\theta_{LK} = \frac{N_{LK}}{N_L + N_{LK}}$. Errors in fractional occupation arise due to errors in counting of the different particle species.

Results and Discussion

In Figure 3.2, we show representative images of two different lock-key combinations at different depletant polymer concentrations and constant salt concentration. Figures 3.2a and 3.2b show 1.4 μm polystyrene keys in 1.0 mM NaCl solution in the presence of 0.6 g/L and 1.2 g/L of PEO, respectively. Figures 3.2c and 3.2d show 1.9 μm polystyrene keys at the same respective conditions. As can be seen, for both cases the number of available lock particles occupied by key particles increases as [PEO] increases. The fractional occupation, θ_{LK}, of locks with 1.4 μm keys is larger than that for 1.9 μm keys at both conditions: a larger fraction of lock particles are occupied by keys when using 1.4 μm PS keys than 1.9 μm PS keys.

As discussed in previous work[19], it is possible to misidentify the number of specifically bound keys by conflating them with nonspecifically bound lock-key complexes which are not in the object plane. When counting the number of lock-key dumbbells, we keep track of the number of specifically bound lock-and-keys that could potentially have been misidentified (false positives) by keeping count of lock-key pairs where one of the particles is out of the focal plane. On Fig 3.3, we show the fluorescent and DIC imaging channels of one frame of a 1.5 mM NaCl, 0.8 g/L PEO lock-key suspension for $\delta = 0.9$. On Fig. 3.3a, we show the composite image of two-fluorescence channels, and on Fig. 3.3b we show the DIC transmission image of the same frame. All specific bonds between locks and keys are circled on Fig. 3.3a. The dashed-lined circle shown in Fig. 3.3a and 3.3b represents a possibly misidentified lock-key complex. We use DIC transmission images to assess whether identified

lock-key complexes can be considered false positives, by considering whether the lock dimples are visible and whether key particles are out of plane, which can be determined by its appearance, as keys in plane look darker than those out of plane. As can be seen on Fig. 3.3b, the key particle in this case is out of plane, and it is uncertain whether the key is inside the dimple or nonspecficially bound to the spherical surface of the lock particle.

Figures 3.4a and 3.4b show plots which establish bounds on the effect of false positives on fractional occupation measurements and free energy measurements for $\delta = 0.9$ at 1.0 mM NaCl. In these figures, "criterion 1" refers to considering all lock-key complexes; "criterion 2" refers to considering all lock-key complexes except possible false positives. Consideration of possible false positives causes the fractional occupation curve to shift down by an average of 15% and the free energy of formation curve to shift up in value an average of 0.4 k_BT for any given [PEO]. These error bounds are much less than the effect of depletant concentration, as evidenced by the equivalent trend and shape of the curve.

In Figure 3.5, we plot the effect that salt concentration on the fractional occupation of available locks for the particular case of a key-to-dimple ratio $\delta = 0.9$. For [PEO] below 1.0 g/L, corresponding to c/c* below 0.53, fractional occupations increase with increasing [PEO], as expected[7]. As salt concentration goes up, the fractional occupation of available locks is expected to increase because of the increased screening of repulsive charge between the lock and key pair. At 1.0 mM NaCl, fractional occupation values increase with [PEO], reaching more than 80%

available lock occupation at [PEO] = 1.2 g/L. For 1.5 mM and 2.0 mM NaCl, fractional occupation values saturate after [PEO] = 0.8 g/L to approximately 60% occupied available locks for 1.5 mM NaCl, and approximately 75% for 2.0 mM NaCl. A small number of multiparticle clusters were observed at [PEO] greater than 0.8 g/L for 1.5 mM and 2.0 mM NaCl conditions. Moreover, at 2.0 mM NaCl and 1.2 g/L, clustering of locks and keys prevented measurement of the number of bound lock-key complexes.

The fractional occupancy of locks is a strong function of the relative size of the key and dimple. In Fig. 3.6a, we plot the fractional occupation (θ_{LK}) as a function of nonspecific binding energy βE_{NS} for all five different key-to-dimple size ratios δ and [PEO] probed for the particular case of 1.5 mM NaCl (See Figure 3.9a and 3.9b for [NaCl] = 1.0 mM and 2.0 mM data). Data for all five different δ indicate an increase in fractional occupation number with increasing nonspecific binding energy. For δ smaller than or equal to 0.9, we observe that maximum θ_{LK} exceeds 0.5 for nonspecific binding energies below k_BT. That is, the enhanced depletion generated by the concave shape of the dimple generates strong binding when the convex binding interaction is still well below the thermal energy.

Suspensions with δ = 0.5, corresponding to 1.0 μm keys, yield θ_{LK} below 0.11 for all nonspecific binding energies probed except for $E_{NS} = 0.9\ k_BT$, which yields $\theta_{LK} = 0.68$. Lock-key particle suspensions with δ = 0.7 and δ = 0.9, corresponding to key particles with size 1.4 μm and 1.75 μm respectively, are the most effective binders, showing increasing fractional occupation of available locks with increasing

nonspecific binding energy, and achieving the largest values of fractional occupation of all five different δ. For δ = 0.7, the largest fractional occupation value observed was $\theta_{LK} = 0.83$ for $\beta E_{NS} = 0.81$. For δ = 0.9, $\theta_{LK} = 0.64$ was measured at $\beta E_{NS} = 0.78$. Lock-key particle suspensions with δ = 1.0, corresponding to a key size of 1.9 μm, show an increase in fractional occupation number from $\theta_{LK} = 0.012$ for $\beta E_{NS} = 0.45$ to approximately 21% for $\beta E_{NS} = 1.2$. For δ = 1.1, fractional occupation of $\theta_{LK} = 0.55$ is achieved when $\beta E_{NS} = 1.74$. Lock-key binding for δ = 1.0 is the least favored of all size ratios, with fractional occupations equal to or below $\theta_{LK} = 0.21$ for all nonspecific binding energies probed. Figure 3.6a therefore shows a complex dependence of binding on both the nonspecific binding energy and the pocket to key ratio.

Figure 3.6b plots the free energy of formation of specific lock-key bonds, ΔF^o, versus nonspecific binding energy for all five different δ at 1.5 mM NaCl (See Figure 3.10a and 3.10b for [NaCl] = 1.0 mM and 2.0 mM data), using equations (1) and (2) to calculate free energies from measured particle numbers. In this plot, positive free energies ($K_{eq} > 1$) indicate that specific lock-key bond formation is not favored, whereas negative free energies ($K_{eq} < 1$) indicate specific lock-key pair formation is favored. Consistent with the fractional occupation data, key-to-dimple size ratios of δ = 0.7 and δ = 0.9 show the most favorable binding free energies. For these two size ratios, the free energy becomes negative at nonspecific binding energies that are lower than those of the other size ratios. For δ = 0.7, the free energy of formation of lock-key bonds decreases from $\beta\Delta F^o = 0.13$ to -1.84 as the nonspecific binding

energy increases from βE_{NS} = 0.52 to βE_{NS} =0.81. For δ = 0.9, $\beta \Delta F^o$ changes from $\beta \Delta F^o$ = 1.04 for βE_{NS} = 0.25 to $\beta \Delta F^o$ = -0.63 for βE_{NS} =0.49. The decrease in the free energies of specific bond formation for δ = 0.7 and δ = 0.9 correspond to more than doubling of their fractional occupation values, seen in Figure 3.6a. For the smallest key-to-dimple size ratio, specific binding is not favored until E_{NS} = 0.9 k_BT, when the free energy of specific bond formation becomes negative, and the fractional occupation has a sharp increase to $\theta_{LK} = 0.68$ from its previous value at E_{NS} = 0.7 k_BT, $\theta_{LK} = 0.11$.

For δ = 1.0, crossover from a positive to negative free energy of formation is absent. Instead, we observe that the free energy of specific bond formation is positive and plateaus at ~1.5 k_BT, implying that specific bond formation is not favored even as nonspecific binding energies increase. In suspensions with δ = 1.1, specific bond formation is favored over unbound particle species for nonspecific binding energies greater than 1.2 k_BT. Correspondingly, fractional occupation values at these conditions remain low. Figure 3.6b shows that the free energy of formation of specific lock-key bonds is sensitive to the key to pocket ratio, and that specific bond formation is more readily favored for key to dimple ratios below one.

In previous modeling and simulation work[19],the free energy difference between nonspecific and specific binding was determined as a function of nonspecific binding energy for different key-to-dimple size ratios. In that work, nonspecific binding energies were obtained by assuming the Asakura-Oosawa form for the depletion interaction. Overlap volumes $\Delta V_{overlap}$were calculated taking into

consideration dimple topography extracted from TEM images. Plots of the free energy difference between nonspecific and specific binding versus nonspecific binding energy were concave downward for all key-to-dimple size ratios probed. In our experiments, we observe saturation of the fractional occupation numbers as well as the free energy of formation of specific bonds (Figures 3.5 and 3.6) at [PEO] greater than 0.8 g/L, which corresponds to $c/c^* = 0.42$. The plots of free energy of specific bond formation plotted against nonspecific energy exhibit changes in their concavity as the key to dimple size ratio and the depletant concentration is increased. Thus, the simulations and experiments show differences, especially at high depletant concentration and high key to dimple ratios. We explore possible explanation for this deviation observed at higher depletant concentrations below.

In Figures 3.7a and 3.7b, we show two specific lock-key bonds with key-to-dimple size ratio $\delta = 1.1$ formed at 1.5 mM NaCl and [PEO] = 1.0 g/L which break. Modeling work that took into consideration the anisotropy of the interaction potential between the particles[19] suggested that at this depleting polymer concentration and salt concentration, unbinding events from the specifically bound lock-key configuration would be rare, and that the free energy difference between the nonspecific binding configuration and specific binding configuration favored the formation of specific bonds. This work predicted that specific lock-key bonds would break at a rate below 10^{-3} s^{-1} (specific to nonspecific unbinding rate coefficient, see ref. [19]). The images shown in Figures 3.7a and 3.7b show that specific binding events break more readily than predicted by theory, signifying that specific lock-key

binding at this condition is not as favored as theoretically expected. The specific bonds shown in these images break in about 50 seconds. In Figure 3.7c, we show several specific bonds formed between locks and keys with key-to-dimple size ratio $\delta = 0.9$ at 1.0 mM NaCl and [PEO] = 1.0 g/L (See Figure 3.10a for the free energy of specific bonds at this salt condition). No unbinding events were observed over a time period of 10 minutes. Differences between theory and experiments regarding the behavior of free energy of specific bond formation plotted against nonspecific binding energy suggest further exploration of the depletion interaction, in particular deviations from ideal depletant osmotic pressure.

When calculating nonspecific binding energies for the abscissa scale in Figures 3.5 and 3.6, we assume the Asakura-Oosawa form of the depletion interaction. This assumes that depleting particles behave like penetrable hard-spheres that do not interact with each other and form no structure. In previous work, we measured the nonspecific binding energy between particles using the lifetime of nonspecific lock-key to unbound events, and found that our values deviated from Asakura-Oosawa model expectations[26]. The results presented on Figures 3.5 and 3.6, which are plotted against nonspecific binding energy, might change if the nonspecific binding energy is actually measured. Based on the results of ref [28], the AO potential is a good estimate of potential in these systems for depletant polymer concentrations below 0.8 g/L ($c/c^* = 0.42$), but overestimates the potential at higher polymer concentrations.

The non-ideal behavior of non-ionic polymer depletant solutions has been studied by direct measurement of the depletion interaction potential between large particles and surfaces mediated by polyethylene oxide macromolecules[41,42]. Edwards et al. used total internal reflection microscopy (TIRM) to measure the depletion potential between particles and a glass surface for polymer concentrations below $c/c^* = 0.3$. Experimentally measured potentials were suitably fitted by modifying the equation of state of the polymer using renormalization group theory, which yields smaller predicted binding energies than the Asakura-Oosawa model, and a depletion layer thickness that decreases with increasing polymer concentration, which effects the range of the interaction potential[41]. Bechinger et al. used TIRM to measure the depletion interaction potential between a particle and a glass surface in an aqueous suspension with PEO, and found that their measured potentials could be explained by considering an inhomogeneous distribution of PEO near surfaces. This inhomogeneous distribution of PEO arises due to short-ranged electrostatic repulsion at small distances and dispersion attraction between the PEO coils and the glass surface. In their work, they report the presence of a small repulsive barrier in the depletion interaction at depletant concentrations below $c/c^* = 0.03$ [42].

In addition to this, at high depleting particle volume fractions, depletion interactions may have a stabilizing effect, arising from the formation of structure that occurs as depleting particles interact with each other, which lead to oscillatory interaction potentials with an energy barrier and secondary minima[37,38]. Energy

barriers and structural oscillations in the potential of interaction of the particles could explain the plateaus we observe in fractional occupation and free energies of formation, since less particles would reach the global internal energy minimum as they may be stable in secondary minima or unable to pass energy barriers without external energy input. Direct measurement of the potential of interaction using techniques such as optical tweezers or total internal reflection microscopy would clarify what effect, if any, structural forces or enthalpic effects arising from interactions between the PEO depletant particles have on the assembly of lock-key colloids.

Note that for all but one of the five different key-to-dimple size ratios at 1.5 mM NaCl, the plots of free energy of formation exhibit a crossover from positive to negative binding free energies as nonspecific binding energy increases. To better investigate the effect of key-to-dimple size ratio, we define the crossover nonspecific binding energy $\beta E_{NS}^{crossover}$ as the nonspecific binding energy where free energy of formation is equal to zero. (The crossover is determined by interpolation between a positive and negative binding free energy. That is, we measure the value of $\beta E_{NS}^{crossover}$ by interpolating between the points immediately above and below the nonspecific binding energy axis for each free energy curve on Fig. 3.6b.) Errors in $\beta E_{NS}^{crossover}$ are obtained by interpolating between the upper and lower errors of the points immediately above and below the nonspecific binding energy axis. We do not estimate a crossover nonspecific binding energy for key-to-dimple size ratios whose free energy of formations remain positive.

To quantify the effect of key-to-dimple size ratio on the formation of specific lock-key bonds, we plot the crossover nonspecific binding energy $\beta E_{NS}^{crossover}$ against key-to-dimple size ratio, δ, as shown in Fig. 3.8, for the [NaCl] = 1.5 mM data presented on Fig 3.5b and the 1.0 mM and 2.0 mM data presented on Figures 3.10a and 3.10b, respectively. For $\delta \leq 0.9$ and [NaCl] = 1.5 mM, the crossover nonspecific binding energies are smaller than k_BT. The results imply that for these size ratios, the specific binding energy is much larger than k_BT, so as to drive the key into the pocket even given the entropic penalty associated with localization in the bond.

The nonspecific interaction potentials at [NaCl] = 1.0 mM were positive for all key sizes except 2.1 μm, which precludes us from plotting crossover nonspecific binding energies at this salt condition except for $\delta = 1.1$. (See Figure 3.10a). Crossover nonspecific binding energies for [NaCl] = 1.0 mM and 2.0 mM are plotted along with those for 1.5 mM on Figure 3.8. At this higher salt concentration, we observe that keys with size ratio below one have lower crossover nonspecific binding energies than those with size ratio greater than one, but that the values of the crossover nonspecific binding energies are above k_BT. The increase in crossover nonspecific binding energies is explained by the increased salt concentration, which results in stronger nonspecific binding at equal [PEO] due to increased screening of the particles' double layers.

The value of the crossover nonspecific binding energy at 1.5 mM is smallest for $\delta = 0.9$, for a value of $\beta E_{NS}^{crossover} = 0.39 \pm 0.01$, closely followed by $\delta = 0.7$ with $\beta E_{NS}^{crossover} = 0.54 \pm 0.02$. For $\delta = 1.0$, corresponding to a perfect match between key

and dimple, the crossover nonspecific binding energy value has more than tripled its value at $\delta = 0.9$ to $\beta E_{NS}^{crossover} = 1.4 \pm 0.13$. The data on Figure 3.8 suggest that specific lock-key binding is preferred over unbound locks and keys at lower nonspecific binding energies for suspensions where the key-to-dimple size ratio is below that of a perfect match, relative to above a perfect match.

Figure 3.8 supports the claim that smaller key sizes form lock-key bonds more readily than larger key sizes. That is, if a key does not match the lock pocket, then a smaller, mismatched key still allows for better specific binding than a larger mismatched key. There is an asymmetry in how well the lock key bond respond to geometric mismatch. This result is consistent with previously obtained simulation results for the free energy difference between nonspecific and specifically bound lock-and-key pairs.

To explore the cause of the observed asymmetry, we consider the effect of geometric mismatch on both the energetic and entropic contributions to the free energy for the case of mismatch due to a relatively small key, or a relatively large key. In previous work[19], the depletion overlap volume and the repulsive electrostatic interaction were determined as a function of distance between lock and key particles and the angle between the line connecting the centers of the particles and the orientation vector of the lock dimple for the $\delta = 1.1$ case. Changes in the magnitude of the overlap volume as well as the electrostatic repulsion interaction show that the internal energy of the specific bond, made up of depletion interaction

and electrostatic interaction contributions, between lock and key particles is a complicated function of the curvatures of the particles, as discussed below.

For geometric mismatch due to small keys, we expect the key's convex surface to be able to be in close proximity to the concave surface of the lock, leading to more overlap of the depletion zones surrounding these surfaces than in the case when the key to dimple size ratio is greater than one. The overlap volume in cases where the key-to-dimple size ratio is less than one is expected to decrease as the key to dimple size ratio decreases, since there is less proximity between the particle surfaces as the key curvature becomes smaller. This entails that key particles with small key-to-dimple size ratios will not bind so easily to the lock dimple as a key particle with key-to-dimple size ratio slightly smaller than one, since larger particles will interact more strongly with the lock dimple surface than small ones, since the depletion interaction is proportional to the overlap volume.

When bound to the concave surface of the lock, particles with key-to-dimple size ratio below one are free to explore different binding configurations inside the dimple, which increases the entropy of the bond. Key-to-dimple size ratios equal to one are entropically penalized, as key particles are able to access less microstates in their binding volume.

For geometric mismatch due to a large key, however, the key's convex surface and the lock's surfaces are not necessarily in close proximity, due to the changing curvature of the lock surface. As shown in Figure 3.1a-c, the lock particle surface has three distinct regions of curvature: the spherical surface of the lock, the

lock lip, and the lock dimple area. The key particle surface, in the case of key-to-dimple size ratio exceeding one, is not in close proximity to the lock dimple basin, which entails a smaller depletion overlap volume between the two surfaces. The surface of a key particle that exceeds the lock dimple size will interact with the concave (bowl-shaped) dimple area and the convex lock lip or rim, affecting the magnitude of the overlap of the depletion exclusion zones. For key-to-dimple ratios that slightly exceed one, such as the $\delta = 1.1$ case, the loss in internal energy of the specific lock-key bond is not sufficiently low to forbid the preferential formation of specific bonds, as observed in Figure 3.6. The depletion overlap volume between the particles is still large enough to allow the particles to form specific bonds, and the binding volume is sufficiently large for the key particles to be able to explore configurations within it, i.e. the bond has sufficient entropy. As the size mismatch increases, depletion overlap volumes decrease and the internal energy of the bond is not large enough to overcome particle entropy loss.

When a key particle binds onto the dimple of a lock particle, it loses configurational entropy relative to when it was freely diffusing in bulk; within the dimple, a key particle has much less volume and configurations to explore[7]. Movement of the key particle when bound to the dimple results in a slight change in the distance between the centers of mass of the lock and key particles. Allowing key particles to move and retain configurational entropy while specifically bound in the lock dimple would help minimize the free energy of the system.

For a key-to-dimple size ratio of $\delta = 0.5$, the internal energy of the specific bond is not favorable enough to overcome the overall loss in entropy of the keys, resulting in the formation of fewer specific bonds. As δ increases its value to $\delta = 0.7$ and $\delta = 0.9$, specific bonds are favored over unbound species at lower nonspecific interaction energies. For these two key-to-dimple size ratios, the internal energy of the specific bond is apparently negative enough to overcome the loss in entropy of the key particles. Moreover, key particles have enough space to assume different configurations within the dimple while remaining strongly bound to the surface.

For $\delta > 1$, the internal energy of the specific bond decreases because $\Delta V_{overlap}$ decreases when the key particle is not in full contact with the concave surface of the lock particle. Although $\Delta V_{overlap}$ is smaller, it is still large enough to promote the formation of some lock-key bonds at large enough nonspecific binding energies.

For the two best binders ($\delta = 0.7$ and $\delta = 0.9$), the data in Figure 3.8 indicate that specific bond formation is favored over unbound lock and key particles at nonspecific binding energies below or around 0.5 k_BT. This implies that a higher yield of formation of specific bonds can be expected at smaller [PEO] concentrations, which is observed in our fractional occupation curves for the two best binders, on Fig 3.6a, where fractional occupation θ_{LK} exceeds 0.5 at nonspecific binding energies below k_BT.

In previous work, we showed that low nonspecific binding energies result in short-lived nonspecific bonds[19,26]. Provided that it is not kinetically trapped, a key

particle in to a nonspecific bond can still transition into to an available lock dimple where it could lower the overall free energy of the system. The fact that $\delta = 0.7$ and $\delta=0.9$ specific bonds form readily at low nonspecific energies of interaction suggests that such conditions can be used to assemble structures[27] through the hierarchical or directed assembly of assembled lock-key dumbbells, since locks, keys, and lock-key dumbbells are not expected to aggregate into clusters[19] at nonspecific binding energies below thermal energy.

Conclusions

The work shows that in order to optimize the formation of specific lock-key bonds for a given lock particle, key particles must have radii smaller than the radius of curvature of the lock dimple. This result is commensurate with the expectation that the best binder is that which lowers the overall free energy of the system, previously predicted by simulations. Optimum binding occurs not when the binding volume between lock and key is maximized, but just barely, so that the key particle is still allowed to explore configurations within the dimple, which allows it to have translational configurational entropy, which further enables minimization of the free energy of bond formation. The formation of specific bonds is asymmetric with respect to geometric mismatch; lock-key suspensions with key-to-dimple ratios below one more readily form specific bonds than systems with key-to-dimple ratios greater than one. Key particles with a perfect match to the dimple size cannot assume many configurations inside the dimple, since they cannot move inside it. Key particles larger that the dimple size may still bind to the dimple, but the binding volume is smaller, as there is less contact between concave and convex particle surfaces, resulting in less internal energy for the bond and less formation of specific bonds.

Particle	Material	$2R_K(\mu m) \pm \sigma$	ϕ (volume fraction)	Zeta potential (mV)			$\delta = R_{key}/R_{dimple}$	Dyed
				1.0 mM	1.5 mM	2.0 mM		
Lock 1	TPM	2.38 ± 0.17	9.5×10^{-5}	-74	-80	-78	--	RBITC
Key 1	Sulfate PS	1.00 ± 0.03	2.0×10^{-4}	-86	-79	-76	0.5 ± 0.1	Yellow-Green
Key 2	Sulfate PS	1.40 ± 0.05	2.0×10^{-4}	-73	-86	-84	0.7 ± 0.1	undyed
Key 3	Carboxylated PS	1.75 ± 0.05	2.7×10^{-4}	-98	-91	-96	0.9 ± 0.2	Yellow-Green
Key 4	Carboxylated PS	1.90 ± 0.09	2.1×10^{-4}	-66	-70	-65	1.0 ± 0.2	undyed
Key 5	TPM	2.14 ± 0.09	1.6×10^{-4}	-38	-36	-42	1.1 ± 0.2	NBD-MAEM

Table 3.1 We include different particle characteristics for the lock and key particle suspensions used in our study, as well as key-to-dimple size ratios for all different binary lock-key suspensions used. RBITC refers to Rhodamine B isothiocyanate, whereas NBD-MAEM stands for 4-methylaminoethylmethacrylate-7-nitrobenzo-2-oxa-1,3-diazol.

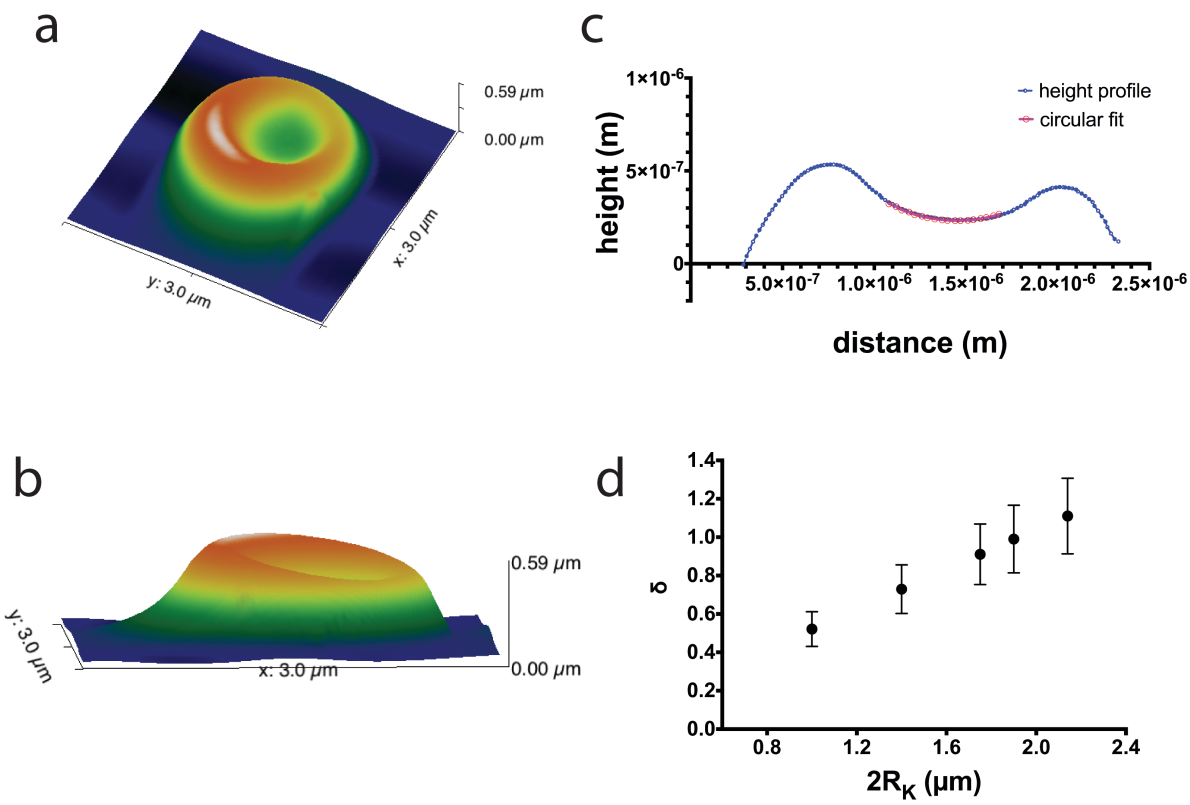

Figure 3.1 Panels (a) and (b) show atomic force microscopy images of a dimpled lock particle, presented at different views to reveal the topography of the particle. In panel (c) we show a representative height profile, obtained by performing a line scan through a different dimpled particle (blue dots), as well as showing a fit identifying the radius of curvature of the dimple (red circles and line), which we used to extract the dimple size. Panel (d) shows the key-to-dimple size ratio for all five different keys used (see Table 1).

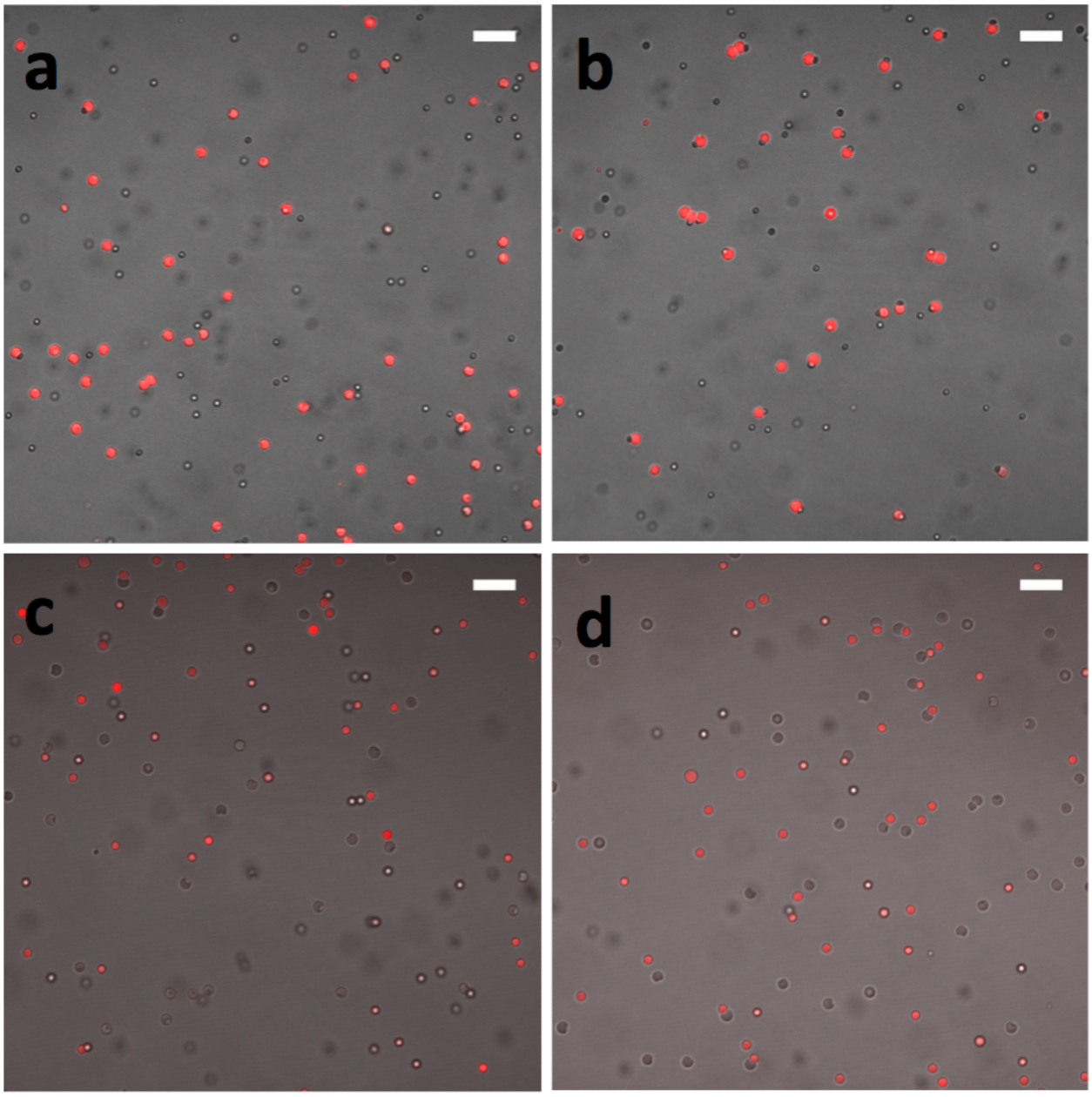

Figure 3.2 Panel (a) shows 1.4 μm key particles (undyed) in 1.0 mM NaCl and 0.6 g/L PEO. Only a few lock particles (dyed red) are occupied by keys. Panel (b) shows the same system at 1.2 g/L PEO. Most lock particles are occupied by keys or by other locks. Panel (c) shows 1.9 μm key particles (red) in 1.0 mM NaCl and 0.6 g/L PEO. Only one lock is occupied by a key particle. Panel (d) shows the same system at 1.2 g/L PEO. The fractional occupation of locks is lower than that for 1.4 μm keys at the same experimental conditions (panel b). Note that lock particles are also dyed red;

we adjusted confocal imaging parameters such that the intensity of emitted light from the locks was low relative to the keys, which fluoresced brighter.

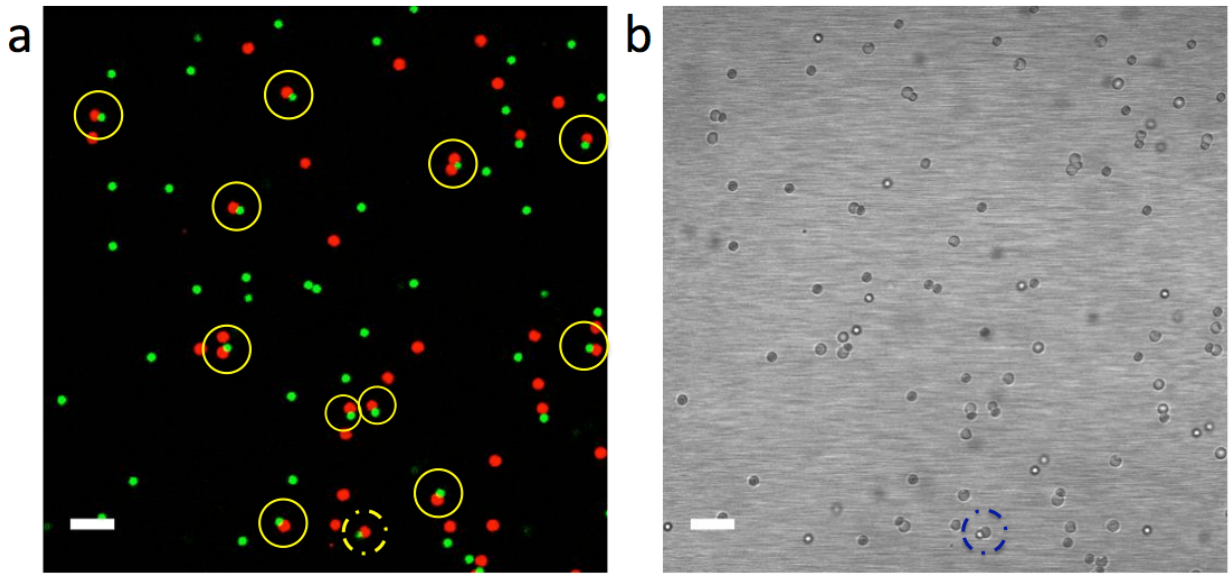

Figure 3.3 Panels show the (a) fluorescence and (b) DIC channels of one frame of a 1.5 mM NaCl, 0.8 g/L PEO, $\delta = 0.9$ suspension. Lock particles are shown in red and key particles in green. Yellow circles on panel (a) circle specific lock-key bonds. The dotted line circles on panels (a) and (b) surround a lock-key pair where the key particle is out of plane and out of focus, which could be a source of error for the counting of specific lock-key bonds. DIC images allow us to tell whether particles are out of plane since particles in plane look darker than those out of plane.

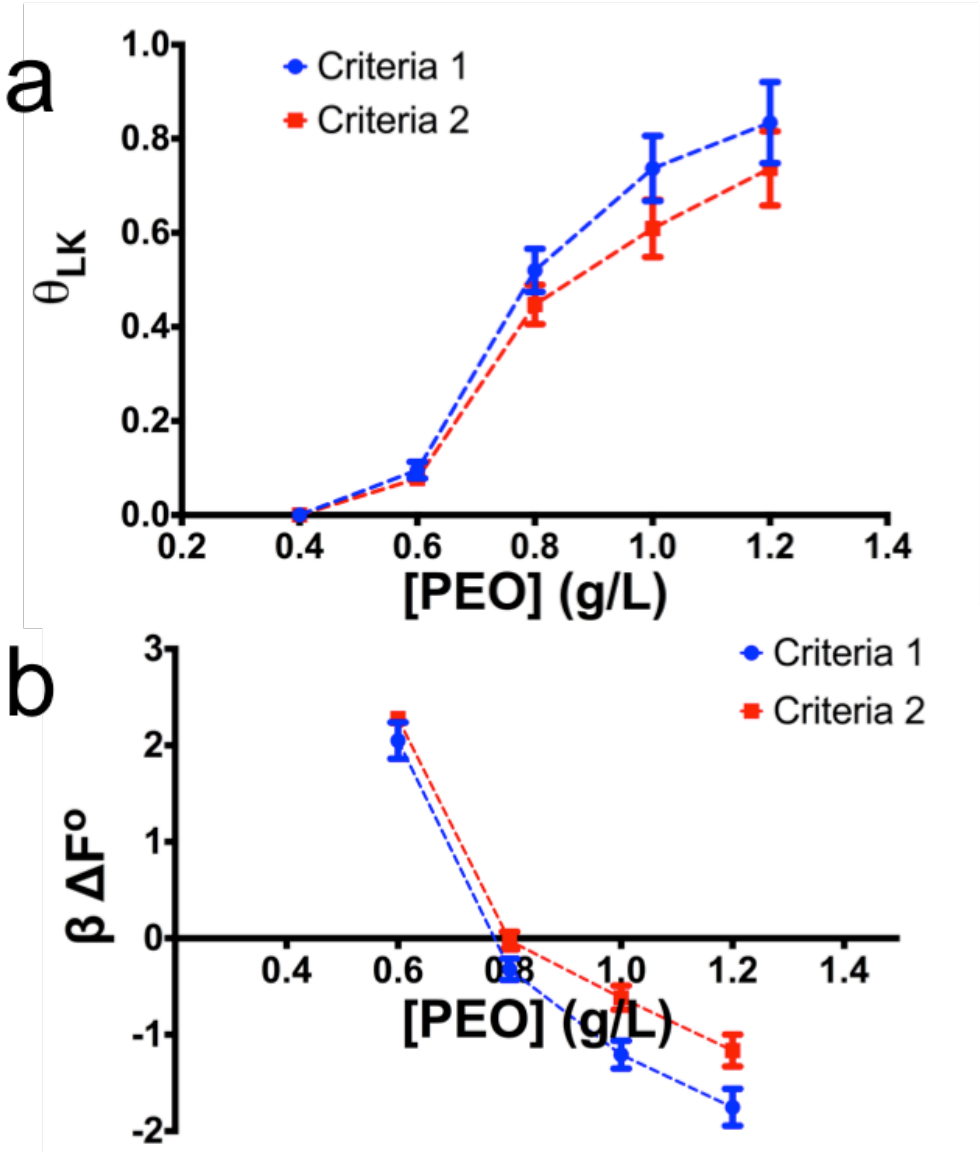

Figure 3.4 A fractional occupation plot for δ = 0.9 at 1.0 mM as a function of [PEO] is presented on panel (a), showing the effects of possible false identification of specific lock-key bonds. When we discount any lock-key pair that could conceivably be a false positive, fractional occupation numbers decrease by a modest amount, less than the replication uncertainty, which here is based on three different experiments. Panel (b) shows the free energy of formation for the same data as in panel (a). Free energies of formation increase when possible false positives are discounted from the data.

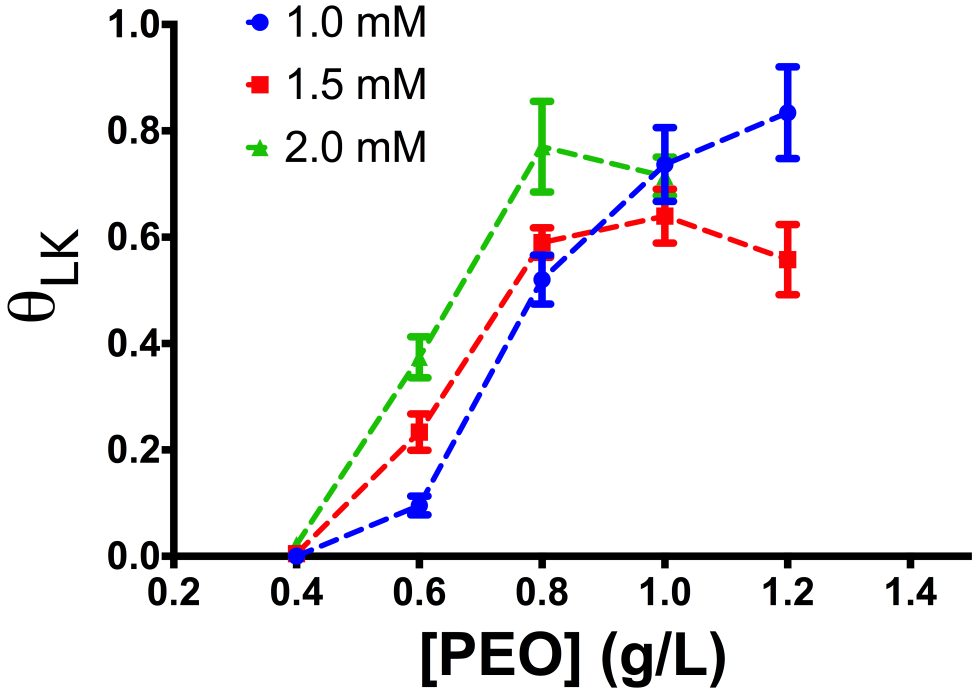

Figure 3.5 We plot the effect of salt concentration on the fractional occupation of available lock particles for $\delta = 0.9$, showing a fractional occupation increase with salt at low [PEO].

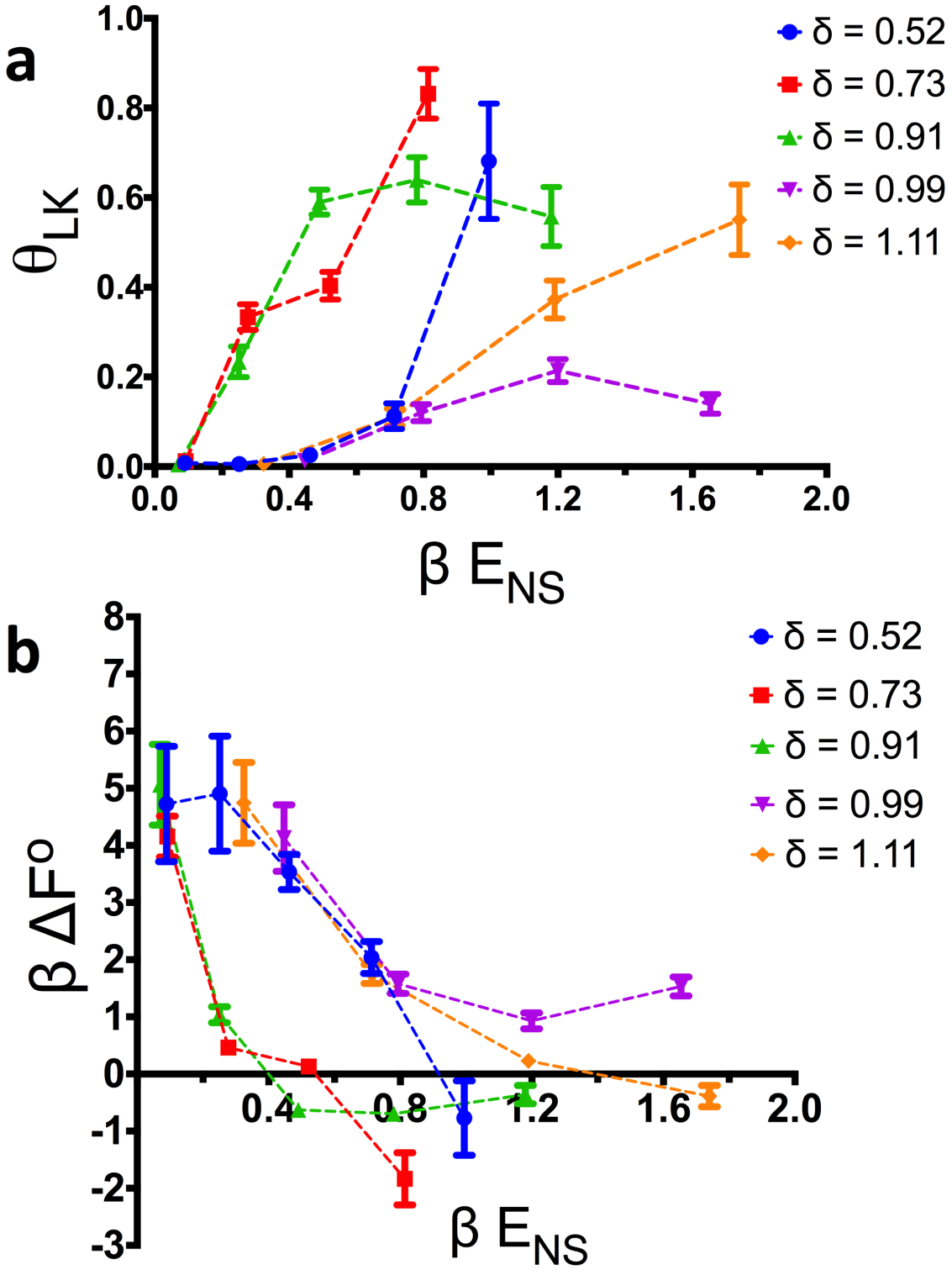
a
θLK
1.0
0.8
0.6
0.4
0.2
0.0
0.0
0.4
0.8
1.2
1.6
2.0
β ENS
δ = 0.52
δ = 0.73
δ = 0.91
δ = 0.99
δ = 1.11
b
β ΔF°
8
7
6
5
4
3
2
1
0
-1
-2
-3
0.4
0.8
1.2
1.6
2.0
β ENS
δ = 0.52
δ = 0.73
δ = 0.91
δ = 0.99
δ = 1.11

Figure 3.6 The fractional occupation curves for all five different key-to-dimple size ratios δ at 1.5 mM NaCl (panel a) and the free energy of formation of specific bonds for all five different δ at 1.5 mM NaCl (panel b) are plotted against nonspecific binding energy of interaction.

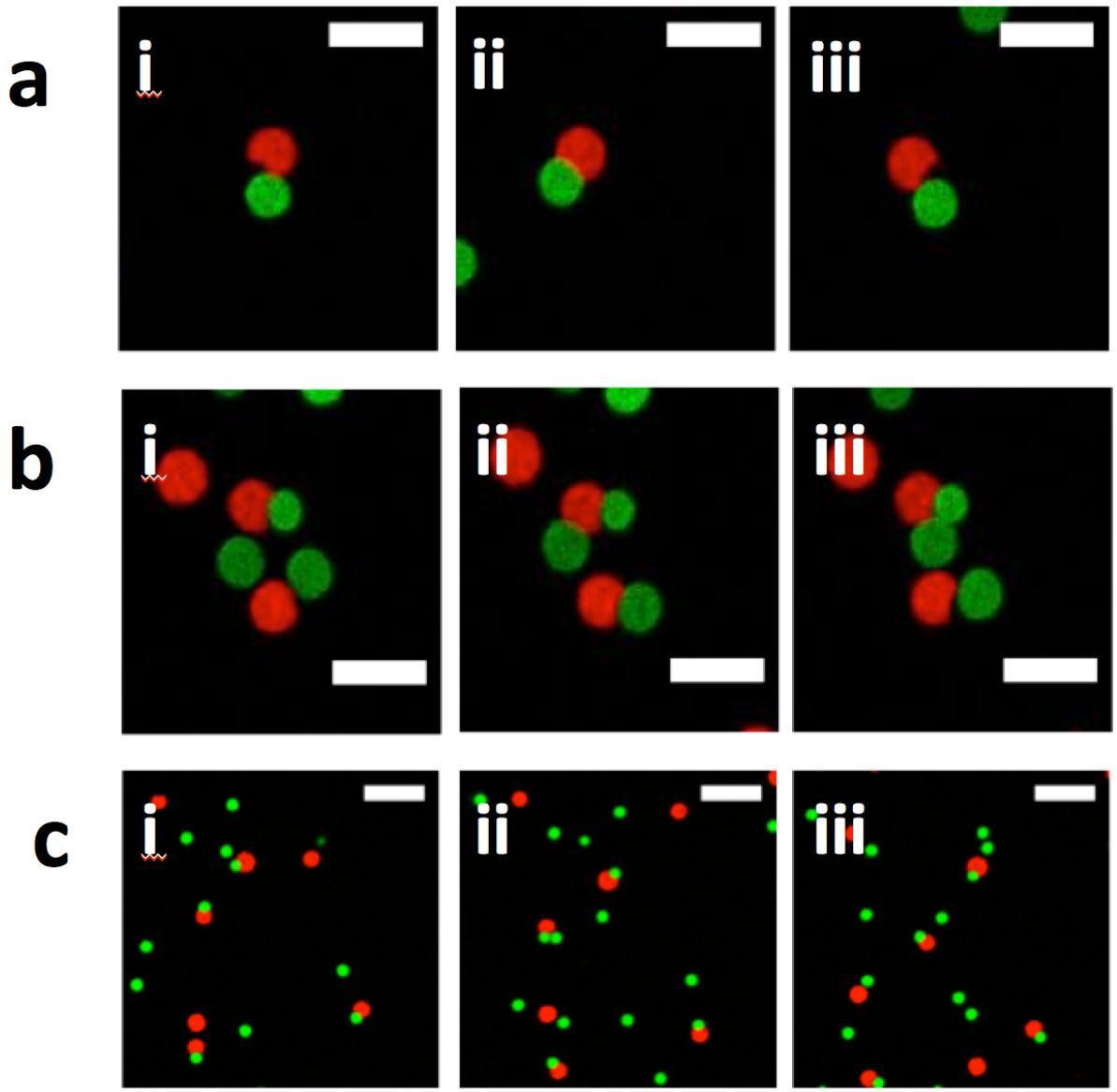

Figure 3.7 Panels a and b: Formation and unbinding of specific lock-key bonds for δ = 1.1 at 1.5 mM NaCl and 1.0 g/L polyethylene oxide concentrations. The time elapsed from panel a(i) to panel a(iii) is 87.2 seconds. The time elapsed from panel b(i) to panel b(iii) is 43.6 seconds. Panel c: Specific bonds between lock and key particles for δ = 0.9 at 1.0 mM NaCl and [PEO] = 1.0 g/L are not observed to unbinding over a time scale of ten minutes. The time elapsed from panel c(i) to panel c(iii) is 600 seconds. Scale bars on all figures on panels a and b: 5 μm. Scale bars on figures on panel c: 10 μm .

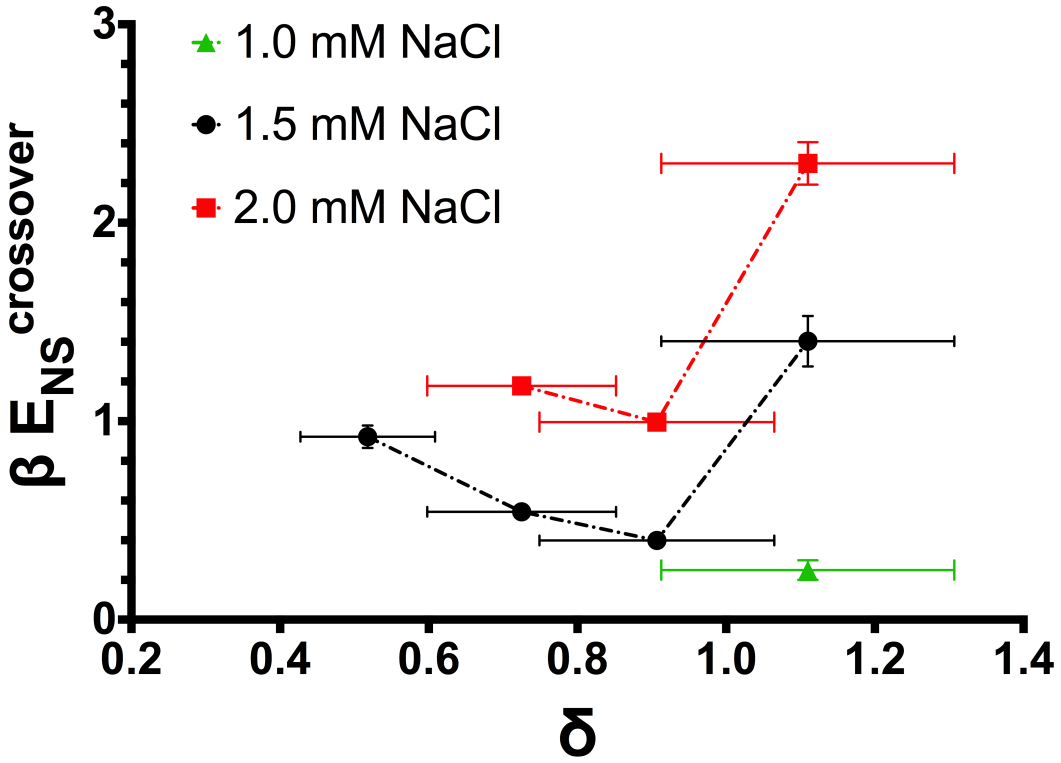

Figure 3.8 Crossover nonspecific binding energies of interaction are shown for all six different key-to-dimple size ratios at 1.0 mM NaCl (green triangles), 1.5 mM NaCl (black circles), and 2.0 mM (red squares). The crossover nonspecific binding energy for each δ are the interpolated point at which the free energy curves intersect the x-axis.

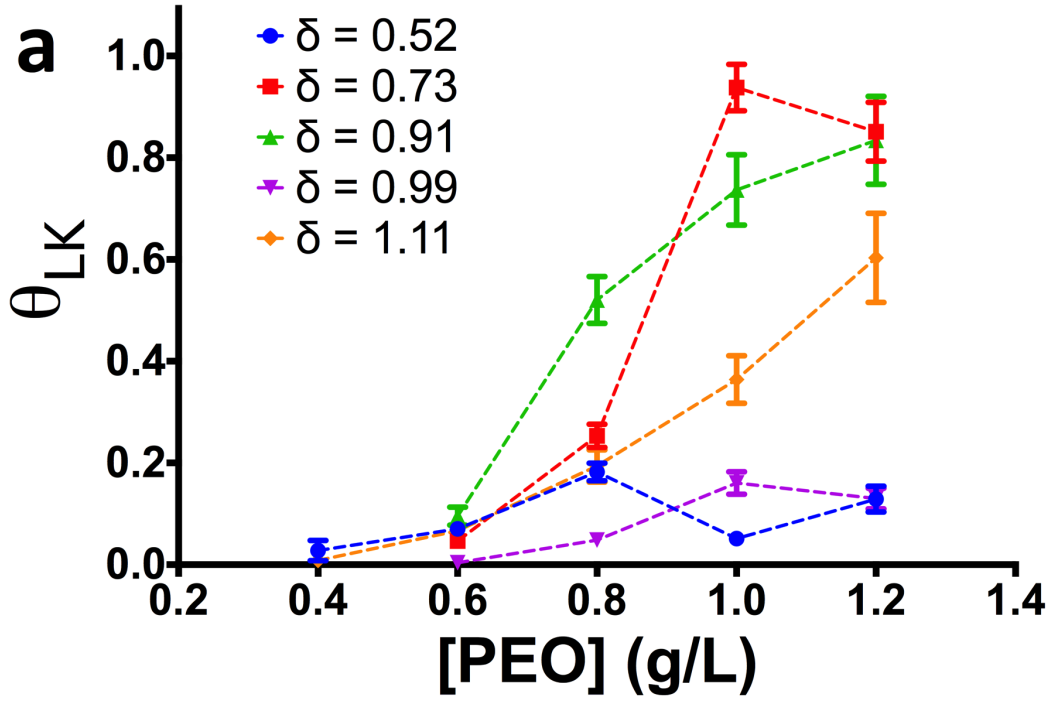
a
δ = 0.52
δ = 0.73
δ = 0.91
δ = 0.99
δ = 1.11
θLK
1.0
0.8
0.6
0.4
0.2
0.0
0.2
0.4
0.6
0.8
1.0
1.2
1.4
[PEO] (g/L)

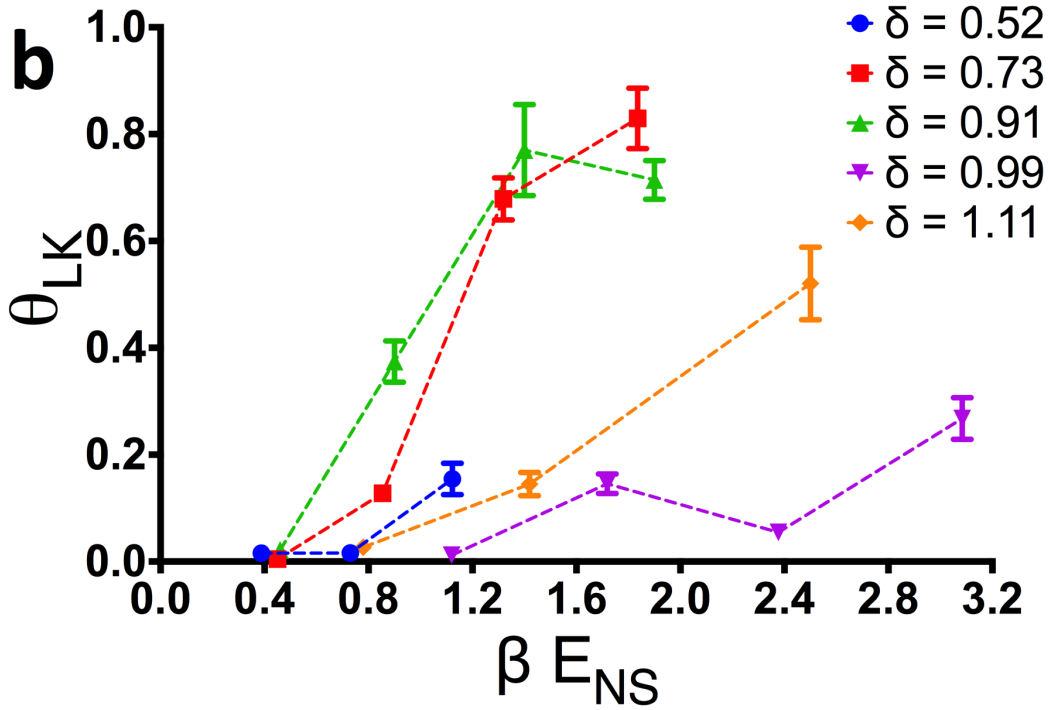
b
δ = 0.52
δ = 0.73
δ = 0.91
δ = 0.99
δ = 1.11
θLK
1.0
0.8
0.6
0.4
0.2
0.0
0.0
0.4
0.8
1.2
1.6
2.0
2.4
2.8
3.2
β ENS

Figure 3.9 In panel a, we plot the fractional occupation for five different key-to-dimple size ratios at [NaCl] = 1.0 mM. In panel b, we plot the fractional occupation at [NaCl] = 2.0 mM.

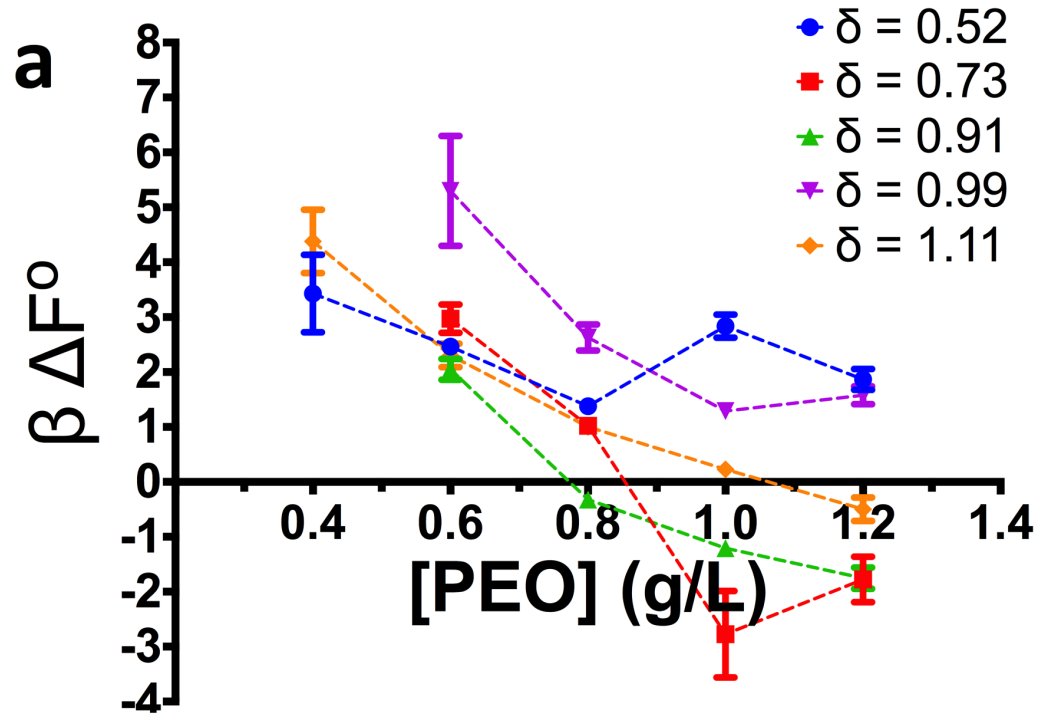
a
δ = 0.52
δ = 0.73
δ = 0.91
δ = 0.99
δ = 1.11
β ΔF°
8
7
6
5
4
3
2
1
0
-1
-2
-3
-4
0.4
0.6
0.8
1.0
1.2
1.4
[PEO] (g/L)

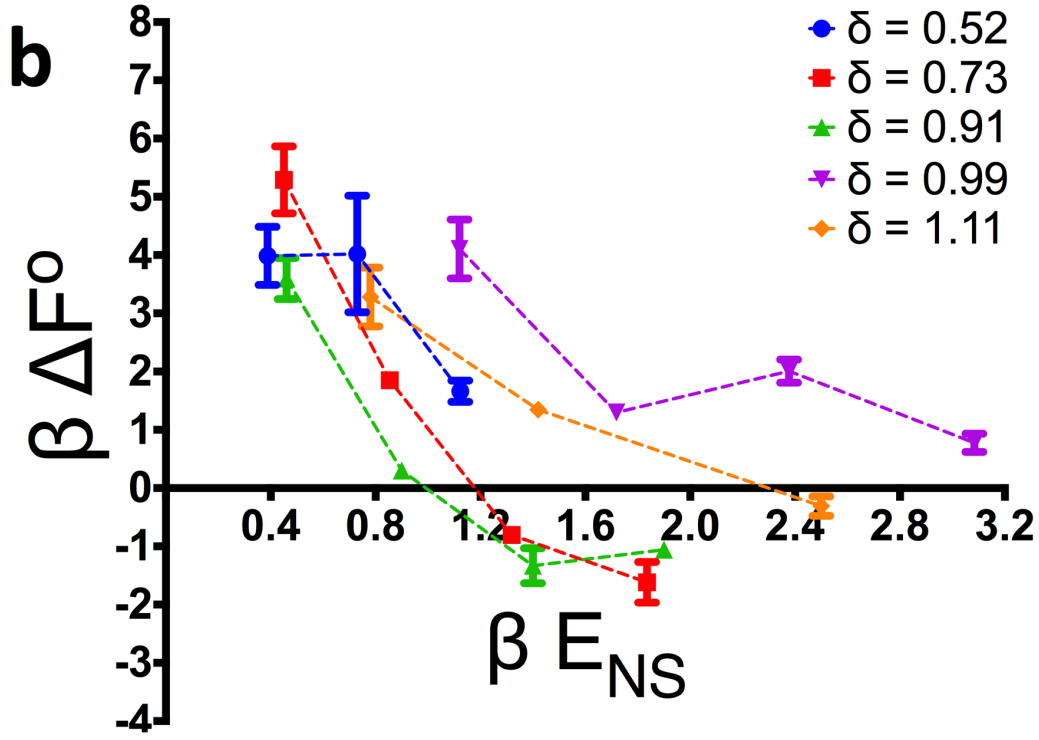
b
δ = 0.52
δ = 0.73
δ = 0.91
δ = 0.99
δ = 1.11
β ΔF°
8
7
6
5
4
3
2
1
0
-1
-2
-3
-4
0.4
0.8
1.2
1.6
2.0
2.4
2.8
3.2
β E_NS

Figure 3.10 On panel a we plot the free energy of formation of specific bonds at [NaCl] = 1.0 mM and, on panel b, for [NaCl] = 2.0 mM.

References

[1] S.C. Glotzer and M.J. Solomon, Nature Materials **6**, 557 (2007).

[2] M.J. Solomon, R. Zeitoun, D. Ortiz, K.E. Sung, D. Deng, A. Shah, M.A. Burns, S.C. Glotzer, and J.M. Millunchick, Macromolecular Rapid Communications **31**, NA (2009).

[3] A.A. Shah, H. Kang, K.L. Kohlstedt, K.H. Ahn, S.C. Glotzer, C.W. Monroe, and M.J. Solomon, Small **8**, 1457 (2012).

[4] A.A. Shah, B. Schultz, K.L. Kohlstedt, S.C. Glotzer, and M.J. Solomon, Langmuir **29**, 4688 (2013).

[5] A.A. Shah, B. Schultz, W. Zhang, S.C. Glotzer, and M.J. Solomon, Nature Materials **14**, 117 (2014).

[6] J. Zhang, E. Luijten, and S. Granick, Annual Review of Physical Chemistry **66**, 581 (2015).

[7] S. Sacanna, W.T.M. Irvine, P.M. Chaikin, and D.J. Pine, Nature **464**, 575 (2010).

[8] S. Sacanna, W.T.M. Irvine, L. Rossi, and D.J. Pine, Soft Matter **7**, 1631 (2011).

[9] L.C. Hsiao, B.A. Schultz, J. Glaser, M. Engel, M.E. Szakasits, S.C. Glotzer, and M.J. Solomon, Nature Communications **6**, 8507 (2015).

[10] T.K. Haxton and S. Whitelam, Soft Matter **8**, 3558 (2012).

[11] G. Munaò, P. O'Toole, T.S. Hudson, D. Costa, C. Caccamo, A. Giacometti, and F. Sciortino, Soft Matter **10**, 5269 (2014).

[12] M.F. Hagan, O.M. Elrad, and R.L. Jack, The Journal of Chemical Physics **135**, 104115 (2011).

[13] T.S. Skelhon, Y. Chen, and S.A.F. Bon, Soft Matter **10**, 7730 (2014).

[14] A.H. Gröschel, A. Walther, T.I. Löbling, F.H. Schacher, H. Schmalz, and A.H.E. Müller, Nature **503**, 247 (2013).

[15] Q. Chen, S.C. Bae, and S. Granick, Journal of the American Chemical Society **134**, 11080 (2012).

[16] L. Di Michele and E. Eiser, Phys. Chem. Chem. Phys. **15**, 3115 (2013).

[17] L. Di Michele, F. Varrato, J. Kotar, S.H. Nathan, G. Foffi, and E. Eiser, Nature Communications **4**, (2013).

[18] K. Miszta, J. de Graaf, G. Bertoni, D. Dorfs, R. Brescia, S. Marras, L. Ceseracciu, R. Cingolani, R. van Roij, M. Dijkstra, and L. Manna, Nature Materials **10**, 872 (2011).

[19] D.J. Beltran-Villegas, L. Colón-Meléndez, M.J. Solomon, and R.G. Larson, Journal of Colloid and Interface Science **463**, 242 (2016).

[20] E. Jankowski and S.C. Glotzer, Soft Matter **8**, 2852 (2012).

[21] H.N.W. Lekkerkerker and R. Tuinier, *Colloids and the Depletion Interaction* (Springer Netherlands, Dordrecht, 2011).

[22] A.D. Dinsmore, A.G. Yodh, and D.J. Pine, Nature **383**, 239 (1996).

[23] Y. Yang, T.D. Edwards, and M.A. Bevan, Journal of Colloid and Interface Science **449**, 270 (2015).

[24] T.D. Edwards, Y. Yang, W.N. Everett, and M.A. Bevan, Scientific Reports **5**, 13612 (2015).

[25] A. Fery and R. Weinkamer, Polymer **48**, 7221 (2007).

[26] L. Colón-Meléndez, D.J. Beltran-Villegas, G. van Anders, J. Liu, M. Spellings, S. Sacanna, D.J. Pine, S.C. Glotzer, R.G. Larson, and M.J. Solomon, The Journal of Chemical Physics **142**, 174909 (2015).

[27] D. Ortiz, K.L. Kohlstedt, T.D. Nguyen, and S.C. Glotzer, Soft Matter **10**, 3541 (2014).

[28] K.L. Kohlstedt and S.C. Glotzer, Physical Review E **87**, 032305 (2013).

[29] G.M. Whitesides and V.M. Krishnamurthy, Quarterly Reviews of Biophysics **38**, 385 (2005).

[30] D.H. Williams, E. Stephens, D.P. O'Brien, and M. Zhou, Angewandte Chemie International Edition **43**, 6596 (2004).

[31] T. Vo, V. Venkatasubramanian, S. Kumar, B. Srinivasan, S. Pal, Y. Zhang, and O. Gang, Proceedings of the National Academy of Sciences **112**, 4982 (2015).

[32] S. Asakura and F. Oosawa, Journal of Polymer Science **33**, 183 (1958).

[33] W.B. Russel, D.A. SAVILLE, and W.R. Schowalter, *Colloidal Dispersions* (Cambridge University Press, Cambridge, 2009).

[34] D. Kleshchanok, R. Tuinier, and P.R. Lang, Langmuir **22**, 9121 (2006).

[35] T.D. Edwards and M.A. Bevan, Langmuir **28**, 13816 (2012).

[36] W. Xu, A.D. Nikolov, and D.T. Wasan, AIChE Journal **43**, 3215 (1997).

[37] J.C. Crocker, J.A. Matteo, A.D. Dinsmore, and A.G. Yodh, Physical Review Letters **82**, 4352 (1999).

[38] X. Wei, X. Gong, and T. Ngai, Langmuir **29**, 11038 (2013).

[39] K. Devanand and J.C. Selser, Macromolecules **24**, 5943 (1991).

[40] D. El Masri, T. Vissers, S. Badaire, J.C.P. Stiefelhagen, H.R. Vutukuri, P. Helfferich, T.H. Zhang, W.K. Kegel, A. Imhof, and A. van Blaaderen, Soft Matter **8**, 6979 (2012).

[41] T.D. Edwards and M.A. Bevan, Macromolecules **45**, 585 (2012).

[42] C. Bechinger, D. Rudhardt, P. Leiderer, R.S. Roth, and S. Dietrich, Phys. Rev. Lett. **83**, 3960 (1999).

Chapter 4
Active motion in alternating current electric field-driven binary colloidal suspensions

Abstract

We observe the active motion of particles emerging from transient associations of unbound large and small colloids in low-frequency (≤ 2 kHz) alternating current electric fields perpendicular to the plane of motion of a binary colloidal suspension of unequally sized polystyrene spherical beads. Their propulsion is attributed to unbalanced electrohydrodynamic flow, as recently described for systems of asymmetric colloidal dumbbells by Ma et al. Two-channel confocal microscopy is used to image the active motion of the binary colloidal suspensions; particle trajectories are quantified by particle tracking algorithms. We find that the propulsion speed of particles and effective diffusion coefficients are comparable to other means of generating active motion; we find effective diffusion constants fifteen times larger than Brownian diffusion. The propulsion speed increases as the peak-to-peak voltage of the applied AC field is increased and the frequency of oscillation of the electric field is decreased. We analyze the short-time ballistic motion of large beads based on the number of neighboring small particles and find that large particles with two and three neighbors propel the fastest.

In this work, Mayank Agrawal and Matthew Spellings contributed custom written Python code to analyze particle trajectory dynamics.

Introduction

Active matter is far from thermal equilibrium: objects that exhibit active motion transform energy they collect from their environment into kinetic energy[1]. They exhibit interesting dynamic behavior, such as the dynamic birth and death of particle clusters[2,3] and giant number fluctuations[3,4]. The standard deviation of the mean number of particles N in equilibrium systems is proportional to $N^{1/2}$; out-of-equilibrium systems have been observed to have number fluctuations that are linearly dependent on the number of particles[5]. Examples of living active matter systems are schools of fish, bird flocks, insect swarms[6], and motile bacteria[7,8]. Examples of artificial active matter include self-propelled colloids such as catalytically active platinum/gold nanorods,[9] platinum/polystyrene Janus particles in hydrogen peroxide (H_2O_2) solutions,[10] carbon-coated Janus particles in near-critical water-2,6-lutidine mixtures exposed to green laser light[11], and composite 3-trimethoxysilyl propyl methacrylate particle/hematite particles that propel in dilute solutions of H_2O_2 upon ultraviolet light-activation[12,13].

Another class of self-propelling colloids are those driven by locally generated electrohydrodynamic flows. Recently, the propulsion of anisotropic colloidal dumbbell and dimer particles was observed in perpendicularly applied alternating current electric fields[14,15], and was found to depend on the amplitude of the applied electric field and its frequency. Platinum-polystyrene hybrid colloidal dimers have also been observed to propel in perpendicularly applied electric fields in the absence of hydrogen peroxide[16].

Colloidal particles that exhibit active motion are still subject to thermal fluctuations, but their motion exhibits ballistic behavior at short times relative to reorientation times dictated by the particles' rotational diffusivity[10]. At long times, the behavior of these active, Brownian particles converges to diffusive-like behavior with an effective diffusion coefficient that is strongly enhanced by the particles' activity.

Single-component particle suspensions in perpendicular electric fields do not display active motion. The behavior of these systems has been extensively studied[17-21] and is known to depend on the particles zeta potential and dielectric behavior, the electrolyte[22,23], as well as the amplitude and frequency of the applied electric field[19]. Critically, at low driving frequencies electrohydrodynamic (EHD) flow generated by the particles' distortion of the concentration polarization layer at the electrode can cause particles to mutually attract or repel depending on the direction of the EHD flow around the particles.[18]

The behavior of symmetric and asymmetrically sized colloidal dumbbells in perpendicularly applied electric fields has been recently reported[24] as well as the behavior of dumbbells asymmetric due to size or composition[16,25]. Symmetric colloidal dumbbells were observed to form reversible colloidal crystals where particles laid down or stood upright aligned with the field direction; asymmetric colloidal dumbbells formed Ising-like lattices where particles next to each other had alternating lobe orientations. At dilute concentration, these asymmetric colloidal

dumbbells were also observed to propel and also to form chiral clusters that could propel clockwise or counterclockwise[14].

In recent work, Ma et al. investigated the propulsion of irreversibly bound asymmetric colloidal dimers[15]. They detected electrohydrodynamic flow surrounding the particles that generated an effective attraction or repulsion of tracer particles. Under the experimental conditions investigated, sulfate polystyrene particles subjected to an external oscillatory field repelled tracer particles, whereas silica beads attracted them. A rigid dumbbell model of the propelling asymmetric colloidal dimers, which took into consideration the EHD flow around each lobe of the dimer, quantitatively described the propulsion of the dimers. Ma et al. found they could change the propulsion of colloidal dimers by changing particle characteristics such as size, zeta potential and composition, and applied field frequency[15]. This discovery, coupled to electrolyte-dependent EHD flow behavior observed by some[22,23], suggests colloidal beads in low-frequency AC electric fields can convectively entrain other particles without the need to bind the particles into irreversibly bound structures.

In this work, we observe colloidal propulsion in binary colloidal suspensions of unequal size particles when subjected to an external alternating current electric field. The dynamics of the binary colloidal suspensions of unequally sized carboxylated polystyrene spheres are observed by confocal laser scanning microscopy and quantified by image analysis and particle tracking. At constant salt concentration and particle concentrations, the amplitude and frequency of the

applied field is varied. We observe the emergent formation of transient, propelling colloidal clusters comprised of large particles surrounded by associating small particles. The number of associated small particles varies stochastically and is a determinant of the overall propulsion of the transient clusters. The phenomenon is reversible: when the field is turned off, particles revert back to normal diffusion.

We characterize the mean-squared displacement of the large particles as they undergo propulsion. We also determine the effect of the number of associated small particle on the short-time ballistic propulsion of the large particles. We find that the effective diffusion coefficient and propulsion speed of particles increase as the peak-to-peak voltage is increased and frequency of oscillation decreases. We also find that large particles surrounded by two and three small particle neighbors exhibit faster short-time ballistic motion than large particles associated with either a smaller or larger number of small particles.

Materials and Methods

Sample preparation

Dilute binary colloidal suspensions of 1.75 μm diameter carboxylated polystyrene (d = 1.75 μm ± 0.05 μm)(Polysciences, yellow-green dye, 2.7% solids) beads and 1.0 μm diameter carboxylated polystyrene (d = 0.99 μm ± 0.022 μm) (Life Technologies, red dye, 2% solids) beads are prepared by placing 2 μL of each bead suspension in 0.125 mM sodium chloride (NaCl) solution prepared with 18.2 MΩ cm deionized water. The zeta potential of the particles are -42.1 mV ± 1.2 mV for 1.75 um carboxylated PS spheres, and -48.2 mV ± 1.7 mV for 1.0 um carboxylated PS spheres. Samples are centrifuged at least twice and resuspended in 0.125 mM NaCl solution (κ^{-1} = 27.2 nm), then sonicated with an ultratip sonicator for three 1-second intervals. Then 25 μL of the suspension is loaded into the electric field device.

Electric field device preparation

Glass coverslips (35 mm x 50 mm, #1.0 thickness (Fisher Scientific)) are covered with a thin layer (~ 10 nm thick) of indium tin oxide (ZC&R Coatings). The ITO-covered glass coverslip are washed thoroughly and treated using existing protocols[20]. A 250 μm-thick insulating spacer (Thermo Scientific™ Gene Frame Seals) is placed on top of one of the ITO covered slides, forming a 25 μL chamber. After the sample is pipetted onto the bottom ITO surface, it is covered with the other ITO-covered glass coverslip. Thin wires (50 μm-thick T2 thermocouple alloy wire, Goodfellow Corporation) are taped onto the electrodes to ensure metal-to-metal

contact. These leads are connected to a function generator for application of a periodically oscillating potential.

Electric field application

We use a function generator (Digol DG1022) to apply a square-wave oscillating potential to the sample. We apply peak-to-peak voltages equal to 10 V, 15 V or 20 V, and a frequency of oscillation of 1 kHz, 1.5 kHz, and 2.0 kHz, to yield N = 9 total experimental conditions. Following an experimental protocol found elsewhere[26], we initially apply a potential of 20 V at 10kHz prior to beginning any of the experiments, and then decrease the frequency and/or voltage to the desired experimental value.

Confocal microscopy image acquisition, particle tracking and data analysis

Two-channel confocal imaging is performed using the resonant scanner of an inverted confocal laser scanning microscope (Nikon A1.R) using an oil-immersion 100x objective with numerical aperture NA = 1.45. Emission laser lines of 488 nm and 561 nm are used to excite the dyes on the yellow-green and red-dyed beads, respectively. Time series of the samples are acquired as the electric field acts on the samples at 7.5 fps ($t_{interval}$ = 0.133 s) for a total of 1000 frames. Images are acquired at a spatial resolution of 0.249 μm/pixel, and are $(512 \text{ pixels})^2$, for an image area of $(127.45 \text{ μm})^2$. Three series are acquired at every experimental condition reported.

Images from each channel were independently analyzed using the ImageJ/Fiji plugin Mosaic Particle Tracker[27], which finds individual particle centroids in each frame and links their trajectories using an algorithm based on the Crocker & Grier particle tracking algorithm[28]. Individual particle trajectories are input to the freely available TRACKPY code[29] to obtain the mean squared displacements of the large particles. For each image series, more than 200 trajectories were typically analyzed. Individual large particle mean squared displacements are averaged to generate the ensemble average at a given experimental condition, for each sample (N=3 replicates per experimental condition).

The ensemble average of the large particle mean-squared displacements is fitted to the single-particle active motion model, as explained below, using weighted non-linear least squares fitting using Matlab curve fitting software. We extract three fitting parameters from our data: the propulsion speed v, the diffusion coefficient D, and the characteristic reorientation time τ. To perform weighted fitting, we consider the weight to each data point i, corresponding to a particular lag time, to be given by the standard error of the mean $\sigma_{\bar{x}_i} = \frac{\sigma_i}{\sqrt{N}}$. Here σ_i is the standard deviation of the mean value of the data and N is the number of points averaged to obtain the mean-squared displacement at that lag time.

Nearest neighbor and velocity analysis

We observe that during their trajectories, large particles have varying numbers of small particle neighbors (see below). Using custom-written Python code, we obtain cross-particle pair correlation functions, which allow us to obtain a nearest-neighbor distance cutoff and, subsequently, a nearest-neighbor distribution of small particles around a large particle. We compute the cross-particle pair correlation functions for large and small particles, $g_{LS}(r)$ for all applied potential differences at frequency 1 kHz, averaged for all three samples at each condition. Using a cutoff distance extracted from the cross-particle pair correlation functions, we segment the trajectories of the larger particles by the number of small neighboring particles to investigate the effect of number of neighbors on the short-time ballistic motion of the large particles. Neighbor-dependent propulsion speeds are obtained by fitting a parabola to the average mean-squared displacement plots at short times (≤ 1.2 seconds), considering from N = 0 to N = 5 small particle neighbors.

Results and Discussion

On Figure 4.1, we show a typical trajectory for a 1.75 μm carboxylated polystyrene bead in 0.125 mM NaCl. This particle exhibits Brownian diffusion, evidenced by the randomly-directed displacements of the particle from frame to frame. The mean-squared displacement of a Brownian particle of radius R diffusing in two dimensions is given by $\langle \Delta r^2(t) \rangle = 4\ D\ t$, where D is the translational

diffusion coefficient of the particle, given by $D = {k_B T}/{6\pi\eta R}$, k_B is Boltzmann's constant, T is absolute temperature, η is the fluid viscosity, and t is the lag time between particle positions.

On Figure 4.2, we show a series of images of a binary colloidal suspension made of 1.75 μm (green) and 1 μm (red) carboxylated polystyrene beads under the effect of an alternating current electric field with peak-to-peak voltage of 20 V and frequency of oscillation equal to f = 1.0 kHz. By comparing Figure 4.1 and Figure 4.2, it is apparent the trajectory of the large, green particle in the AC electric field is qualitatively different than that of a passively diffusing particle. The trajectory of this particle is comprised of intervals of directed motion; the trajectory of the large particle appears to be influenced by the presence of small 1 μm particles in close proximity to it.

Active colloidal particles, in addition to being influenced by the thermal fluctuations of the medium surrounding them, transform energy acquired from their environment into kinetic energy. An active particle moving with speed v still undergoes changes in orientation due to rotational diffusion[30]. The two-dimensional mean-squared displacement of a particle with Brownian translational diffusion coefficient D, propulsion speed v, and characteristic reorientation time τ is given by

$$\langle \Delta r^2(t) \rangle = 4\,D\,t + \frac{1}{2}\,v^2\tau^2\left(\frac{2\,t}{\tau} + e^{-\frac{2t}{\tau}} - 1\right). \quad (1)$$

This expression also describes the two-dimensional mean square displacement of run-and-tumble particles that swim with constant speed v and suddenly change

their direction in Poisson-distributed time intervals[30]. At lag times t << τ, active particles whose mean square displacement is described by equation (1) exhibit mean-squared displacements which can be described by

$$\langle \Delta r^2(t) \rangle = 4\,D\,t + v^2 t^2. \quad (2)$$

The squared dependence in lag time can be explained by the ballistic behavior of particles: a body moving at constant velocity **v** has displacement equal to $(\boldsymbol{v}\,t)$ in a time t. At lag times t >> τ, the particle's mean square displacement is given by

$$\langle \Delta r^2(t) \rangle = 4\,D_{eff}\,t - {v^2\tau^2}/{2} \quad (3)$$

where D_{eff} is the effective diffusion coefficient and is given by $D_{eff} = D + {v^2\tau}/{2}$.

Figure 4.3 plots the ensemble average of the mean-squared displacement of all individual large particle trajectories for a peak-to-peak potential difference of 20 V and frequency f = 1 kHz. The shape of the mean-squared displacement displays short-time behavior that is non-linear in time, and approaches linear, diffusive behavior at longer times. We explore the short-time behavior of the mean-squared displacement of the particles below. We show similar plots for the mean-squared displacement at 10 V and 15 V, at 1 kHz, in Figures 4.4a and 4.4b, respectively. Comparison of the mean-squared displacements at varying peak-to-peak voltages (10 V, 15 V, and 20 V) while holding frequency fixed at 1 kHz show that mean-squared displacements for a given lag time increase with increasing peak-to-peak voltage.

On Figure 4.3, we include the standard error in the measurement of the mean-squared displacement at a given lag time t. Since large particles may exit the image acquisition frame due to their motion, not all trajectories have the same time duration, which explains why as lag time increases, so does the error in measurement of the mean-squared displacement. The best fit of the data to equation (1) is shown as a red line, which describes the mean-squared displacement of an active particle with propulsion speed v, diffusion coefficient D and reorientation time τ. In the inset plot of Figure 4.3, we plot the short time (for lag times $t \leq 1.2$ seconds) mean-squared displacement data and find that the data is also well-described by the short-time limit of equation (1), given by equation (2). At long times, the mean-squared displacement of the particles recovers the linear form one would expect from a diffusing particle, but now with a larger effective diffusion coefficient than expected for Brownian motion, as described by equation (3). On Figure 4.3, we also include the fit to the long-time mean-square displacement data using equation (3).

On Figure 4.5a, we show the percent difference between the experimental data and weighted non-linear least square fits to the data using equation (1) – the active motion model – and the linear mean-squared displacement of a passive Brownian motion in two dimensions for the experimental condition presented on Figure 4.3. Our analysis shows the mean-squared displacement at this condition is much better described by the active motion of equation (1), rather than that of purely Brownian diffusion. Average percent differences between the active motion

fit (equation (1)) and the experimental data do not exceed 2% for all active motion fits reported. On Figure 4.5b, we plot the percent difference between the experimental data and the two different fits at a peak-to-peak voltage of 10 V and frequency of oscillation f = 2 kHz. Although equation (1) fits the data marginally better, the percent difference between the models (active motion and Brownian motion) and the experimental data are comparable. In this case, we do not consider the particles in such samples -- 10 V at 2 kHz -- to be active movers and therefore do not report fitting parameters from equation (1) for this experimental condition in subsequent figures.

On Figures 4.6a and 4.6b, we plot the values extracted from the fits (equation (1)) for the propulsion speed (Figure 4.6a) and the characteristic time (Figure 4.6b). On Figure 4.6c, we plot the effective diffusion coefficient of the particles extracted from fitting the long-time mean-squared displacement of the particles to equation (3), as well as $D_{eff} = D + {v^2\tau}/{2}$ computed from the fit parameters D, v, and τ obtained from fitting the data to the active fit model (equation (1)).

On Figure 4.6a, we can see that particle propulsion speeds increase with increasing applied peak-to-peak voltage and decrease with frequency of oscillation of the field. This behavior is consistent with what is expected from EHD flow for permanent dimers [19] and what has been found in other experiments[15,18]. What is interesting and different about the present results however, is that the active motion is obtained in a suspension of unbound, isotropic particles, rather than in permanently bound dimers or asymmetric dumbbells, as has been shown in the

literature[14,15]. This difference highlights the fact that the active motion found here is emergent, arising from the collective proximity of the different size colloids as a result of attractive EHD flow, discussed below. When the electric field is turned off, we no longer observe transient associations between the particles; particles revert back to performing Brownian diffusion.

The largest propulsion speed was measured at 20 V and 1 kHz, with a value of v = 1.5 μm/s. The dashed line on Figure 4.6a represents the propulsion speed of gold/polystyrene Janus particles in 2% H_2O_2 solution, v ~ 1.1 μm/s, as reported in Howse et al[10]. The value of the propulsion speeds at 15 V, 1 kHz, and 20 V, 1.5 kHz are comparable to this value. As the peak-to-peak voltage is increased, we observe an increase in propulsion speed at fixed frequency, and a decrease in propulsion speed as frequency is increased at fixed applied voltage. At the experimental condition of 10 V and 2 kHz, the mean-squared displacement of the particle is no longer distinguishable from that due to Brownian motion. These results are in agreement with expected behavior due to EHD flow in which fluid flow is proportional to the field strength (therefore, applied voltage) and inversely proportional to the frequency of field oscillation.[15,19]

On Figure 4.6b, we show the values for the characteristic reorientation time τ extracted from the weighted fits. The dashed grey line represents the time scale for Brownian rotational diffusivity for a 1.75 μm particle, given by τ_r = 4.2 seconds. (A colloidal particle of radius R has rotational diffusion coefficient D_r given by

$D_r = {k_B T}/{8\pi\eta R^3} \equiv \tau_R^{-1}$.) Large statistical errors on the data, which rise from the quite gradual transition from ballistic to diffusive motion for these particles, preclude us from making a definite statement about changes in reorientation time with frequency and applied voltages. However, overall, the data suggests that reorientation times are smaller for higher applied voltages than for lower applied voltages. At 10 V, characteristic times are about 14 seconds. At 15 V, average characteristic times are between 8.4 and 12 seconds. At 20 V, the characteristic reorientation times range from 6.5 seconds at 2 kHz to 7.2 seconds at 1.0 kHz and 1.5 kHz.

The characteristic rotational times are approximately a factor of 2 to 3 times greater than predicted for a free particle undergoing Brownian motion. This difference could potentially be a consequence of the EHD flow itself: work by Santana-Solano et al.[31] suggests that the rotation rate of particles is affected by the EHD flow. In their study on the rotation of 4.2 μm-sized carboxylated polystyrene particles in clusters of particles brought together by EHD flow, they observed that the rotation frequency of boundary particles increased as applied voltage was increased, and that rotation frequencies were inversely proportional to the frequency of the applied field. An increase in rotation frequency would imply a decrease in reorientation time with increasing applied voltage, which is commensurate with the characteristic times we report. However, in our data, we do not observe frequency dependence to the characteristic time, yet the particles

whose motion we are tracking are freely moving by propulsion and not part of a cluster.

On Figure 4.6c, we plot the effective diffusion coefficient, D_{eff}, as it varies with applied peak-to-peak voltage and frequency of field oscillation. The dashed line on this figure represents the Brownian translational diffusion coefficient for 1.75 μm particles, D = 0.26 $\mu m^2/s$. Overall, we observe that higher applied voltages and lower frequencies of oscillation yield the greatest enhancements to the diffusion coefficient. At 10 V, the values for D_{eff} are comparable to Brownian diffusion. At 15 V and 1 kHz, D_{eff} = 1.9 $\mu m^2/s$, for a seven fold increase in diffusivity, comparable to the enhacement observed at 20 V and 1.5 kHz. At 20 V, 1kHz, we measure D_{eff} = 3.8 $\mu m^2/s$ for a nearly fifteen-fold enhancement of the diffusion coefficient. Thus, when particles propel faster, their effective diffusion coefficient increases, which can be seen by comparing Figures 4.6a and 4.6c.

Next, we turn our attention to how the propulsion of large particles is affected by the number of small particle neighbors surrounding them. On Figure 4.7, we show three representative trajectories of large particles over a total period of 16 seconds. On Figures 4.7a and 4.7b, a number of large particles are present in these frames, and it can be observed that they have different numbers of small particle neighbors. Focusing on the particular trajectory drawn on the image, we observe that this large particle is initially surrounded by one small particle, indicated by an arrow. Later, by the frame shown in Figure 4.7c, the particle has now acquired an additional neighbor. On Figure 4.7d, we observe that the particle being tracked has

two small neighbors. In subsequent frames (Figure 4.7e and 4.7f), the particle is surrounded by three particles. From the frame represented on Figure 4.7e to the one represented in Figure 4.7f, we can observe that the large particle's trajectory has turned, perhaps under the effect of encountering the third particle. On Figures 4.7g to 4.7i, we show the trajectory of a large particle as it exchanges small particles with neighboring large ones. On Figure 4.7g, we see that the large particle has two neighbors. Next, on frame 4.7h, it is surrounded by three small particles. Finally, on Figure 4.7i, it only has two small particle neighbors. These three trajectories show that the trajectories of large particles are influenced by the small particles surround it. Moreover, they show that the number of particles in the associated clusters is a function of time.

The electrohydrodynamic flow velocity of the fluid at a point r away from the center of a particle of radius R is given by [15]

$$u_{EHD}(r) = \frac{C}{\eta} \frac{K' + \frac{\omega}{\omega_{RC}} K''}{1 + (\frac{\omega}{\omega_{RC}})^2} \frac{3\,(r/R)}{2(1 + (r/R)^2)^{5/2}} \ , \qquad (4)$$

where $C = \varepsilon\varepsilon_o \left(\frac{V}{2h}\right)^2 \kappa h$. In these expressions, η is the fluid viscosity, R is the particle radius, K' and K'' are the real and imaginary components, respectively, of the particle's polarization coefficient, ε is the dielectric constant of the medium, ε_o the permittivity of vacuum, V is the applied peak-to-peak voltage, κ is the inverse of the Debye length, 2h is the separation between the electrodes, ω is the frequency of oscillation of the field, and ω_{RC} is the inverse of the RC time for charging the electrode, given by $\omega_{RC} = \kappa D_{ion}/h$, where D_{ion} is the diffusion coefficient of the

ions[15,19]. The resulting toroidal flow streamlines surrounding the particles are directed towards or away from the particle, depending on the polarization coefficient of the particle, whose real and imaginary parts depend on frequency, particle size, ion diffusivity, Debye length, particle zeta potential, and Stern layer conductance of the particles.

In our experiments, we always observe large particles leading the small ones. That is, large particles pull small particles. In the present case both types of particles are made of carboxylated polystyrene. The volume of dielectric material that is polarized by the electric field is 5.4 times greater for the larger spheres than for the smaller ones. In terms of equation (4), this means that the velocity of the electrohydrodynamic flow surrounding the large polystyrene particles is larger than that surrounding the smaller polystyrene particles. This velocity difference is enough to entrain small polystyrene particles in the convective EHD flow generated by the large particle, and propel the large particles while keeping the small particles close to it. The asymmetry in the EHD flow fields is what determines the direction of propulsion. This is why we observe large particles to move, roughly, in the direction defined by the sum of the line-of-center directors from the neighboring small particles to the large particle.

We are interested in quantifying how the number of small particles neighboring a large particle affects the propulsion speed of large particles. In 2D, a 1.75 μm-sized particle can be surrounded by up to eight 1.0 μm particles. (Briefly,

the number of particles that can be placed side-by-side around another is $\left[N_{small} = \frac{2\pi(r_{small}+r_{large})}{2r_{small}} = 8.6\right]$.) To investigate the effect of small particle neighbors on the motion of large particles, we need to identify the number of small particles in close proximity a large one. We use the cross-particle pair correlation function $g_{LS}(r)$, which is the probability of finding small particles as a function of distance r from the center of large particles. On Figure 4.8a, we plot $g_{LS}(r)$ at a driving frequency of 1 kHz for peak-to-peak applied voltages of 10 V, 15 V and 20 V. We see that for all three applied voltages the likelihood of finding a small particle is largest at small distances, and reduces to its expected value of 1 at large distance away from the large particle centers. For 15 V and 20 V, the likelihood of finding small particles close to the large particles is greater than at 10 V, evidenced by the relative height of the peaks in $g_{LS}(r)$. This implies that the entrainment of small particles by large particles is strongest at higher electric field amplitudes, which is expected, as the EHD flow magnitude increases with increasing field amplitude. We note that the cross-correlation function is itself a confirmation of the EHD coupling between the large and small particles. The particles themselves are stable. This fact, coupled with the low concentration of the specimens, indicates that the passive, equilibrium structure would be largely uncorrelated, and the strong peak absent.

We measure the number of nearest small particle neighbors next to a large particle using a distance cutoff given by 2.4 μm, shown in Figure 4.8a as a dashed vertical grey line. This distance is roughly equal to 1.5 small particle diameters away

from the large particle surface. Using this distance as our nearest-neighbor cutoff, we measure the nearest neighbor distributions at f = 1kHz for peak-to-peak voltages of 10 V, 15 V and 20 V, shown in Figure 4.8b. The small-nearest neighbor distribution functions plotted in Figure 4.8b indicate that, in all image frames acquired, roughly 20% of large particles have no small particle neighbors. Most large particles have one, two or three small particles surrounding them during the image capture. Less than 10% of particles have four or more neighbors. Visual evidence of neighboring small particles is provided on Figures 4.2 and 4.7.

We segment the large particle trajectories into runs in which the number of small particle neighbors are fixed. From these segmented particle trajectories, we measure the mean-squared displacement of large particles at each different number of small particle neighbors. On Figure 4.9a, we show the short-time (lag time ≤ 1.2 s) mean-squared displacements of large particles as a function of the number N of small particles surrounding it for one sample at 20 V, 1 kHz experimental condition. Note the ordering of the MSD curves with N in this plot: we see that large particles with one, two, or three neighbors achieve larger mean-squared displacements than particles with zero, four or five neighbors at the same lag times.

In order to obtain the propulsion speed of the particles, we fit the short-time mean-squared displacements to equation (2). Results for the propulsion speed are plotted on Figure 4.9b. For a fixed number of neighbors, the propulsion speed increases as the peak-to-peak voltage is increased. This agrees with results shown in Figure 4.6a, where the large particle ensemble average propulsion speed shows the

same pattern. At 10 V, large particles move relatively slowly compared to measured velocities at 15 V and 20 V. At 15 V, particles with two and three neighbors have propulsion speeds roughly equal to 0.8 μm/s. At 20 V, particles with two and three neighbors have speeds of 1.2 μm/s and 1.3 μm/s, respectively.

Large particles with two and three small neighbors are observed to have the largest propulsion speeds. As the number of small neighboring particles increases from three to four and five neighbors, the propulsion speed decreases. As mentioned above, large particles can be surrounded by up to 8 particles, and the asymmetry in the EHD flow is what determines the direction of propulsion. When the number of small particles surrounding a large one exceeds 4, we expect small particles to have a constraining effect on large particle motion, since the large particle would collide with them. Also, the sum of the forces acting on the large particles due to the effect of the small ones would decrease with more than 4 small neighboring particles, as the line-of-center directors start to cancel themselves out when summed.

Conclusions

We observe emerging propulsion of transient colloidal molecules formed upon the application of perpendicular, low-frequency alternating current electric fields onto a binary suspension of unequally sized carboxylated polystyrene particles. We observe that the mean-squared displacement of the particles is well-described by fitting it to the mean-squared displacement of active particles. As peak-to-peak voltage is increased and frequency of oscillation decreased, we measure larger propulsion velocities. The application of the field is observed to affect the rotation of the large particles via measurement of characteristic reorientation times that differ from the expected Brownian rotational diffusion scale. The effect of the field leads to enhanced effective diffusion coefficients up to sixteen times larger than the diffusion coefficient for Brownian translational motion. The number of small particles neighboring large ones is found to impact the propulsion speed of large particles; large particles with two and three small particle neighbors are observed to propel the fastest.

We perform our experiments solely with carboxylated polystyrene beads at constant salt concentration. We observe propulsion of carboxylated polystyrene particles without the need to perform surface modifications to the particle or to use hydrogen peroxide or other solvent mixtures. Our work, combined with previous work done in other groups, suggests that one can rationally control propulsion speeds of particles by choosing different electrolytes and changing relative particle sizes, composition and zeta potentials. We perform our experiments at relatively

dilute particle concentrations. Subsequent experiments may show what effect changing salt concentration and the relative and overall particle concentrations have on the dynamical behavior of this propelling particle system.

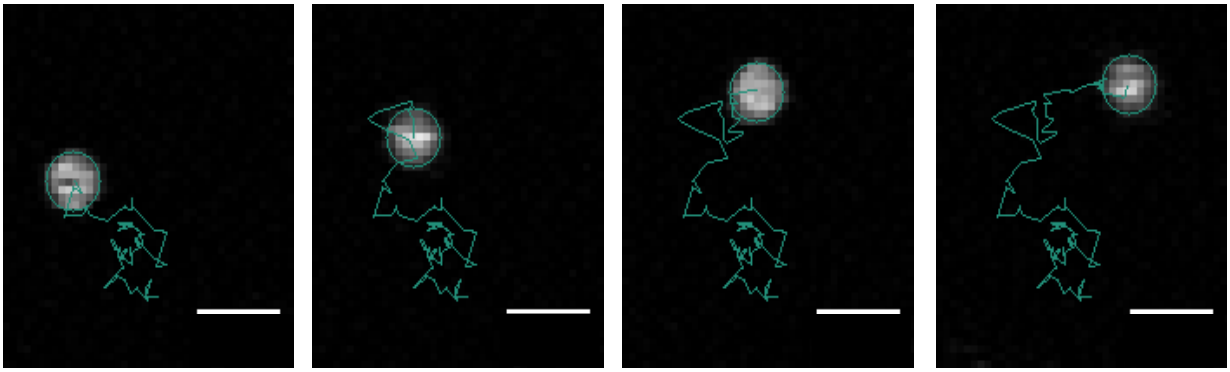

Figure 4.1 Brownian motion of a 1.75 μm polystyrene bead in water. Scale bars: 3 μm. Time between frames: 1.33 seconds. Images were also acquired at 7.5 fps.

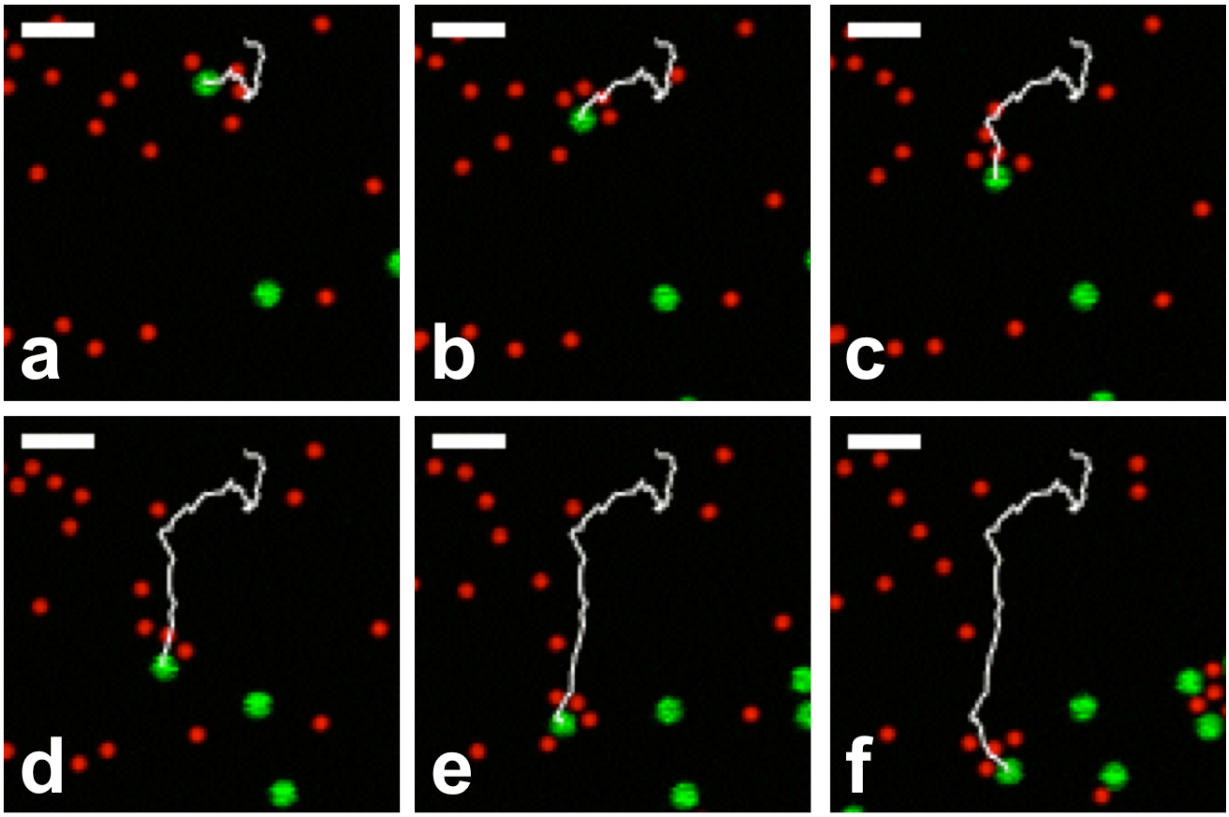

Figure 4.2 Trajectory of a 1.75 μm polystyrene bead driven by 20 V at 1 kHz. Scale bars: 5 μm. Time between frames: 1.33 s. The trajectory of this particle is markedly different than that of passive Brownian particles.

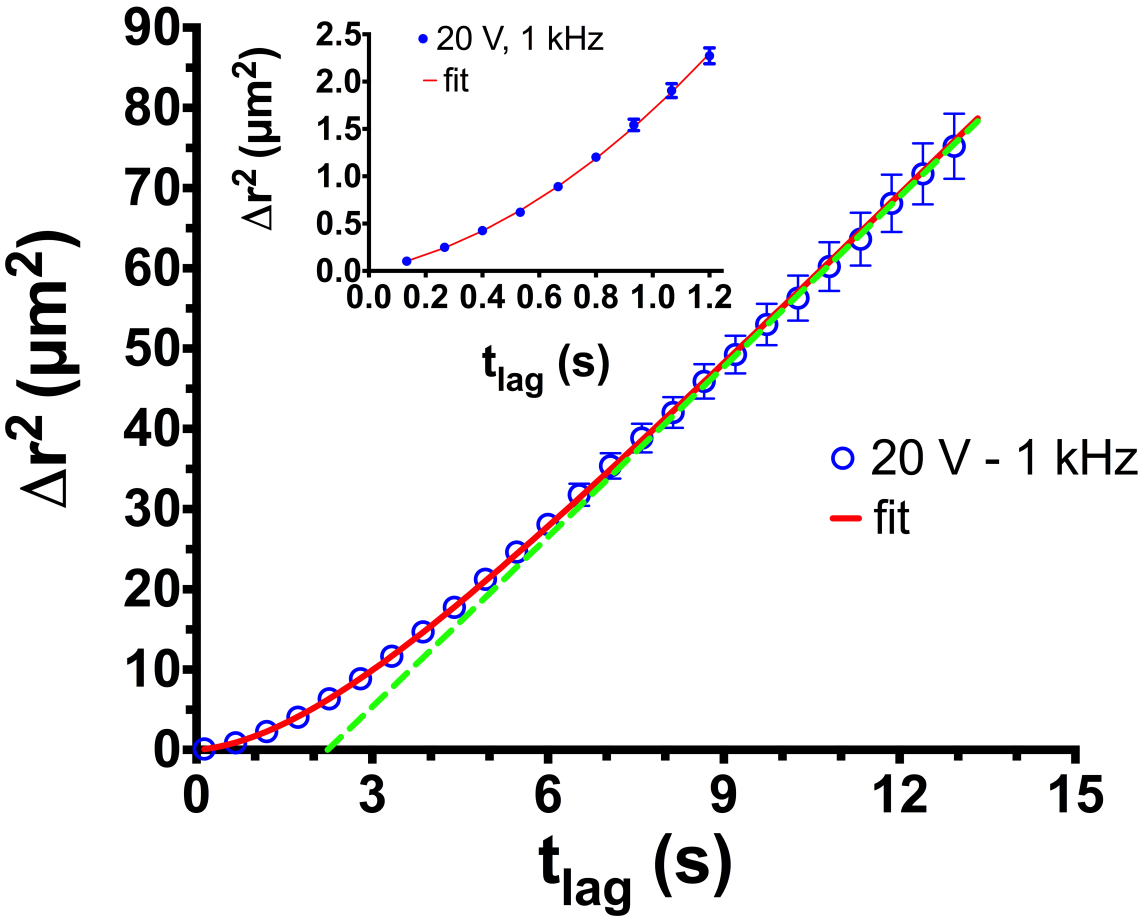

Figure 4.3 Ensemble average of all large particle trajectories' mean-squared displacements of large particles at 20 V, 1 kHz applied electric field. The experimental data (blue open circles) is fit by the mean-squared displacement for an active particle propelling with speed v, diffusion coefficient D and characteristic reorientation time τ (equation (1)), shown here as a red line. We show the mean-squared displacement data plotted every four data points for clarity purposes. The inset plot shows the short time ensemble mean-squared displacement, displaying ballistic behavior, fit by equation (2). The dashed gray line is the fit to the long-time mean-squared displacement data obtained from fitting equation (3) to the long time mean-squared displacement, which exhibits linear behavior.

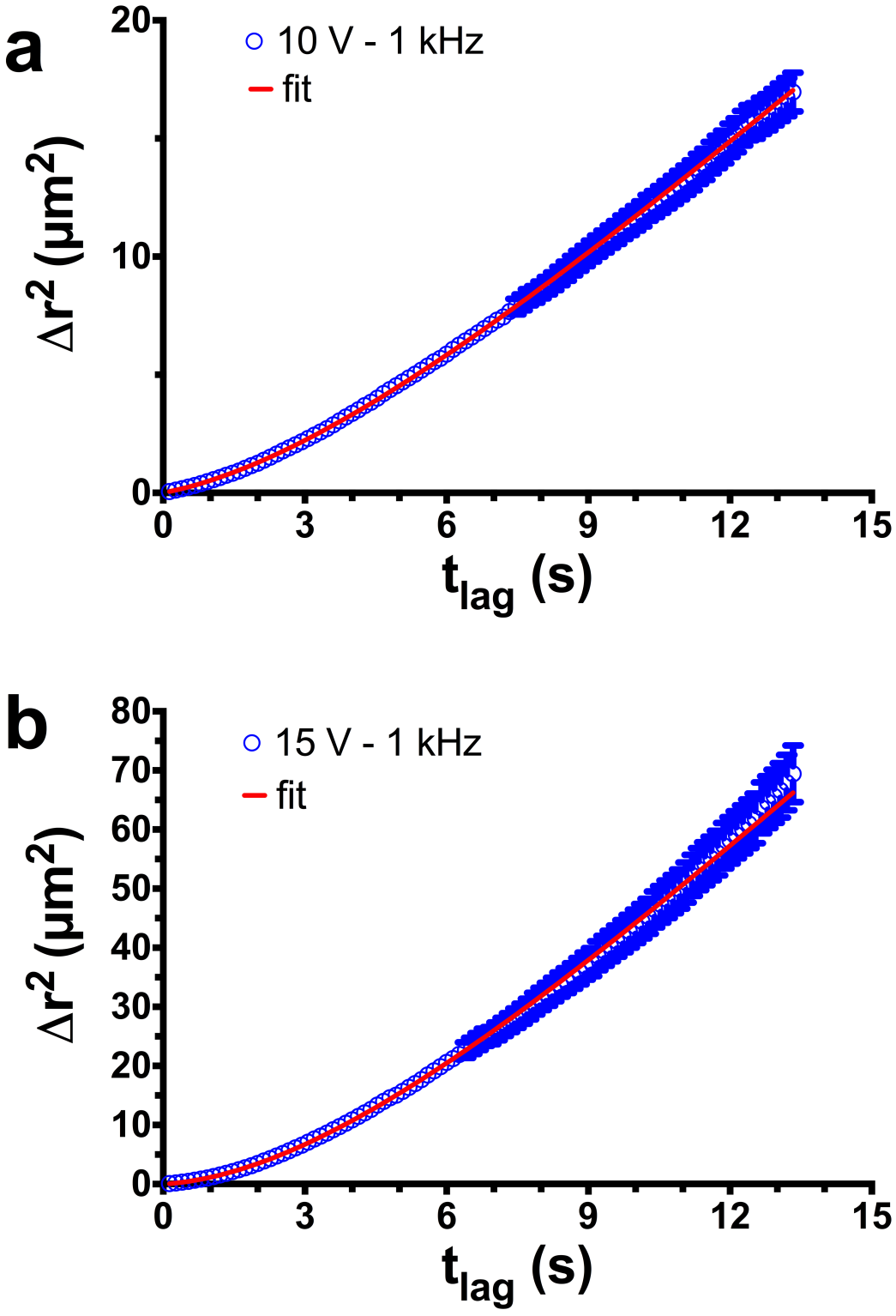
a
10 V - 1 kHz
fit
Δr^2 (μm^2)
0
10
20
0
3
6
9
12
15
t_{lag} (s)
b
15 V - 1 kHz
fit
Δr^2 (μm^2)
0
10
20
30
40
50
60
70
80
0
3
6
9
12
15
t_{lag} (s)

Figure 4.4 Ensemble average of all large particle trajectories' mean-squared displacements of large particles at (a) 10 V, 1 kHz applied electric field, and (b) 15V, 1kHz applied electric field. In both panels, experimental data is represented by blue open circles and fits to the active motion model mean-squared displacement, equation (1), are shown in as a red line.

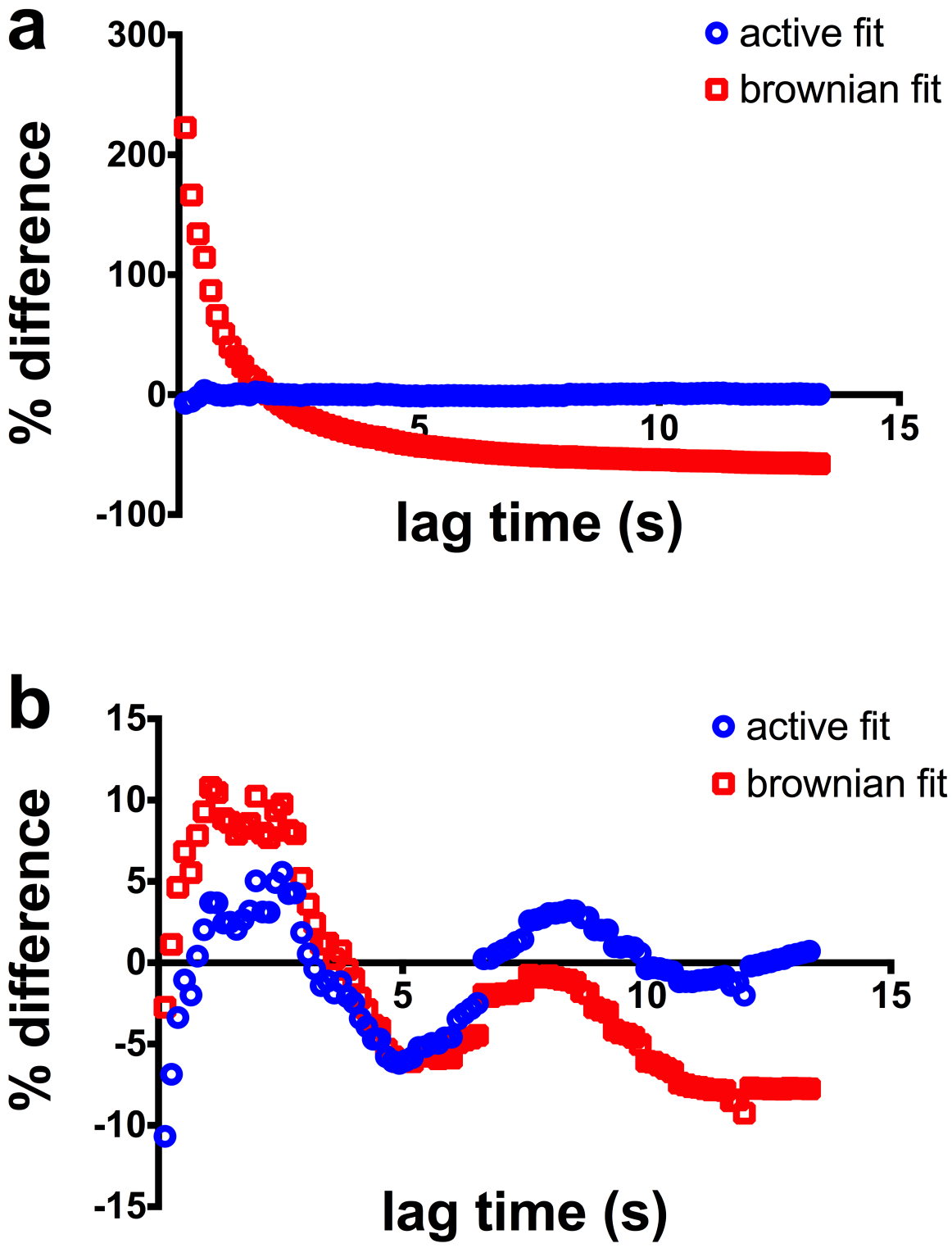
a
300
200
100
0
-100
% difference
5
10
15
lag time (s)
active fit
brownian fit
b
15
10
5
0
-5
-10
-15
% difference
5
10
15
lag time (s)
active fit
brownian fit

Figure 4.5 Panel (a) shows the percent difference between experimental mean-squared displacement and the active motion fit for MSD (equation (1)), shown as blue circles, and Brownian motion (red squares) for a peak-to-peak voltage of 20 V and frequency of oscillation f = 1 kHz. Panel (b) shows the same for 10 V and 2 kHz.

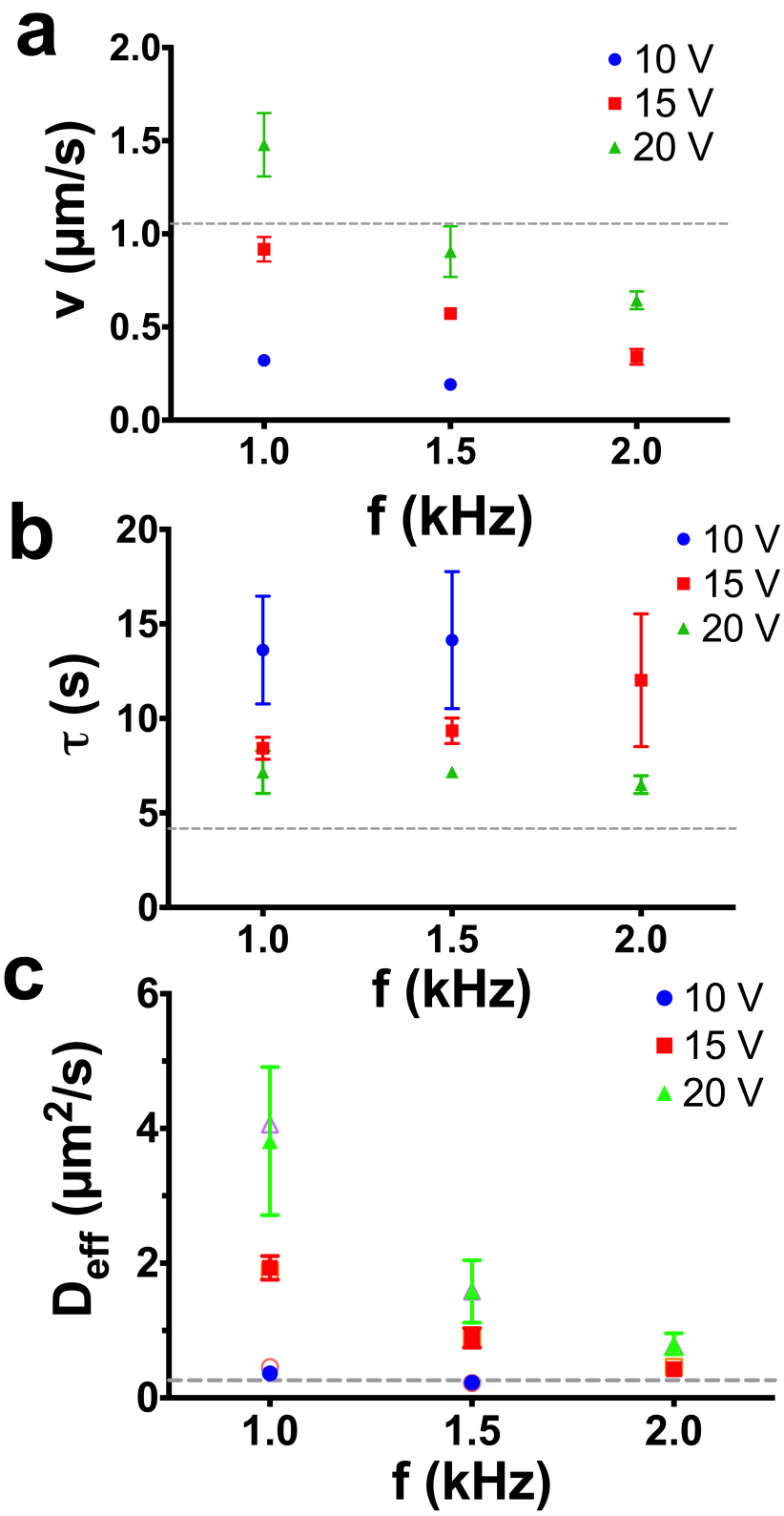
a
2.0
1.5
1.0
0.5
0.0
v (μm/s)
10 V
15 V
20 V
1.0
1.5
2.0
f (kHz)
b
20
15
10
5
0
τ (s)
10 V
15 V
20 V
1.0
1.5
2.0
f (kHz)
c
6
4
2
0
D_eff (μm²/s)
10 V
15 V
20 V
1.0
1.5
2.0
f (kHz)

Figure 4.6 *Fitted parameters extracted from mean-squared displacement model.* On panel (a) we plot the ensemble average propulsion speed of large particles as a function of applied frequency for all three different applied voltages. The dotted lines is the value of the propulsion speed of a Janus particle in 2% H_2O_2 solution, per Howse et al.[10]. On panel (b), we plot the characteristic reorientation time. The dotted line is the characteristic time of rotational diffusion, τ_r, for the 1.75 μm polystyrene beads. Panel (c) is a plot of the effective diffusion coefficient D_{eff} obtained via two different methods. Open symbols denote D_{eff} values obtained by using the values of D, v, and τ obtained from fitting the data to equation (1). Closed symbols denote D_{eff} obtained from fitting the long-time mean-squared displacements to equation (3). The dotted line is the Brownian diffusion coefficient for 1.75 μm polystyrene beads. On panels a thru c, data for 10 V is plotted as solid blue circles, 15 V as solid red squares, and for 20V, solid green triangles. On panel c, solid symbols denote D_{eff} obtained from fitting parameters of equation (1); open data symbols (pink circles for 10 V, orange squares for 15 V, and purple triangles for 20 V) denote D_{eff} obtained from long-time mean-squared displacement fits.

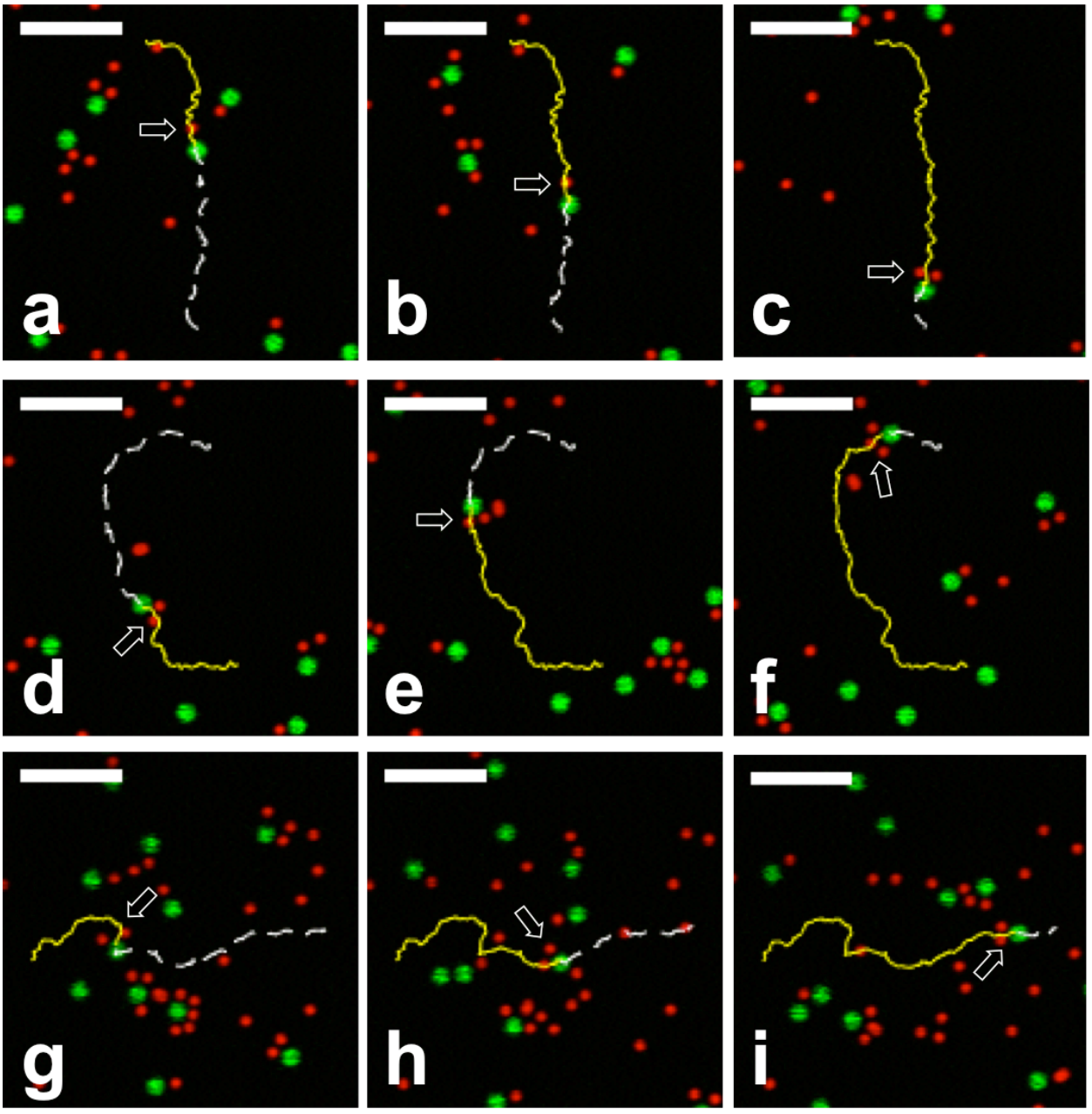

Figure 4.7 Entrainment of small particles by large particles. Panels (a)-(c), (d)-(f), and (g)-(i) show three different large particle trajectories, respectively. On all panels, solid yellow lines indicate where the tracked particle has been, and white dashed lines indicate the particles' future trajectories. The time interval between all frames is 4 s. Solid yellow and dashed white line trajectories are plotted for a total of 16 s. In these panels, it can be seen that the number of small particle neighbors surrounding a large particle is not constant in time. Arrows indicate the location of the small particles surrounding the large beads.

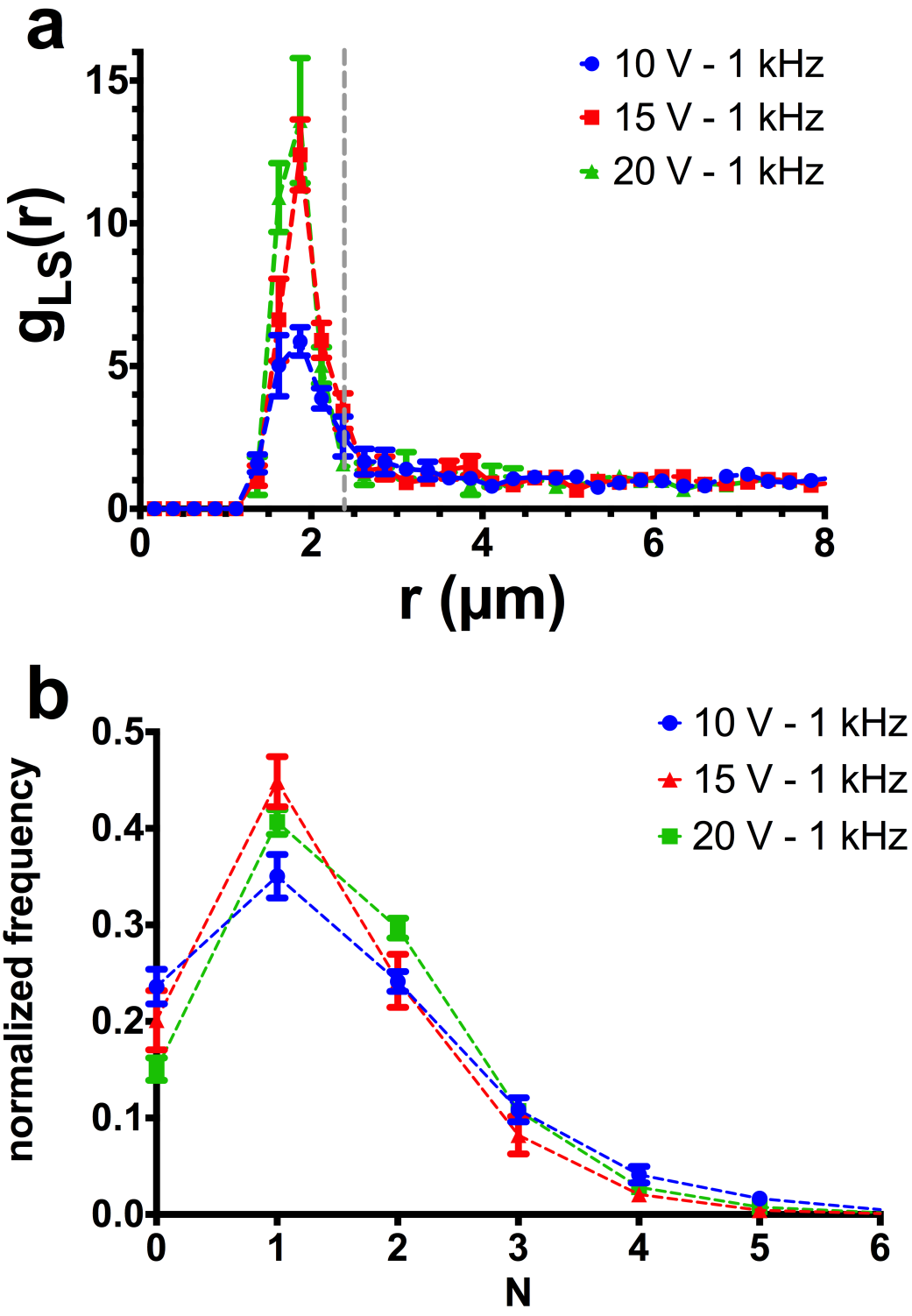
a
10 V - 1 kHz
15 V - 1 kHz
20 V - 1 kHz
$g_{LS}(r)$
r (µm)
b
10 V - 1 kHz
15 V - 1 kHz
20 V - 1 kHz
normalized frequency
N

Figure 4.8 Small-large particle pair correlation function and nearest neighbor distributions: On panel (a) we show the pair correlation function at 10 V (blue circles), 15 V (red triangles), and 20 V (green squares) at f = 1 kHz. The dashed grey vertical line represent the cutoff used to obtain the nearest neighbor distribution of small particles surrounding large particles shown in panel (b). Colors in panel (b) are the same as (a).

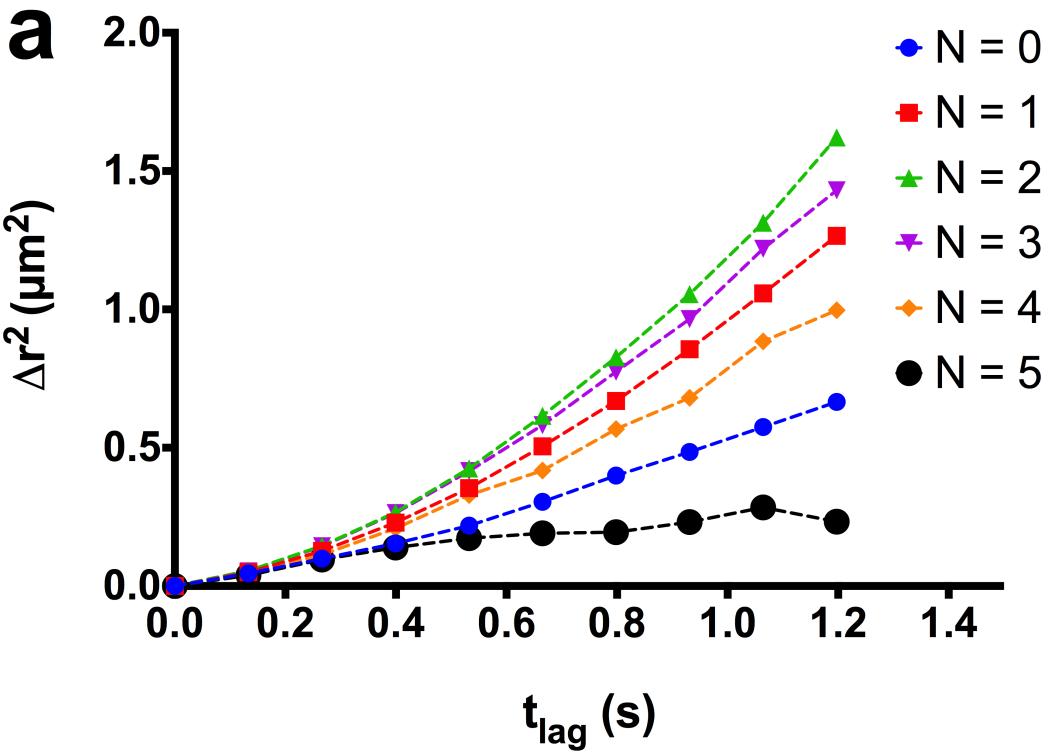
a
2.0
1.5
1.0
0.5
0.0
Δr² (μm²)
0.0
0.2
0.4
0.6
0.8
1.0
1.2
1.4
t_lag (s)
N = 0
N = 1
N = 2
N = 3
N = 4
N = 5

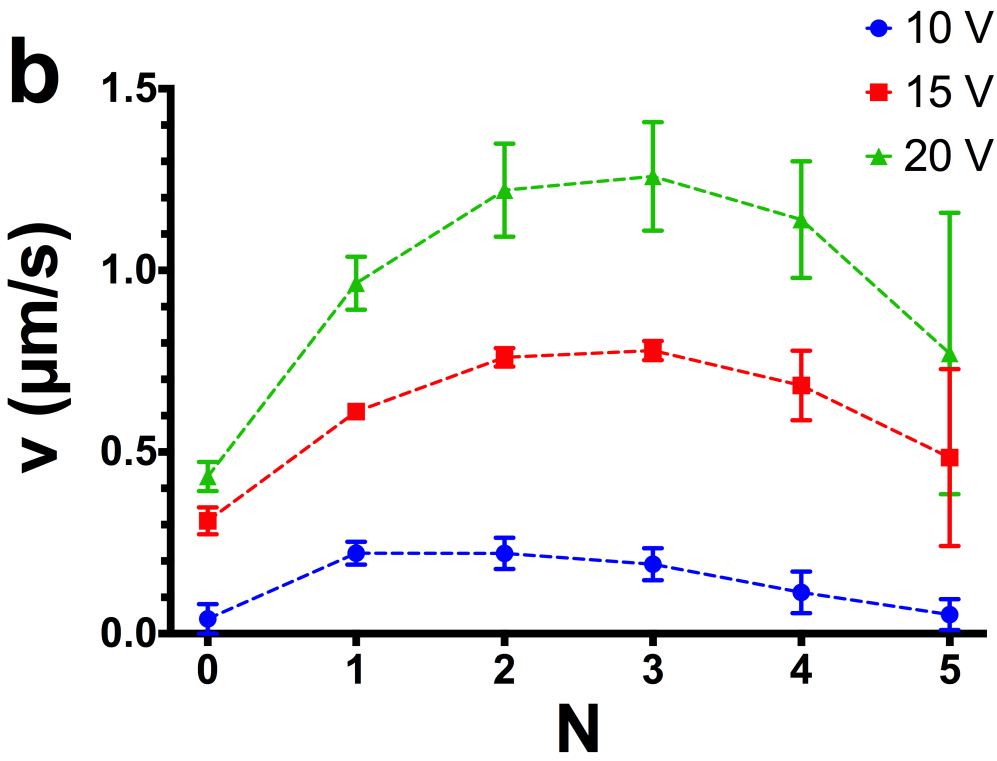
b
1.5
1.0
0.5
0.0
v (μm/s)
0
1
2
3
4
5
N
10 V
15 V
20 V

Figure 4.9 On panel (a) we plot the short-time mean-squared displacement of large particles as a function of how many small particle neighbors N surround them for a peak-to-peak voltage of 20 V and a driving frequency f = 1 kHz. (N = 0: small blue circles, N = 1: red squares, N = 2: green up-facing triangles, N = 3: purple down-facing triangles, N = 4: orange diamonds, N = 5: large black circles). On panel (b) we plot the propulsion speeds extracted from fitting short-time mean-squared displacements for 10 V (blue circles), 15 V (red squares), and 20 V (green triangles) at f = 1 kHz**.**

References

[1] S. Ramaswamy, Annual Review of Condensed Matter Physics **1**, 323 (2010).

[2] J. Palacci, C. Cottin-Bizonne, C. Ybert, and L. Bocquet, Physical Review Letters **105**, 088304 (2010).

[3] J. Palacci, S. Sacanna, A.P. Steinberg, D.J. Pine, and P.M. Chaikin, Science **339**, 936 (2013).

[4] S. Ramaswamy, R.A. Simha, and J. Toner, EPL (Europhysics Letters) **62**, 196 (2007).

[5] Y. Fily and M.C. Marchetti, Physical Review Letters **108**, 235702 (2012).

[6] G. Popkin, Nature **529**, 16 (2016).

[7] H.C. Berg and D.A. Brown, Nature **239**, 500 (1972).

[8] A.E. Patteson, A. Gopinath, M. Goulian, and P.E. Arratia, Scientific Reports **5**, 15761 (2015).

[9] W.F. Paxton, K.C. Kistler, C.C. Olmeda, A. Sen, S.K. St Angelo, Y. Cao, T.E. Mallouk, P.E. Lammert, and V.H. Crespi, Journal of the American Chemical Society **126**, 13424 (2004).

[10] J.R. Howse, R.A.L. Jones, A.J. Ryan, T. Gough, R. Vafabakhsh, and R. Golestanian, Physical Review Letters **99**, 048102 (2007).

[11] I. Buttinoni, G. Volpe, F. Kümmel, G. Volpe, and C. Bechinger, Journal of Physics: Condensed Matter **24**, 284129 (2012).

[12] J. Palacci, S. Sacanna, S.H. Kim, G.R. Yi, D.J. Pine, and P.M. Chaikin, Philosophical Transactions of the Royal Society A **372**, 20130372 (2014).

[13] J. Palacci, S. Sacanna, A. Abrahmian, J. Barral, K. Hanson, A.Y. Grosberg, D.J. Pine, and P.M. Chaikin, Science Advances **1**, e1400214 (2015).

[14] F. Ma, S. Wang, D.T. Wu, and N. Wu, Proceedings of the National Academy of Sciences **112**, 6307 (2015).

[15] F. Ma, X. Yang, H. Zhao, and N. Wu, Physical Review Letters **115**, 208302 (2015).

[16] S. Wang, F. Ma, H. Zhao, and N. Wu, ACS Applied Materials & Interfaces **6**, 4560

(2014).

[17] M. Trau, D. Saville, and I. Aksay, Science **272**, 706 (1996).

[18] W.D. Ristenpart, I.A. Aksay, and D.A. Saville, Physical Review E **69**, 021405 (2004).

[19] W.D. Ristenpart, I.A. Aksay, and D.A. Saville, Journal of Fluid Mechanics **575**, 83 (2007).

[20] F. Ma, D.T. Wu, and N. Wu, Journal of the American Chemical Society **135**, 7839 (2013).

[21] T.J. Woehl, B.J. Chen, K.L. Heatley, N.H. Talken, S.C. Bukosky, C.S. Dutcher, and W.D. Ristenpart, Physical Review X **5**, 011023 (2015).

[22] J.D. Hoggard, P.J. Sides, and D.C. Prieve, Langmuir **23**, 6983 (2007).

[23] T.J. Woehl, K.L. Heatley, C.S. Dutcher, N.H. Talken, and W.D. Ristenpart, Langmuir **30**, 4887 (2014).

[24] F. Ma, S. Wang, L. Smith, and N. Wu, Advanced Functional Materials **22**, 4334 (2012).

[25] F. Ma, S. Wang, H. Zhao, D.T. Wu, and N. Wu, Soft Matter **10**, 8349 (2014).

[26] W.D. Ristenpart, I.A. Aksay, and D.A. Saville, Physical Review Letters **90**, 128303 (2003).

[27] I.F. Sbalzarini and P. Koumoutsakos, Journal of Structural Biology **151**, 182 (2005).

[28] J.C. Crocker and D.G. Grier, Journal of Colloid and Interface Science **179**, 298 (1996).

[29] D.B. Allan, T.A. Caswell, and N.C. Keim, TRACKPY v0.2.

[30] M.E. Cates and J. Tailleur, EPL (Europhysics Letters) **101**, 20010 (2013).

[31] J. Santana-Solano, D.T. Wu, and D.W.M. Marr, Langmuir **22**, 5932 (2006).

Chapter 5
Conclusions and Future Directions

Binding kinetics and equilibrium thermodynamics measurements of anisotropic colloidal systems

In Chapter 2, we used confocal microscopy and particle tracking methods to study the kinetics of formation of lock-key dumbbells due to depletion interactions. The interaction potential between lock and key particles is a function of distance and relative orientation of key with respect to the lock dimple. This anisotropy leads to there being two possible configurations of lock and key colloids at contact: a key particle may be bound at the spherical surface of the lock or it could be bound at its dimple. We were able to distinguish between the two different particle configurations using the bond length distribution between lock and key centers, since the distance between lock and key centroids when the key is inside the lock dimple is smaller than the sum of the two particle radii, which is the distance between centroids when the particles are nonspecifically bound to each other. Our experimental results showed that lock-key dumbbells are formed by direct diffusion of the key into the lock dimple from bulk, or from the surface diffusion of key particles from the spherical surface of the lock particle to its dimple via a surface diffusion mechanism.[1]

We quantified the kinetic rate constants of all six different pathways in the interaction. Lock and key colloids may be free (unbound), bound to each other nonspecifically or specifically bound. Locks and keys may bind to each other from bulk, and unbind to bulk, or they may go from being nonspecific to specifically bound. We treat all binding in the system as reversible. We find that the rate of nonspecific to specific binding is independent of depleting polymer concentration. The rate of unbinding from the nonspecific binding state decreases as the depletant concentration increases. The impact that this has on assembly is that, as keys are more strongly bound to the surface, the more time a key particle is likely to be bound to the surface of the lock. This, combined with the constant NS – S kinetic rate constant, implies more nonspecifically bound keys will make it to the specific binding configuration at the lock dimple as the depletant concentration increases. We measure the success probability for NS-S binding, that is, the conditional probability that once a key is nonspecifically bound to the lock surface it will successfully bind to the lock dimple, and find that, indeed, the success probability increases as the depletion interaction increases.

Subsequent simulation and modeling work[2] studied the effect that nonspecific binding energy would have on the formation of specific bonds from a nonspecific binding configuration as a function of key to dimple size ratio. Simulations found that the kinetic rate of NS – S binding depends on the key to dimple size ratio, and so does the free energy of NS – S. The threshold nonspecific binding energy, defined as the nonspecific binding energy between locks and keys

where formation of nonspecific and specific bonds is equally likely, is minimized for keys slightly smaller than the lock dimple cavity size. This threshold nonspecific energy is an asymmetric function of key to dimple size ratio: if the key-to-dimple size ratio is reduced by ε from the aforementioned optimum value, the threshold NS binding energy increases by less than if the key-to-dimple size ratio is increased by the same ε. When there is good shape recognition between the key and the lock dimple surfaces, specific binding is favored over nonspecific binding at lower interaction strengths, i.e. lower depleting polymer concentrations.

In Chapter 3, we studied the effect that the key-to-dimple size ratio has on the free energy of formation of specific bonds. Our experimental results were consistent with the above-mentioned modeling and simulation work where keys smaller than the dimple cavity size formed specific bonds more readily that keys that were much smaller (less than 70%) or of equal or larger size than the dimple. If the size mismatch between lock dimple and keys is too small, the specific binding interaction energy is not large enough to overcome the loss of entropy of the key particle. When a key binds to the lock dimple, it loses configurational degrees of freedom, since it cannot explore configurations around the bulk volume. Entropy, however, penalizes a perfect key-dimple fit: when a key particle and the dimple perfectly match each other, the key particle has restricted configurational phase space to explore within the dimple since it cannot move within it. As the key to dimple size ratio increases from one, the convex, circular shape of the key is in less contact with the concave dimple, and gains more contact with the convex rim of the

lock dimple, which is not of negligible curvature. In fact, we performed our experiments by rotating the samples to eliminate the effect that lock dimple binding to the glass substrate of our capillaries would have on our experiments, since this is not a negligible interaction: it is as if a toroid of curvature given by the lock lip radius was in contact with a flat plate in the presence of depletants.

Our experimental approach, where particles are allowed to assemble and then a bond length distribution or pair distribution function is used to distinguish one spatial configuration state from the other, coupled with diffusion-migration modeling, can be extended to other systems, such as Janus particles or other types of patchy colloids[3], or to the binding of keys to locks with multiple cavities[4] to explore the kinetics of self-assembly of anisotropic particle systems. It would be interesting to study how the lock rim geometry affects binding; locks with a perfectly circular cavity have been synthesized[5], and it would be interesting to see what effect the sharp rim[6] has on the formation of specific bonds via the surface diffusion mechanism described on Chapter 2[1].

Our work on the free energies of formation of specific locks enables the experimental study of the rational design of lock-key assemblies, which have been shown to exhibit exciting symmetries[7,8]. Modeling work performed to this end suggests that interactions should be as nonspecific as possible while promoting specific binding assembly[2], consistent with studies on the self-assembly of protein crystals[9].

Simulations of assemblies of reconfigurable lock-key colloidal molecules[7,8] suggest the formation of many exciting crystalline phases, depending on lock-key size ratios, the bond length between the particles, and the type of lock-key colloidal molecules formed. As first presented by Sacanna et al.[10], lock-key colloids may form different colloidal molecules based on the number of locks that dock around a central spherical key. To experimentally realize predicted lock-key crystalline assemblies, it would be useful to study the effect that changing particle ratios would have on the formation of different types of lock-key colloidal molecules, as well as the effect of changing overall particle concentration. A strategy that could be used to promote the formation of lock-key bonds is to apply electric fields, as recently shown by Kamp et al.[11] Another experimental possibility is to work with lock and key colloids in organic solvents. An experimental procedure to transfer 3-trimethoxysilylpropyl methacrylate colloidal particles from aqueous solvents to apolar solvents has already been developed[12], and would enable refractive index and density matching of the suspensions, and use of polystyrene polymer as depletant. This could lead to studies of lock-key colloidal structure formation that are free from the effect of sedimentation.

We performed a few experiments at higher overall particle concentrations using one of the two best binding lock-key pairs in our experiments (key to dimple size ratio $\delta = 0.9$) made of 1.75 μm polystyrene keys and 2.4 μm lock particles. On Figure 5.1, we show a binary colloidal gel of lock and key particles prepared at a 3:1 lock-to-key number ratio at 0.1 mM NaCl and 1.0 g/L polyethylene oxide (M_v =

600,00 g/mol). The total particle concentration in this suspension was less than 30% volume fraction. The structures shown in this image merit further study: recent simulation work predicts the formation of empty liquids of colloidal dimpled particles[13]. Does the structure shown in Figure 5.1 have regions where empty liquids are present? How does the presence of keys affect the formation of that phase? On Figure 5.2, we show a colloidal suspension of locks and keys with key-to-dimple size ratio $\delta = 0.9$ that has been tilted at a slight angle with respect to the horizontal and allowed to assemble overnight at 1.0 mM NaCl and 1.0 g/L PEO, showing the suitability of using gravitational fields to crystallize lock-key colloids[14], and study the effect of packing fraction on lock-key colloidal assembly. Both Figure 5.1 and 5.2 are examples of potential further experiments that can be conducted toward the self-assembly of lock-key colloidal structures. Moreover, the abundance of lock-key bonds observed in these images for this particular pair of binders indicates experimental agreement of the the suitability of lock-key pairs with key to dimple size ratio slightly below one for increasing the yield of specific lock-key bonds.

Binary suspensions in perpendicular AC electric fields

In Chapter 4, we presented experimental evidence of propulsion of particles in binary colloidal systems under the action of a perpendicular alternating current electric field. We used carboxylate polystyrene particles of different sizes, and observed that large particles propel while accompanied by one or more small

particles surrounding them. The reason why particles propel is due to unbalanced electrohydrodynamic flow, which arises in the system as the dipole fields of the particles perturb the concentration polarization layer that forms over the electrodes in the system. In our work, we observed that we could obtain enhancements to the large particle diffusion coefficient of up to fifteen times the diffusion coefficient due to Brownian motion. We found that particle velocities increase with increasing applied peak-to-peak voltage and with decreasing oscillation frequency. Small-large particle nearest-neighbor analysis enabled us to determine that large particles associated with two or three small particle neighbors has the fastest short-time propulsion speeds for three different peak-to-peak voltages at constant frequency of oscillation.

By definition, active Brownian particles have reorientation times given by the inverse of their rotational diffusion coefficient. It would be interesting to study the rotation rates of the particles as they are acted upon by the electrohydrodynamic flow. Anisotropic particles such as dimpled colloids might be promising candidates for generating more enhanced directed motion via this mechanism. In an electric field, lock particles align their dimple perpendicularly to the direction of the field, since this minimizes the interaction energy between the field and the particle's dipole[11]. This could have an effect of slowing down the rotational diffusion of a lock particle in low-frequency AC electric fields like the ones we have used in our experiments, which would have the effect of increasing the ballistic motion regime of the particles – it would result in larger effective diffusivities.

Work by Ma et al.[15] established that one can change the propulsion speeds of colloidal dimers by changing the zeta potential of the particles or their composition. Apart from using carboxylated polystyrene particles, we also made a suspension with 3-trimethoxysilyl lock colloids and sulfate polystyrene spheres. On Figure 5.3, we show an image of a suspension of colloidal lock particles and sulfate polystyrene spheres driven at a frequency of 1 kHz at a 20 V peak to peak voltage over a gap of h = 250 μm. Since the lock particles can be imaged using confocal laser scanning microscopy, we tracked their motion. On Figure 5.4, we show the self-part of the van Hove correlation function for a suspension of locks and PS particles that was driven at a peak-to-peak voltage of 20 V, and where the frequency was swept from 10 kHz to 1 kHz as the sample was imaged. Figure 5.4 shows exciting dynamic behavior: we observe that the self-part of the van Hove correlation functions show broad shoulders uncharacteristic of Brownian motion. The self-part of the van Hove correlation function quantifies the likelihood of given particle displacements for fixed lag times. These results suggests it may be fruitful to investigate particle dynamics in these systems in more detail by, for example, changing the electrolyte used, using different particle combinations, and changing the amplitude and frequency of the applied electric field. The use of anisotropic particles, such as lock colloids, seems promising too, since anisotropic particles can exhibit preferred orientational configurations in electric fields[16-18], which, combined with unbalanced electrohydrodynamic flow, might lead to higher propulsion velocities due to reduced rotational motion of the lock particles in the field.

❖

In this dissertation, we have found that anisotropic lock-and-key colloids may form specific bonds via diffusion from bulk or a surface-diffusion mechanism that allows keys particle to diffuse to the lock dimple. We have also found that specific binding is favored for lock-key particle combinations where the key size is smaller than the lock dimple, in agreement with existing simulation work. The research that we have done regarding lock-and-key binding may be extended to study the kinetics and thermodynamic behavior other anisotropic particle systems, such as Janus particles, where different binding states can be easily identified via optical microscopy and particle tracking methods.

We have also investigated and characterized active motion in binary colloidal suspensions acted upon by an oscillating perpendicular electric field. To the best of our knowledge, this is the first active colloidal particle system studied where the propelling particles are not modified to be anisotropic but active motion is generated by the proximity of two different isotropic colloidal spheres via electrohydrodynamic flow. This system may lend itself to further study of collective active motion, such as phase separation and dynamic clustering studies.

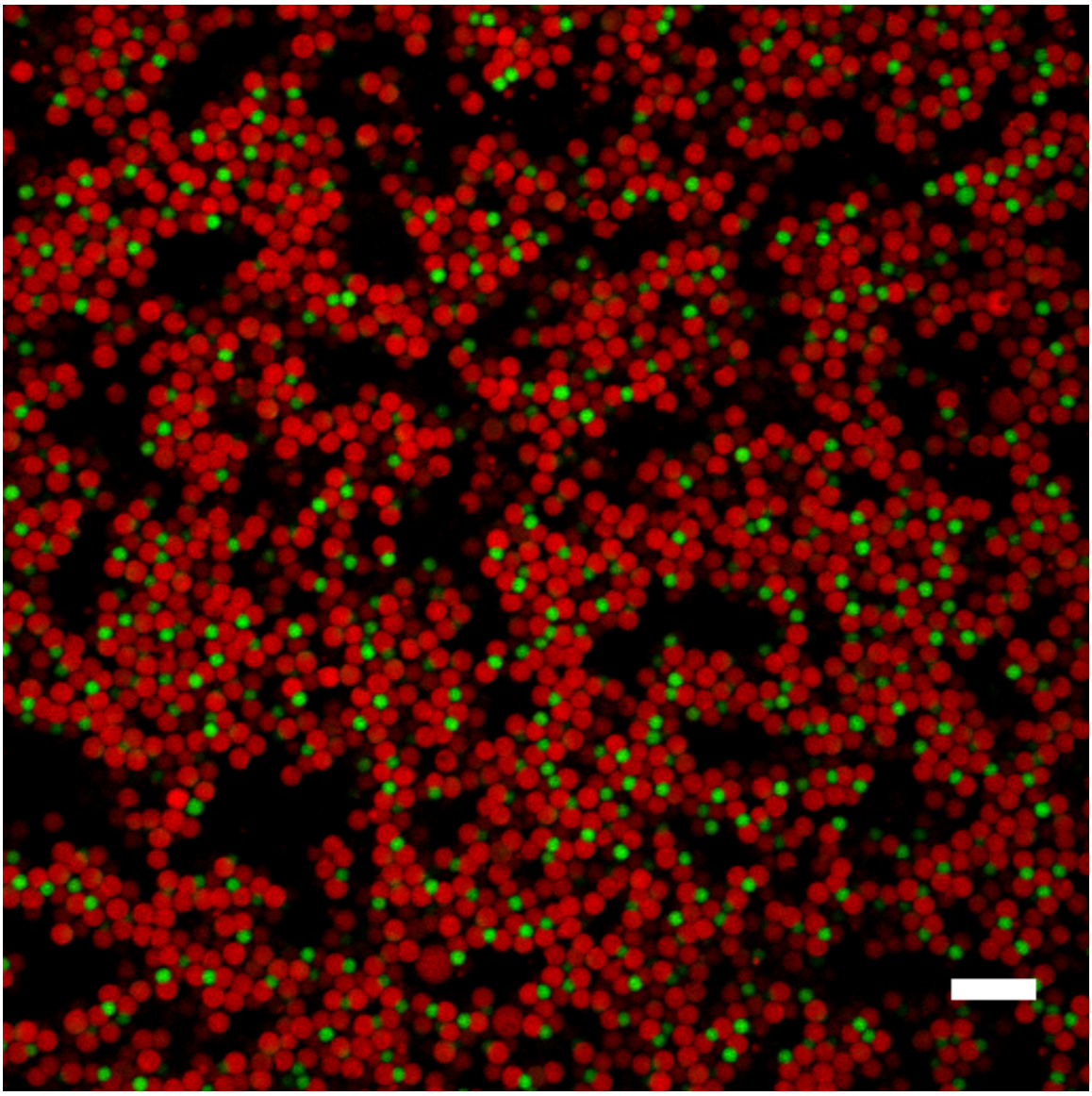

Figure 5.1 Lock-and-key colloidal gel prepared at 0.1 mM NaCl and 1.0 g/L PEO (M_v = 600,000 g/mol) at a stoichiometric number ratio of 3 (three locks for every key). Notice the abundance of specific bonds. Scale bar: 10 μm.

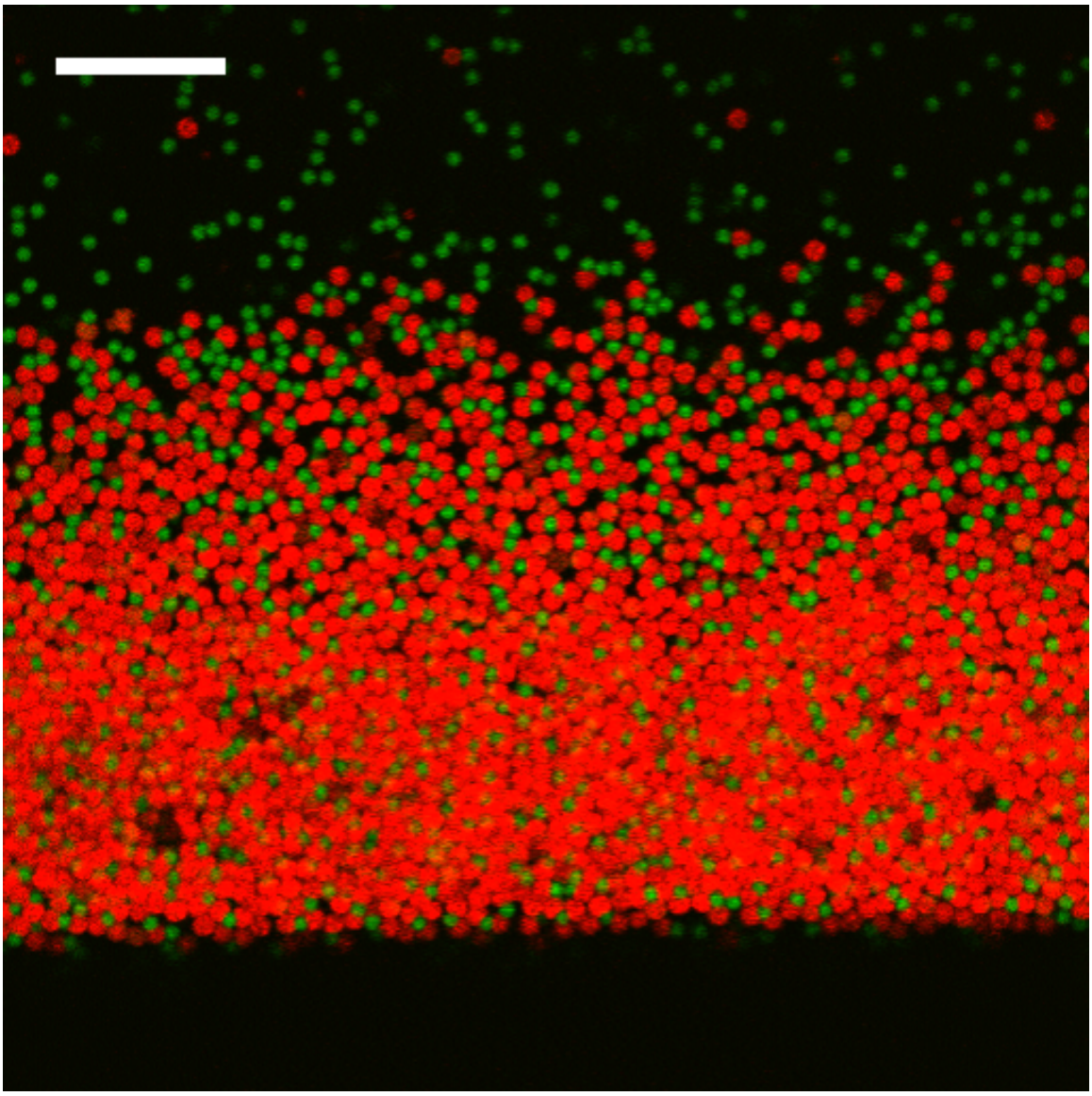

Figure 5.2 Self-assembly of lock-and-key colloids at 1.0 mM NaCl and 1.0 g/L PEO. The sample was titled at a slight angle overnight to promote the densification of the system. Scale bar: 20 μm.

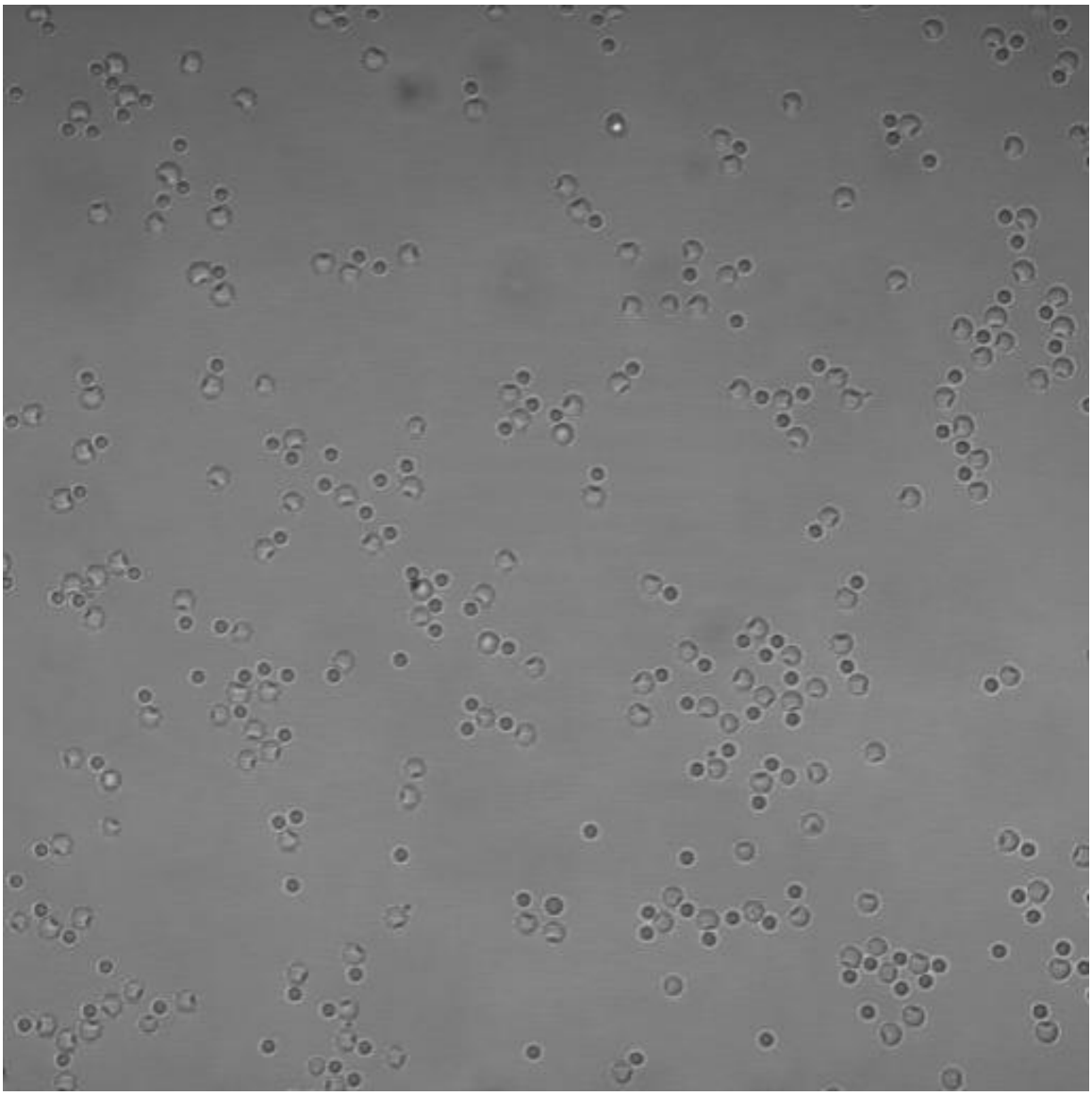

Figure 5.3 Lock colloids (2.4 μm size) and suflate polystyrene spheres (1.4 μm) driven at 20 V peak-to-peak voltage and frequency of oscillation of 1 kHz. Image is $(127.45\ \mu m)^2$.

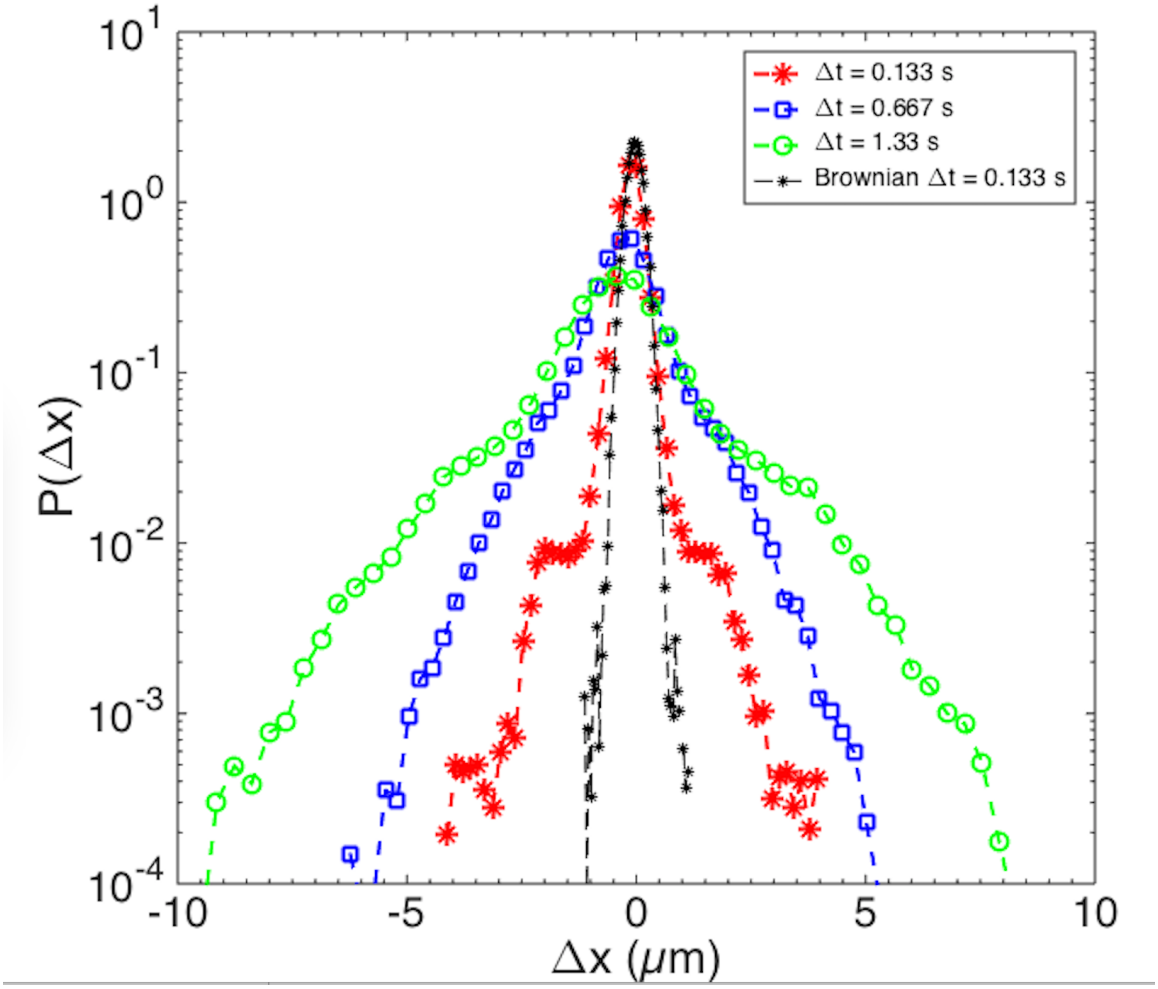

Figure 5.4 Self-part of the van Hove correlation function for lock particles driven at 20 V. For this data, the frequency of oscillation of the field was swept down at a slow rate of ~0.1 kHz/second from 10 kHz to 1 kHz. The self-part of the van Hove correlation function for diffusing locks, for a lag time of 0.133 seconds, is plotted as small black stars. The self-part of the van Hove correlation function for active lock particles is shown in red large starts for a lag time of 0.133 s, blue squares for a lag time of 0.667 s, and green circles for a lag time of 1.33 s.

References

[1] L. Colón-Meléndez, D.J. Beltran-Villegas, G. van Anders, J. Liu, M. Spellings, S. Sacanna, D.J. Pine, S.C. Glotzer, R.G. Larson, and M.J. Solomon, The Journal of Chemical Physics **142**, 174909 (2015).

[2] D.J. Beltran-Villegas, L. Colón-Meléndez, M.J. Solomon, and R.G. Larson, Journal of Colloid and Interface Science **463**, 242 (2016).

[3] Y. Wang, Y. Wang, D.R. Breed, V.N. Manoharan, L. Feng, A.D. Hollingsworth, M. Weck, and D.J. Pine, Nature **491**, 51 (2012).

[4] Y. Wang, Y. Wang, X. Zheng, G.-R. Yi, S. Sacanna, D.J. Pine, and M. Weck, Journal of the American Chemical Society **136**, 6866 (2014).

[5] S. Sacanna, M. Korpics, K. Rodriguez, L. Colón-Meléndez, S.-H. Kim, D.J. Pine, and G.-R. Yi, Nature Communications **4**, 1688 (2013).

[6] A.D. Dinsmore, A.G. Yodh, and D.J. Pine, **383**, 239 (1996).

[7] K.L. Kohlstedt and S.C. Glotzer, Physical Review E **87**, 032305 (2013).

[8] D. Ortiz, K.L. Kohlstedt, T.D. Nguyen, and S.C. Glotzer, Soft Matter **10**, 3541 (2014).

[9] T.K. Haxton and S. Whitelam, Soft Matter **8**, 3558 (2012).

[10] S. Sacanna, W.T.M. Irvine, P.M. Chaikin, and D.J. Pine, Nature **464**, 575 (2010).

[11] M. Kamp, N.A. Elbers, T. Troppenz, A. Imhof, M. Dijkstra, R. van Roij, and A. van Blaaderen, Chemistry of Materials **28**, 1040 (2016).

[12] D.J. Pine, P.M. Chaikin, S. Sacanna, and W. Irvine, U.S. patent 8815118 (26 August 2014).

[13] D.J. Ashton, R.L. Jack, and N.B. Wilding, Physical Review Letters **114**, 237801 (2015).

[14] P.-Y. Wang and T.G. Mason, Journal of the American Chemical Society **137**, 15308 (2015).

[15] F. Ma, X. Yang, H. Zhao, and N. Wu, Physical Review Letters **115**, 208302 (2015).

[16] S. Sacanna, W.T.M. Irvine, P.M. Chaikin, and D.J. Pine, Nature **464**, 575 (2010).

[17] S. Gangwal, O.J. Cayre, and O.D. Velev, Langmuir **24**, 13312 (2008).

[18] B.W. Kwaadgras, M. Verdult, M. Dijkstra, and R. van Roij, The Journal of Chemical Physics **135**, 134105 (2011).

Appendix

Appendix A

As briefly discussed above, the bond length distribution, shown in Fig. 2.3, has two broad peaks which indicate the bond length distance between specifically and nonspecifically bound lock-key pairs. The broadness of these peaks can be explained by the polydispersity of the particles and by out-of-plane Brownian rotation of particle pairs. Out-of-plane rotation of the particles would lead to the identification of false positives: nonspecifically bound pairs of particles that our code would identify as specifically bound (see Figure A.1 below). In such cases, the apparent distance between particle centroids is below the threshold value for specific bonds, and the bond is classified as a specific bond.

The presence of false positives, and the effect that they have on the determination of kinetic rate constants, was studied and discussed in subsequent modeling and simulation work (see Chapter 2, ref. [21]). Due to the presence of false positives, S-F and S-NS kinetic rate constants include the influence of fast events with short lifetimes, leading us to obtain S-F and S-NS kinetic rate constants that describe these events as faster than what they occur in reality. The influence of false positives leads us to estimate NS-S free energy differences that indicate a weaker specific bond than in reality. Modeling work that incorporated the effect of false

positives successfully described the impact such misidentifications have on the measurement of S-NS kinetic rate constants and the NS-S free energy difference.

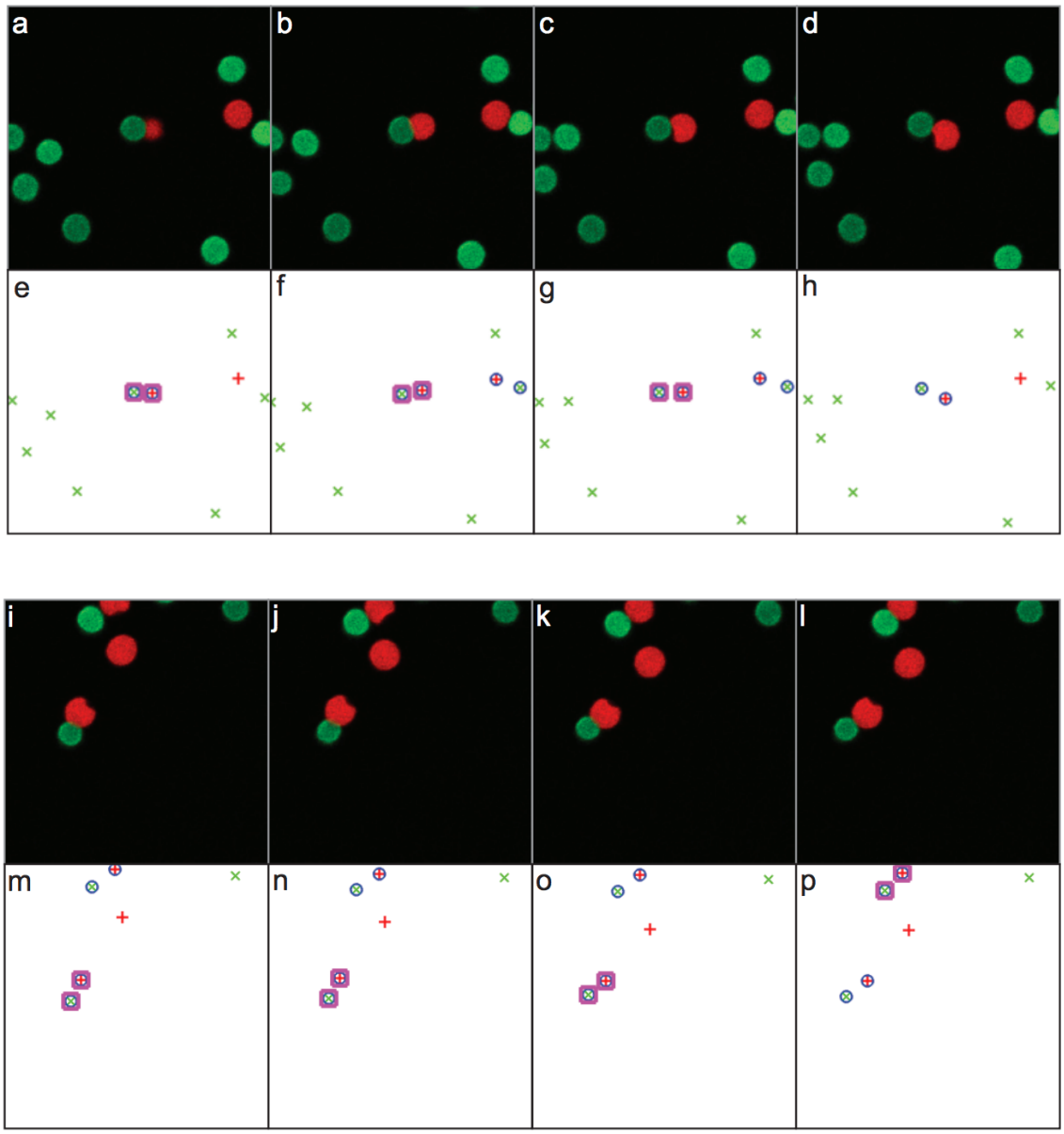

Figure A.1 *Experimental evidence for false positive identification*
Panels (a) thru (d) show confocal images of a correctly identified specifically bound lock-key pair that undergoes a transition to being nonspecifically bound. Panels (e) thru (h) shows the position of the particles on the previous panels, by denoting locks with red crosses and keys with green "x"s. Thick purple circles denote what the code has identified as a specific bond between the particles, using the bond length distribution from Figure 2.3. In panels (i) – (l), we show a false positive "specific bond", as can be seen from comparing these images with centroid position

images on panels (m) thru (p). We can clearly see that the dimple of the lock particle is not occupied by a key.